PROCESS MODELLING FOR DISTORTIONS IN MANUFACTURING OF FIBRE REINFORCED COMPOSITE MATERIALS

by

Kenan ÇINAR

B.S., Mechanical Engineering, Celal Bayar University, 2005

M.S., Mechanical Engineering, Boğaziçi University, 2008

Submitted to the Institute for Graduate Studies in
Science and Engineering in partial fulfillment of
the requirements for the degree of
Doctor of Philosophy

Graduate Program in Mechanical Engineering
Boğaziçi University

2014

PROCESS MODELLING FOR DISTORTIONS IN MANUFACTURING OF FIBRE REINFORCED COMPOSITE MATERIALS

APPROVED BY:

Assoc. Prof. Nuri Ersoy (Thesis Supervisor)	…….
Prof. Günay Anlaş	…….
Assist. Prof. Cahit Can Aydıner	…….
Prof. Fazıl Önder Sönmez	…….
Assoc. Prof. Murat Sözer	…….

DATE OF APPROVAL: 05.06.2014

ACKNOWLEDGEMENTS

I would like to express my special appreciation and thanks to my advisor Assoc. Prof. Nuri B. Ersoy, who has been a tremendous mentor for me. I would like to thank him for encouraging my research and for allowing me to grow as a research scientist. His advice on both research as well as on my career have been priceless.

I would also like to thank my committee members, Prof. Günay Anlaş, Prof. Fazıl Ö. Sönmez, Assoc. Prof. Murat Sözer, and Assist. Prof. C. Can Aydıner for serving as my committee members. I also want to thank them for their brilliant comments and suggestions.

A special thanks to my family. Words cannot express how grateful I am to my family for all of the sacrifices that they have made on my behalf.

I would also like to thank all of my friends especially Niyazi Tanlak, Fatih Öz, and Onur Yüksel who supported me in writing, and incented me to strive towards my goal.

I also acknowledge the support of Boğaziçi University Research Fund for and Istanbul Development Agency (ISTKA) for their support under project codes 12A60D3 and ISTKA/BIL/2012/58 respectively.

ABSTRACT

PROCESS MODELLING FOR DISTORTIONS IN MANUFACTURING OF FIBRE REINFORCED COMPOSITE MATERIALS

A fibre reinforced composite part generally takes a shape different from the one that is originally designed after removing from the mould at the end of the curing process. Due to the anisotropic nature of the fibre reinforced composite materials, the Coefficient Of Thermal Expansion (CTE), the cure shrinkage rate and the stiffness are direction dependent. The direction dependent behaviour of the composite materials, with the aid of temperature change during curing, triggers some mechanisms that are responsible for the residual stresses and shape distortions. Composite parts of various geometries (L-section, U-section and flat strip laminates), various stacking sequences, thicknesses and lay-up conditions are manufactured by using prepreg material system designated as AS4/8552. These parts were scanned using a 3D laser coordinate scanner to obtain the distorted geometry. A 2D and 3D Finite Element model has been developed for predicting shape distortions during curing of fibre reinforced composite parts. The total curing process is divided into three steps that corresponds the states that resin is passing through during curing: viscous, rubbery, and glassy. The material property changes during curing are implemented in the model through a three step user subroutine. Various mechanisms that contribute to shape distortions are identified and their relative contributions are assessed. Some observations on final shape and manufacturing defects are addressed. The shape distortion predictions are compared to the distortions measured by 3D laser coordinate scanner and satisfactory results are obtained.

ÖZET

ELYAF TAKVİYELİ KOMPOZİT MALZEMELERİN İMALATINDAKİ ÇARPILMALAR İÇİN SÜREÇ MODELLENMESİ

Elyaf takviyeli kompozit malzemelerden üretilen parçalar pişme süreci sonrasında kalıptan ayrıldığında genellikle orijinal tasarlanmış şeklinden farklı bir şekil almaktadırlar. Elyaf takviyeli kompozit malzemelerin isotropic olmayan doğasından dolayı laminaların termal genleşme katsayısı, pişme çekmesi oranı ve katılıkları yöne bağlıdır. Kompozit malzemelerin yöne bağlı davranışları pişme sırasında sıcaklığın değişimi ile birlikte artık gerilmelere ve şekil bozukluklarına neden olan bazı mekanizmaları tetiklemektedirler. AS4/8552 prepreg malzeme sistemi kullanılarak çeşitli geometrilere (L-kesitli, U- kesitli ve düz dar laminat), çeşitli istifleme oryantasyonlarına, kalınlıklara ve serim durumlarına sahip kompozit parçalar üretilmiştir. Çarpılma geometrilerini elde etmek için bu parçalar üç boyutlu lazer koordinat tarayıcısı ile taranmıştır. Elyaf takviyeli kompozit malzemelerin pişme sonrasındaki şekil bozukluklarını öngörmek için iki ve üç boyutlu sonlu elemanlar modeli geliştirilmiştir. Tüm pişme prosesi reçinenin pişme sürecinde geçtiği viskoz, kauçuk, ve camsı durumlara karşılık gelen üç adıma bölünmüştür. Üç adımlı kullanıcı altprogramı ile pişme sırasında değişen malzeme özellikleri modele entegre edilmiştir. Artık gerilmelere ve şekil bozukluklarına neden olan çeşitli mekanizmalar tespit edilmiş ve bu mekanizmaların göreli katkıları değerlendirilmiştir. Parçaların nihai şekillerine ve imalat hatalarına ilişkin çeşitli gözlemler aktarılmıştır. Şekil bozukluklarına ilişkin model öngörüleri üç boyutlu lazer taramasıyla ölçülen değerlerle karşılaştırılmış, tatmin edici sonuçlara ulaşılmıştır.

TABLE OF CONTENTS

ACKNOWLEDGEMENTS iii

ABSTRACT iv

ÖZET v

LIST OF FIGURES viii

LIST OF TABLES xv

LIST OF SYMBOLS xvi

LIST OF ACRONYMS / ABBREVIATIONS xvii

1. INTRODUCTION 1

1.1. Problem Statement 3

1.2. Literature Review 4

1.2.1. Development of Process Induced Residual Stresses 5

1.2.2. Resin Property Development 19

1.2.3. Process Modelling of Stresses and Deformations 22

2. EXPERIMENTAL WORK 28

2.1. Materials and Manufacturing 28

2.1.1. Materials Used 29

2.1.2. Specimen Preparation 30

2.1.3. Samples Manufactured 31

2.2. Measurement of Part Geometry 32

2.3. Observations on Manufactured Parts 34

2.3.1. Corner Thickening 34

2.3.2. Fibre Wrinkling 34

2.3.3. Bagging Condition 35

2.3.4. Effect of Stacking Sequence 35

3. 2-D FINITE ELEMENT ANALYSIS 37

3.1. Steps of Analysis 37

3.2. Stress Calculation and Implementation of Mechanical Properties 40

3.3. Tool-part Interaction 43

3.4. Meshing and Boundary Conditions 44

3.5. Implementation of Fibre Wrinkling into FEA 46
4. 3-D FINITE ELEMENT ANALYSIS 50
4.1. Meshing and Boundary Conditions for L Section Parts 50
4.2. Meshing and Boundary Conditions for U Section Parts 53
4.3. Meshing and Boundary Conditions for Flat Parts 55
5. RESULTS AND DISCUSSION 57
5.1. Observations on Parts Manufactured 57
5.1.1. Corner Thickening 57
5.1.2. Fibre Wrinkling 59
5.1.3. Bagging Condition 64
5.1.4. Effect of Stacking Sequence on the Warpage 70
5.2. 2D Comparison between Predicted and Manufactured Samples 75
5.2.1. Thermoelastic Spring-in 75
5.2.2. Effect of Sliding Stress and Viscous State Shear Modulus. 79
5.2.3. Stresses Developed During Curing 82
5.2.4. Tool-part Interaction 83
5.2.5. Parameter Sensitivity Analysis 86
5.2.6. Results of 2D Fibre Wrinkling Model 88
5.3. Comparison of Predicted and Measured 3D Distortion Patterns 92
5.3.1. Comparison of Predicted and Measured 3D Distortion Patterns for L-section Samples 92
5.3.2. Comparison of Predicted and Measured 3D Distortion Patterns for U-section Samples 96
5.3.3. Comparison of Predicted and Measured Warpage for Flat Strip Samples 101
6. CONCLUSIONS AND FUTURE WORK 102
REFERENCES 108

LIST OF FIGURES

Figure 1.1. A schematic representation of vacuum bagging [1]. 1

Figure 1.2. A reduction in enclosed angle. 6

Figure 1.3. The effect of through-thickness contraction on spring-in angle. a) Stiff in shear b) No restriction in shear [28]. 10

Figure 1.4. Effect of tool-part interaction on distortion. a) Flat parts. b) Parts that have corner sections. 11

Figure 1.5. Effect of resin flow on the warpage in flat laminates. 15

Figure 1.6. Corner thickening due to resin flow from arms to the corner. 16

Figure 1.7. Development of the degree of cure and the glass transition temperature through the cure [50]. 20

Figure 1.8. Development of shear modulus through cure [75]. 21

Figure 1.9. Development of mechanical properties of composite through cure [75]. 22

Figure 2.1. The mould used during manufacturing: (a) dimensions in mm. (b) closed to form an autoclave. 28

Figure 2.2. Flat composite plate bagged up on a steel tool inside the autoclave. . 29

Figure 2.3. Schematic representation of specimen fabrication for L-shaped laminates. 31

Figure 2.4. Measurement of part geometry. The deformation scale is in mm. ... 33

Figure 2.5. Thickness variation for UD16-15 laminate. The scale is in mm. 33

Figure 2.6. Wrinkled fibres during lay-up a) less fibre wrinkling b) more fibre wrinkling. 35

Figure 2.7. Schematic representation of strip placement and stacking configuration. 36

Figure 2.8. Warpage values are measured in Section 1 and Section 2. 36

Figure 3.1. a)Various stages of the mrcc, b) steps of fem model. 38

Figure 3.2. The fibre, transverse, and through-the-thickness directions. 40

Figure 3.3. Schematic block diagram of umat for stress calculation. 42

Figure 3.4. Interface friction characteristics. 44

Figure 3.5. The finite element mesh and boundary condition for the l-shaped sections in step-1and 2 (a) and step-3 (b). 45

Figure 3.6. Fem steps of the model. 47

Figure 3.7. a) Compressive strains occurred after initial step, b) reduction of elastic modulus for the elements that have compressive strains. 49

Figure 4.1. 3D modelling of L shape parts. 51

Figure 4.2. Loading and boundary conditions for L shaped parts. 51

Figure 4.3. Finite element mesh for the tool and 4-ply laminate. 52

Figure 4.4. Material orientation used in ABAQUS for 4 -ply cross-ply laminate (XP4) with the designation of $[0/90]_{s.}$ 53

Figure 4.5. Symmetry boundary condition for U shaped parts. 54

Figure 4.6. Loading and boundary conditions for U shaped parts. 55

Figure 4.7. The symmetry planes and symmetry boundary conditions for flat strips parts. 55

Figure 4.8. Loading and boundary conditions for flat strip parts. 56

Figure 5.1. Thickness variation for UD16-R15 laminate and XP16-R15 The scale is in mm. 57

Figure 5.2. Thickness variation for UD16-R25 laminate and XP16-R25. The scale is in mm. 58

Figure 5.3. Thickness measurement at the mid-section of the laminates. 58

Figure 5.4. Observed wrinkled fibres during lay-up. 59

Figure 5.5. Initial fibre wrinkles convert to in-plane fibre waviness after curing. 60

Figure 5.6. Photomicrograph at 5x magnification from the arm of the L-shaped laminate. The left one is 4 plies unidirectional $[0]_4$ laminate and the right one is 12 plies cross-ply $[0/90]_{3s}$ laminate. 60

Figure 5.7. Photomicrograph at 5x magnification from the corner of the L-shaped laminate. The upper one (a) is 4 plies unidirectional $[0]_4$ laminate and the lower one (b) is 12 plies cross-ply $[0/90]_{3s}$ laminate. 61

Figure 5.8. Photomicrograph at 5x magnification from the corner of the L-shaped 4 plies unidirectional $[0]_4$ laminate that manufactured in the second way of lay-up. 62

Figure 5.9. Measured spring-in for $[0]_4$ L-section parts with R15 mm corner radius. 63

Figure 5.10. Measured spring-in for $[0]_4$ L-section parts with R25 mm corner radius. 63

Figure 5.11. Measured warpage in the fabricated strips of UD4 plies. 65

Figure 5.12. Measured warpage in the fabricated strips of XP4 plies. 65

Figure 5.13. Measured warpage in the fabricated strips of XP4 plies. 66

Figure 5.14. Measured deformation patterns in the fabricated UD4-R15. 67

Figure 5.15. Measured deformation patterns in the fabricated UD4-R25. 67

Figure 5.16. Measured deformation patterns in the fabricated XP4-R15. 68

Figure 5.17. Measured deformation patterns in the fabricated XP4-R25. 68

Figure 5.18. Thickness variation for UD4-R25 laminate. 69

Figure 5.19. Thickness variation for XP4-R25 laminate. 69

Figure 5.20. Schematic representation of strip placement and stacking configuration. 70

Figure 5.21. Warpage values for different stacking sequence. 71

Figure 5.22. Warpage values are measured in Section-1 and Section-2. 71

Figure 5.23. Warpage values measured in section 1 and section 2 for UD-R15 $[0]_4$. 72

Figure 5.24. Warpage values measured in section 1 and section 2 for XP-R15 [0/90]s. 73

Figure 5.25. Warpage values measured in section 1 and section 2 for XP-R15 [90/0]s. 73

Figure 5.26. Spring-in values for XP-R15[0/90]s laminate. Scale is in mm. 74

Figure 5.27. Spring-out values for XP-R15 [90/0]s laminate. Scale is in mm. 74

Figure 5.28. Effect of sliding shear stress and viscous shear modulus on spring-in predictions for UD-R25 parts. 76

Figure 5.29. Effect of sliding shear stress and viscous shear modulus on spring-in predictions for XP-R25 parts. 77

Figure 5.30. Effect of sliding shear stress and viscous shear modulus on spring-in predictions for UD-R15 parts. 78

Figure 5.31. Effect of sliding shear stress and viscous shear modulus on spring-in predictions for XP-R15 parts. 79

Figure 5.32. Representation of warpage along 3rd direction for 4 ply R15 parts. .. 81

Figure 5.33. Fibre direction stress for UD4-R15 part at the end of (a) 2nd step (b) 3rd step. 83

Figure 5.34. Fibre direction stress for XP4-R15 part at the end of (a) 2nd step (b) 3rd step. 83

Figure 5.35. Representation of opening at the end of 2nd step for 16UD-R15 part. 84

Figure 5.36. Surface defects created by separation of part from the tool during manufacturing. 84

Figure 5.37. Stresses and displacements at the contact interface at the end of the second step for 16UD-R25 part. 85

Figure 5.38. Main effects of the DOE factors on the results of spring-in. Refer to Table 5.1 for values of the parameters. 87

Figure 5.39. Percent effect on spring-in of the geometric parameters. 87

Figure 5.40. Percent effect on spring-in of the material parameters. 88

Figure 5.41. Strain distribution through the thickness at the curve side of the part at the end of each steps of analysis. 88

Figure 5.42. Stress distribution through the thickness at the curve side of the part at the end of each steps of analysis in which reduction ratio is 1. 89

Figure 5.43. Stress distribution through the thickness at the curve side of the part at the end of each steps of analysis in which reduction ratio is 2. 89

Figure 5.44. Stress distribution through the thickness at the curve side of the part at the end of each steps of analysis for the conventional model. 90

Figure 5.45. Measured and predicted spring-in for $[0]_4$ L-section parts with R15 mm corner radius. 91

Figure 5.46. Measured and predicted spring-in for $[0]_4$ L-section parts with R25 mm corner radius. 91

Figure 5.47. Measured and predicted deformation patterns for $[0]_4$ and $[0/90]_s$ L-section parts with R15 mm corner radius. 93

Figure 5.48. Spring-in predictions for UD-R15 parts. 94

Figure 5.49. Spring-in predictions for XP-R15 parts. 94

Figure 5.50. Spring-in predictions for UD-R25 parts. 95

Figure 5.51. Spring-in predictions for XP-R25 parts. 95

Figure 5.52. Measured and predicted deformation patterns for $[0]_4$ and $[0/90]_s$ U-section parts. 96

Figure 5.53. Spring-in predictions for R15 side of U shaped UD parts. 97

Figure 5.54. Spring-in predictions for R25 side of U shaped UD parts. 97

Figure 5.55. Spring-in predictions for R15 side of U shaped XP parts. 98

Figure 5.56. Spring-in predictions for R25 side of U shaped XP parts. 98

Figure 5.57. Measured and predicted full field deformation patterns for long U-Shaped $[0]_4$ parts. 99

Figure 5.58. Spring-in predictions for long U- Shaped UD4 parts. 99

Figure 5.59. Measured and predicted full field deformation patterns for long U-Shaped $[0/90]_s$ part. 100

Figure 5.60. Spring-in predictions for long U-section Shaped [0/90]s part. 100

Figure 5.61. Spring-in predictions for flat strip parts of 300 mm length. 101

Figure 6.1. Various stages of the MRCC. 105

LIST OF TABLES

Table 2.1. Physical properties of AS4/8552. 30

Table 2.2. Samples manufactured during the study. 31

Table 3.1. Material properties in the rubbery and the glassy state [29]. 39

Table 4.1. Mesh convergence for UD R25 4 plies L shaped part. 52

Table 5.1. Factor values used in parameter study. 86

Table 6.1. List of various mechanisms that are active during manufacturing (MRCC), and their relative importance (H:High, M:Medium, L:Low) as a function of thickness. 105

Table 6.2. List of parameters used in model and their relative importance. 106

LIST OF SYMBOLS

^{o}C	Celsius
E_{11}	Elastic modulus in fibre direction
E_{22}	Elastic modulus in transverse direction
E_{33}	Elastic modulus through thickness
GPa	Gigapascal
G_{ij}	In-plane shear modulus
MPa	Megapascal
mm	Millimeter
Ø	Initial part angle
ΔØ	Total spring-in angle
ΔT	Change in temperature
α_{ii}	Coefficient of thermal expansion in principal direction
$\alpha_{Ø}$	Circumferential coefficient of thermal expansion
α_{R}	Radial coefficient of thermal expansion
ε_{11}	Fibre direction strain
ε_{22}	Transverse direction strain
ε_{33}	Through thickness direction strain
ε_{ii}^{cure}	Cure shrinkage strains in principal directions
$\varepsilon_{Ø}$	In-plane chemical shrinkage strain
ε_{R}	Through thickness chemical shrinkage strain
ß	Angle between the arms
γ_{ij}	In-plane shear stresses
υ_{ij}	Poisson ratios

LIST OF ACRONYMS / ABBREVIATIONS

AS4/3501-6	Low viscous Prepreg Material
AS4/8552	High viscous Prepreg Material
CHILE	Cure hardening instantaneous linear elastic constitutive model
COMPRO	Two dimensional finite element code
CPRESS	Autoclave pressure
CSHEAR	Tool-part interface shear stress
COPEN	Opening between part and tool
CSLIP	Relative slip between part and tool
CTE	Coefficient of Thermal Expansion
DMA	Dynamic Mechanical Analyser
DOE	Design of Experiment
DSC	Differential Scanning Calorimeter
FBG	Fibre Bragg Grating
FE	Finite Element
FEM	Finite Element Model
FEP	Fluorinated Ethylene Propylene
FEBM	Finite Element Based Micromechanics
FVF	Fibre Volume Fraction
GIM	Group Interaction Modelling
MRCC	Manufacturer Recommended Cure Cycle
RVE	Representative Volume Element
RTM	Resin Transfer Moulding
R15	The part with 15 mm radius
R25	The part with 25 mm radius
SCFM	Self Consistent Field Micromechanics
UD	Unidirectional parts
XP	Cross-ply parts

1. INTRODUCTION

Fibre reinforced composite materials have been increasingly used in various structural components in aerospace, marine, automotive and wind energy sectors. Although manufacturing and investment costs of composite materials are high as compared to conventional materials, primarily metals, their higher strength per unit weight, less machining and fastening operations increase the popularity of composite materials day by day. The direction dependent mechanical properties of composite materials can also be advantageous in some applications where strength is only required in a specific direction.

In aerospace applications, fibre reinforced composite materials are manufactured by autoclave processing in order to achieve low void content (<0.1%) required for aerospace components. In the autoclave manufacturing technique, resin pre-impregnated layers of fibres called prepregs are sequentially laid on the mould in predetermined stacking sequence, covered with a peel ply, breather and vacuum bag in order. A schematic representation of vacuum bagging can be seen in Figure 1.1.

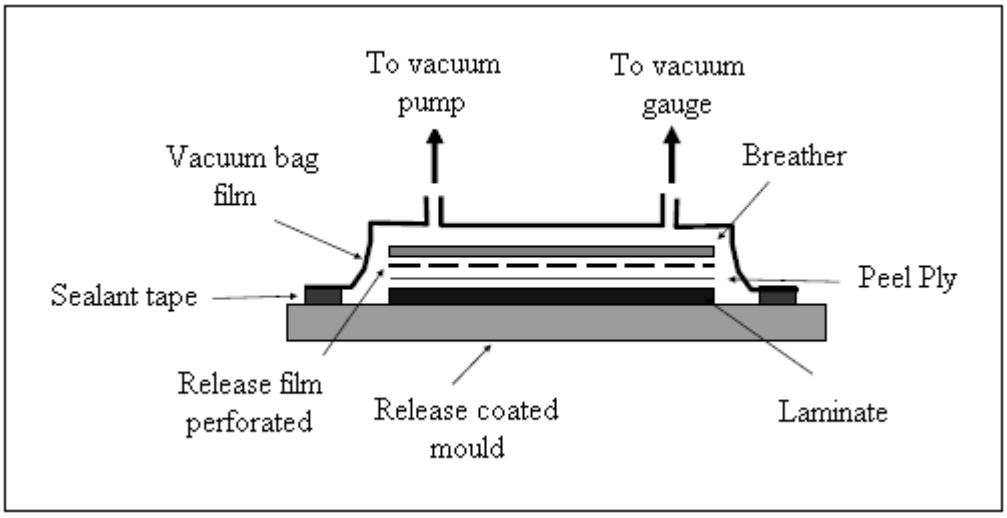


Figure 1.1. A schematic representation of vacuum bagging [1].

During the process pressure and heat are applied according to the process curing cycle. A different Manufacturer Recommended Cure Cycle (MRCC) is used for each prepreg systems because each prepreg system has different resin chemistry. The aim of the cure cycle is to cure the resin with low void content and bond the resin to the fibres.

In the processing of composite materials, generally the final shape of the composite parts is not the same as the mould shape after the process. Also, process induced distortions cannot be entirely eliminated. In the literature these distortions are represented by spring-in in curved parts and by warpage in flat parts. A reduction in enclosed angles of a curved region is called spring-in. Problems occur during and after the assembly of parts due to poor contact between mating surfaces unless the magnitude of these distortions are predicted within the tolerances. The solution of this problem is very complex because the absolute magnitude of the distortion is difficult to predict and is often variable in production even the production conditions held constant. In manufacturing floor, a trial and error approach is preferred to solve these problems but this method is very expensive and time consuming in manufacturing of large components. If the distortions are predicted closely in advance the investment to the trial and error modification can be prevented. In order to predict the process induced distortions, the mechanisms behind them should be examined first.

The basic reason behind the distortion is the process induced residual stresses occurring during the manufacturing process. The unbalanced distribution of residual stresses inside the composite materials results in deformation, matrix cracking, and even delamination. In the literature five main mechanisms or sources have been identified responsible for process induced residual stresses; mismatch in the thermal expansion coefficients, resin cure shrinkage, tool-part interaction, cure gradients and volume fraction gradients. Residual stresses can be categorized according to scale they are originated and whether they are thermoelastic and non-thermoelastic.

Residual stresses can be grouped as micro scale residual stresses and macro scale residual stresses. Micro scale residual stresses develop between fibre and resin as consequence of (i) thermal expansion mismatch between fibres and the resin, (ii) cure shrinkage of resin and (iii) moisture absorption. The residual stresses at this scale do not

cause any distortions on the composite laminate although they adversely affect the strength of the laminate by matrix cracking in the laminate. The stresses at this scale are self-equilibrating so that they do not lead to large deformations. On the other hand, residual stresses at the macro scale are the source of large dimensional changes. Anisotropic behaviour of individual plies, constraint effect of individual plies and tooling constraints are the main sources that trigger the residual stresses at this scale.

Residual stresses can be classified as thermoelastic or non-thermoelastic. Thermoelastic residual stresses are reversible so that the distortion can be eliminated by heating the part to its curing temperature. The source of these stresses in the composite materials is the difference between in plane thermal strains and the through thickness thermal strains. Non-thermoelastic residual stresses, on the other side, are irreversible and the mechanisms behind them are more complex. These mechanisms can be listed as follow; tool-part interaction, cure shrinkage, consolidation, cure gradients, and fibre volume fraction gradients.

1.1. Problem Statement

A fibre reinforced composite part generally takes a different shape from the one that is originally designed after removing from the mould at the end of the curing process. Traditional method used by manufacturers is a trial and error approach to fabricate the composite parts within the dimensional tolerances but this method is very expensive and time consuming. The solution of this problem is to predict the absolute magnitude of the distortion and then to design a mould that gives the desirable final shape according to the prediction.

Unlike conventional materials such as metals, which are isotropic in nature, fibre reinforced composite materials are generally anisotropic. Due to their anisotropic nature, the Coefficient Of Thermal Expansion (CTE), the cure shrinkage rate and the stiffness of the laminate are direction dependent. The direction dependent behaviour of the composite materials assisted by temperature change during curing triggers some mechanisms that are responsible for the residual stresses. Also, tool-part interaction, resin flow, initial defects

such as fibre wrinkling is some of the other contributors to residual stress. These residual stresses occurring during curing of composite materials cause distortions at the end of the production. In the literature these distortions are represented by spring-in in curved parts and warpage in flat parts. There are no commercial software that take into account all mechanisms cited above to predict the distortions of complex shape parts. The reason behind this is the fact that there is a large number of material parameters, characterization of which are difficult and the mechanisms behind the residual stresses are not formulated precisely for modelling especially at the early stages of the cure. In addition, the material properties at the early stages of the resin cannot be measured properly due to difficulties in implementing useful experimental setups.

Most of the process modelling of distortions in the literature is two- dimensional and can be applied to simple shape parts but these models are insufficient for modelling of complex three- dimensional parts. Furthermore, a precise definition of the tool-part interface is not available in commercial software to predict the shape distortions in composite parts.

The basic objective of this thesis is implement a heuristic finite element method that simulates all aspects of composite manufacturing in order to understand the relative importance of the mechanisms behind shape distortions. The method is verified against a large number of parts manufactured by autoclave moulding.

1.2. Literature Review

Processes induced residual stress and deformations are inevitable in processing of composite materials as mentioned before so that there are many studies in the literature about this subject. These studies can be grouped into two basic categories: studies on clarifying the mechanisms behind process induced residual stresses and deformations and studies on predicting these deformations through different numerical and analytical methods.

1.2.1. Development of Process Induced Residual Stresses

The knowledge of the development of the process induced residual stresses allows one to control and adjust the processing parameters in order to manufacture high quality parts and predict the distortion in the working tolerances. There are number of mechanisms that are responsible for the development of residual stresses and distortions. Thermal anisotropy, cure shrinkage of the resin, tool-part interaction, resin flow, consolidation, fibre volume fraction gradients, moisture swelling, prepreg variability, gradients in temperature and degree of cure can be listed as the mechanisms identified to be responsible for process induced residual stresses.

1.2.1.1. Thermal Anisotropy. The Coefficient Of Thermal Expansion (CTE) difference between fibre and the resin causes residual stresses in both micro and the macro scale but not cause any distortion in the micro scale [2]. CTE of fibres is smaller than the resin. This CTE difference is responsible for the thermal anisotropy in the macro scale because the part expands or contracts more in the resin dominated directions as compared to fibre dominated directions. A balanced symmetric flat part does not give any out of plane distortion if there are no tooling constraints. However in curved region, the CTE difference between the thickness direction and the circumferential direction results in a reduction in the enclosed angle of the part, which is called spring-in. In the case of isotropic materials, the contraction upon cooling in a curved region is uniform, therefore the angle is preserved. For composite materials, the thermal expansion coefficient, hence the strain in the through-the-thickness direction is much higher than the in-plane expansion coefficients and strains, and this leads to a reduction in enclosed angle, as shown in Figure 1.2. The effect is reversible, with the spring-in reducing if the part is reheated.

The first attempt to calculate the magnitude of enclosed angle has been proposed by Nelson and Cairns [3] in the following equation;

$$\Delta\emptyset = \emptyset \,.\frac{(\boldsymbol{\alpha}_{\emptyset} - \boldsymbol{\alpha}_{\boldsymbol{R}})\,\Delta\boldsymbol{T}}{\mathbf{1} + \boldsymbol{\alpha}_{\boldsymbol{R}}\,\Delta\boldsymbol{T}} \qquad (1.1)$$

where, $\Delta\emptyset$ is the spring-in angle, $\emptyset$ is the initial angle of the part, $\alpha_{\emptyset}$ is the circumferential coefficient of thermal expansion, α_R is the radial coefficient of thermal expansion, ΔT is the temperature change.

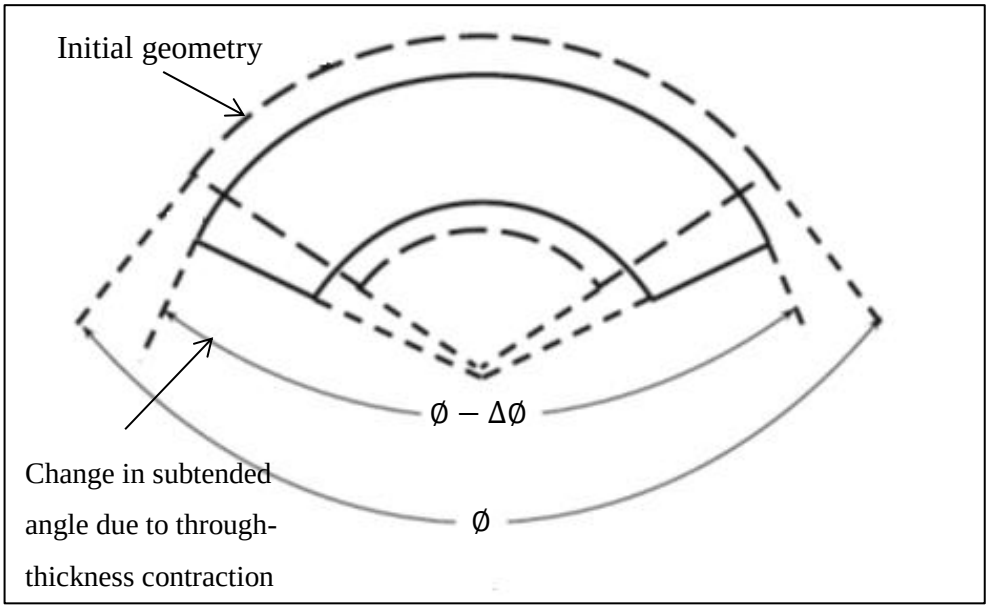


Figure 1.2. A reduction in enclosed angle.

The development of residual stresses and distortions in unsymmetrical flat [4, 5] and symmetric curved laminates [6, 7] was monitored by interrupting the cure cycle at pre-determined points. By this method, thermoelastic and non-thermoelastic components of spring-in and the effect of change in transverse CTE during curing on distortion can be determined. Gigliotti *et al*. measured the stress free temperature of composite samples. It was found that the stress free temperature of samples cured beyond vitrification is higher than their cure temperature, which provides evidence that a certain percentage of non-thermoelastic stress is present in the part. It was concluded that out of plane deformation of the flat laminates are small when the laminates are cured at a low temperature [4] and the deformation increase very sharply during the second heating ramp of MRCC [5]. Gigliotti *et al*. also found that the transverse CTE remains almost constant during the curing cycle below the glass transition temperature. Ersoy *et al.* [7] adopted a cure quench technique to analyse the development of spring-in angle during cure of AS4/8552 thermosetting composite using a similar approach to that presented by Gigliotti *et al*. In their experiments, C-shaped laminates were cured on the inner wall of an aluminium tube. It

was found that the specimens quenched before vitrification had more spring-in angle than the samples quenched after vitrification. According to their explanation, in the rubbery state (above the glass transition temperature) the thermal expansion coefficient of the part was larger than the coefficient of thermal expansion in the glassy state; therefore to quench the samples in the rubbery state caused the samples to shrink more, in turn, spring-in more . They also observed that the thermoelastic component of spring-in was %50 of the final spring-in, the remaining is the non-thermoelastic component mainly due to cure shrinkage. A similar mechanism that incorporates a higher CTE of the part in the rubbery state was proposed by Svanberg and Holmberg [6] to explain the spring-out phenomena in post-curing of partially cured curved regions produced by Resin Transfer Moulding (RTM). This production method is different from the prepreg layup method. In this method, the resin is injected into the mould that consists of two rigid mould halves (the female and male moulds) and then the mould is heated. They observed that increase in the cure temperature led more spring-in because a high cure temperature contributed to larger thermal strains and higher degree of cure. This means that the stress level and corresponding frozen strains at vitrification is higher at higher in-mould cure temperature.

Another method to quantify the thermoelastic and non-thermoelastic components of spring-in and study the thermoelastic behaviour of composite angle brackets with varying laminate thickness, stacking sequence and part radius was proposed by Radford and Rennick [8] and then similar technique was used by Garstka [9]. A laser reflection method was used to measure spring-in angle as the samples were exposed to the temperature change in an oven. It was found that the thermoelastic effect is independent of laminate thickness and corner radius but is affected by the laminate stacking sequence. Gartska has got slightly different results related to effect of thickness on thermoelastic component of spring-in. Experimental results showed a small increase in the thermoelastic spring-in for thicker laminates that is believed to be a result of corner thickening due to resin percolation during processing.

Curing residual stresses occurring during the cool-down stage of the cure cycle due to the thermal anisotropy of the laminate have been modelled by ignoring stresses generated during cure [10-13, 14]. Determining curing stresses in the symmetrical boron-epoxy composite laminates, Hahn and Pagano used linear elastic constitutive model and

calculated the stresses through Classical Laminated Plate Theory [10]. They assumed that the part is stress free up to the highest curing temperature prior to the final cool-down stage due to low stiffness of the resin so that the residual stresses occurring during the cool-down stage were only taken into account. In order to examine the effect of viscoelastic relaxation of the resin on the residual stress development during the cool-down stage, a linear viscoelastic constitutive model was used [11-13]. Weitsman concluded that the residual stresses were reduced by more than 20 % [11] due to viscoelastic relaxation.

1.2.1.2. Cure Shrinkage. In thermosetting polymers during polymerization, the liquid resin is converted into a hard brittle solid by chemical cross-linking which leads to the increase in density and a corresponding reduction in volume [15]. Resin shrinkage only occurs during the curing process and ceases once cure is complete. The amount of shrinkage of composite during curing is different between the in-plane directions and the through thickness direction due to the constraints provided by the fibres. Shrinkage strains will be much larger in the transverse direction than the fibre direction. Hence, the effect of cure shrinkage on residual stress and deformation is very similar to the effect of thermal contraction on residual stress and deformation and can be analysed in the same way. In order to take into account the effect of cure shrinkage on the spring-in, Radford and Diefendorf [16] added a cure shrinkage term into the eq. (1.1).

$$\Delta\emptyset = \emptyset[\left(\frac{(\boldsymbol{\alpha_\emptyset} - \boldsymbol{\alpha_R})\Delta\boldsymbol{T}}{\mathbf{1} + \boldsymbol{\alpha_R}\Delta\boldsymbol{T}}\right) + \left(\frac{\boldsymbol{\varepsilon_\emptyset} - \boldsymbol{\varepsilon_R}}{\mathbf{1} + \boldsymbol{\varepsilon_R}}\right)] \qquad (2.2)$$

where, $\Delta\emptyset$ is the spring-in angle, $\emptyset$ is the initial angle of the part, $\alpha_\emptyset$ is the circumferential coefficient of thermal expansion, α_R is the radial coefficient of thermal expansion, $\varepsilon_\emptyset$ is the in-plane chemical shrinkage strain, ε_R is the through-the-thickness chemical strain, ΔT is the temperature change

The volume change of the polymeric resin during cure was measured by using various methods. Cure shrinkage strains were calculated from measurement of the change in the dimensions of a test specimen during cure. White and Hahn [17] used a simple method to measure the cure shrinkage. Prepreg plies were placed in a computer controlled oven and cured according to MRCC. During the cure cycle, at each of the predetermined

points, a prepreg sample was taken out of the oven and the thickness was measured after cooling to room temperature. The cure strains were then calculated from the changes in dimensions of samples at room temperature. Another common method is to directly measure the chemical shrinkage using a volumetric dilatometer [18-21] or a Thermo-Mechanical Analyser (TMA) [22]. Russell *et al*. used PVT apparatus to measure the neat chemical shrinkage of 3501-6 resin. The volume change in the resin was determined by the deflection of the bellows that is filled by mercury and covers a piezometer cell. A Linear Variable Differential Transducer (LVDT) measured the deflection of the bellows at the thickness direction. Johnston [22] used Thermo-Mechanical Analyser to measure the shrinkage strains by monitoring the displacement of a small probe pressing lightly on the specimen surface. All specimens were processed isothermally (130^{o}C, 150^{o}C, and 170^{o}C) for eliminating thermal strain effects. A non-contact technique was used by Garstka [9] for measuring cure shrinkage strains of unidirectional and cross-ply laminates. A non-interlaced camera was mounted on a tripod and focused on contrasting targets marked on the sides of the two steel plates that were in contact with the composite specimen during the test. It was found that cross-ply laminates have more through-the-thickness chemical shrinkage than unidirectional ones due to the constraints imposed by fibres in both in-plane directions in cross-ply specimens. Ersoy and Tugutlu used Dynamic Mechanical Analyser (DMA) in the compression mode to find the through-the-thickness cure shrinkage strain values of partially cured unidirectional and cross-ply composite samples [23]. The experimental results showed that cure shrinkage strains in cross-ply samples are measured to be twice of the strains in unidirectional ones, which is similar to the findings of Gartska *et al*. [9].

The concept of equivalent CTE was used to account for resin shrinkage during the curing process [24-27]. Volumetric cure shrinkage of the resin was implemented through the change of CTE of the composite material in numerical models.

The existing analytical approaches that used Equation 1.2 for predicting spring-in of a curved shape parts do not distinguish between cure shrinkage in different phases of cure, and the material properties such as shear modulus of resin changes during curing. Wisnom *et al*. examine the effect of material properties at the rubbery state on the final spring-in value by adding another term to the Equation 1.2 [28]. It was found that spring-in values

are small as compared to the values found through analytical Equation 1.2. Due to low shear modulus of resin, there is some shear deformation (shear-lag) between plies to maintain the same arc length during curing, which in turn decreases the amount of in-plane stress and causes smaller spring-in values, as shown schematically in Figure 1.3. This shear-lag phenomenon was also shown in the two-step FEM model that predicts the spring-in angles in C-sections [29]. The predicted and the measured spring-in values for different thicknesses show a considerable decrease in spring-in with part thickness, which matches well the trend predicted from the analytical study of Wisnom *et.al*. [28]. It can be concluded from these studies that the effect of cure shrinkage on spring-in decreases with increasing the thickness due to this shear-lag phenomenon.

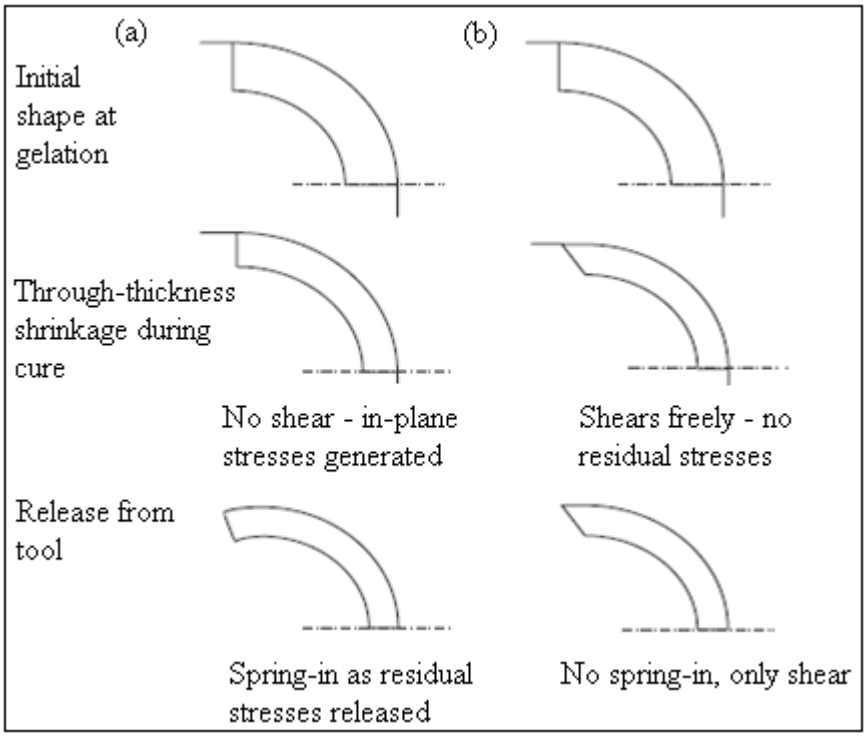


Figure 1.3. The effect of through-thickness contraction on spring-in angle. a) Stiff in shear b) No restriction in shear [28].

1.2.1.3. Tool-Part Interaction. When the tool and part are forced together due to autoclave pressure and subjected to a temperature ramp, a shear interaction occurs between the tool and the part due to differential Coefficients of Thermal Expansion (CTE) between the tool and the part. As this occurs prior to any significant degree of resin modulus development, the laminate shear modulus is very low and plies that are distant from the tooling are not

loaded to the same extent as those close to the interface. This non-uniform stress distribution is locked in as the resin cures, and upon removal from the tooling, the resultant bending moment warps the part away from the tooling as shown in Figure 1.4.

The tool-part interaction which comes from the tooling constraints is an extrinsic source of residual stresses and deformations as opposed to the thermal anisotropy and cure shrinkage, which are considered to be due to intrinsic properties of the composite material itself.

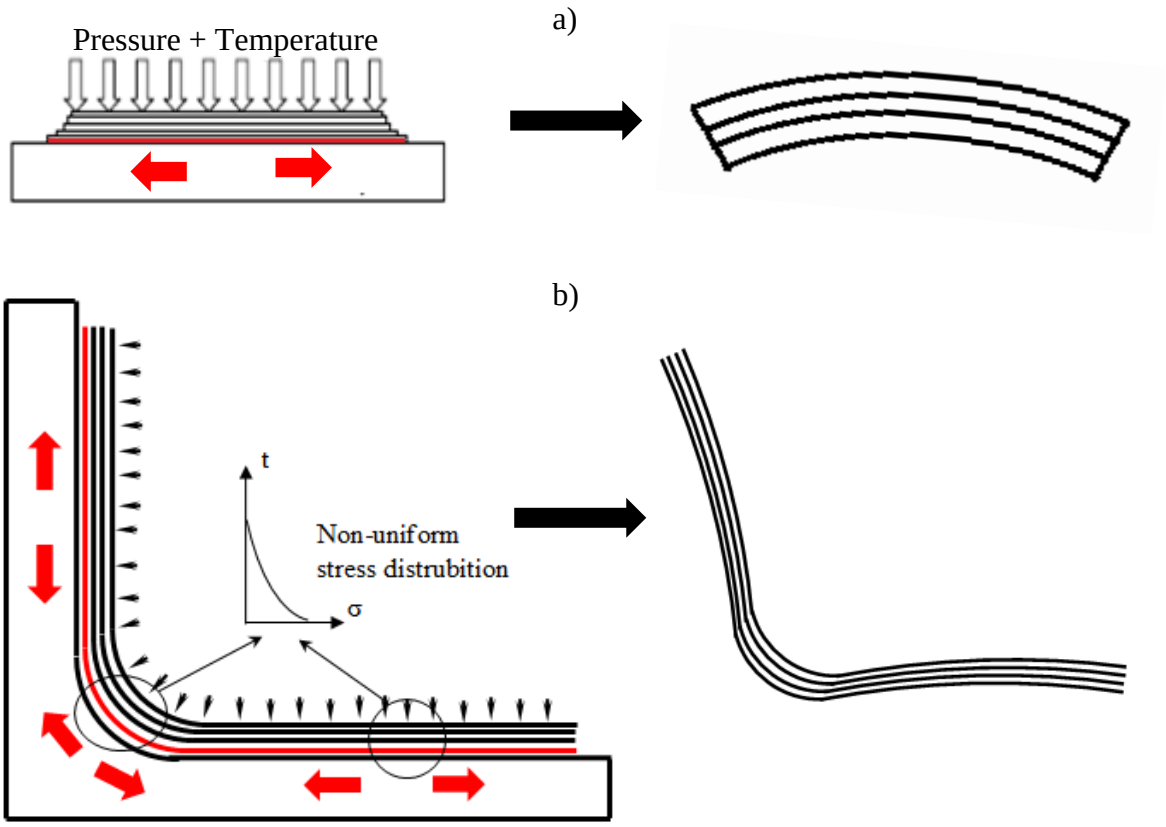


Figure 1.4. Effect of tool-part interaction on distortion. a) Flat parts. b) Parts that have corner sections.

The effect of the tool-part interaction on the distortion has been emphasized in recent studies [22, 30-43]. Twigg *et al.*[30-32] conducted experimental and numerical studies to understand the mechanics and constitutive behaviour of the tool-part interface. To examine the interaction between the tool and part, an instrumented tool method was introduced [30]. A strain gage mounted on a thin aluminium sheet was laid on the flat carbon/epoxy

laminate for measuring strains on the thin aluminium sheet imposed by tool-part interaction with time during the cure cycle. It was concluded that a sliding friction condition occurs during the heat-up portion of the cure cycle and the value of sliding shear stress increases with degree of cure. During temperature modulations and cooling, sticking interface condition dominates the interaction. Also it was shown that the use of FEP release film prevents the sticking of the laminate to the tool, on the other hand using release agent causes adhesive bonding at the interface. In an experimental study of the same group, the effect of part aspect ratio and processing conditions on warpage were investigated [31]. For a given lay-up and material, part aspect ratio was found to be more effective than pressure on warpage, while the magnitude of warpage was not influenced significantly by the tool surface condition.

As opposed to Twigg *et al*. which employs strain gage to the tool, Gartska *et al*. mounted a strain gage directly on the prepreg by using the spot curing technique [9, 45], where a small spot of uncured prepreg is cured to provide a bonding location for strain gage. After mounting the strain gage on the prepreg before moulding, the strain gage was calibrated using a tensile test machine for determining the modulus of the prepreg. The prepreg was than cured using the MRCC, and strain is recorded vs. time. In another method to measure strains due to expansion of the mould during curing, Fibre Bragg Grating (FBG) sensors (optical fibre sensors) were embedded along the reinforcement orientations [41, 46, 47]. Four different mould materials (aluminium, steel, carbon foam, and carbon-epoxy composite based) were used to examine the strain difference between the moulds [41]. A clear difference was observed between the samples cured on the aluminium and steel moulds, and those on the other moulds. Higher strains were measured on the aluminium and steel moulds. It should be kept in mind that FBG sensors can only measure the strains after gelation, since mechanical interlocking between the sensor and the resin is only possible after gelation, whereas the instrumented tool and instrumented ply techniques can measure the tool-part interaction stresses in the early stages of cure where the resin is in its viscous state.

Experimental setups were designed to quantify the friction coefficient and shear stress at the tool-part interface [37-38, 48-50], which consist of two temperature controlled heated platens and a loading plate where the prepreg is wrapped around. The prepreg is

then pulled against other prepreg layers or the tool material in a tensile testing machine. After the heated platens are pushed towards each other by using a pneumatic ram [37, 38] or spring screw set [50] to simulate autoclave pressure, the tensile test machine applies a load and records load vs. displacement data. Ersoy *et al*. [50] measured the interfacial shear stresses between the tool and the part directly in terms of temperature and pressure. They observed that significant tool-part interaction stresses, presumably due to fibre friction develop during early stages of cure even when the resin is in its viscous state. Friction coefficients during the curing were measured in other studies [37, 48, 49]. Martin *et al*. and Flanagan *et al*. have measured only static friction coefficient during the ramp-up portion of the cure cycle and the observations [49, 50] showed that the tool-part interface changes during the process cycle. Kaushik and Raghavan have measured both static and dynamic friction coefficients as a function of degree of cure, ramp rate and pressure for the entire cure cycle [37, 38]. They found that the static and dynamic friction coefficients drop at early stages of cure as degree of cure advances to α=0.2, increases cure as degree of cure advances to α=0.4, and then decreases again as degree of cure advances to α=0.6 and the dynamic coefficient of friction remains constant whereas the static coefficient increases considerably. This indicates that as the cure advances, the interface condition changes from sliding to sticking condition. This is also confirmed by the observation that as the cure advances there is less resin residue at the interface which is an indication of a shift from cohesive to adhesive failure.

In the context of roughness and anisotropic expansion behaviour of tooling material, Kappel *et al*. [34, 35] found that differences in coarseness affect the warpage deformations although anisotropic expansion behaviour of the raw tooling material due to rolling process does not cause any significant distortions. They also examined the transfer of shear stress from the tool to the parts and inside the laminate by using different surface conditions and prepreg systems. One of the results of the study is that the prepreg systems M21/T800 (E32), M21/T800 (E38) and AS4/8552 (E35) show considerable deformations when using release film, on the other hand when the same release film is used for 977-2/IM7 (E40) prepreg system, deflection is considerably smaller.

Several numerical modelling approaches to capture the tool-part interaction effect were developed [9, 22, 42-44, 48]. In these models, tool-part interaction is modelled as a

cure hardening elastic shear layer which remains intact until the tool is removed [22, 42, 44], as an interfacial sliding friction at the interface [9, 36, 48] and as the part stuck to the tool surface with no relative motion [43]. These models are semi-empirical models that need to be calibrated with the use of experimental data. By adjusting the shear layer properties such as elastic and shear modulus, the amount of stress transferred between the tool and part can be tailored and a range of tool-part interface conditions can be simulated. According to the parametric study [32] using this shear layer model, the tool-part interfacial shear stress distribution is critical for accurate modelling of distortions. Arafath *et al*. [39, 40] also used this shear layer assumption in the closed-form solution for process-induced stresses and deformations for flat and curved geometries. A parametric study examining the effects of the shear layer properties such as elastic and shear modulus and shear layer thickness on the compaction behaviour was performed and it was concluded that improving the ability to slip of the flexible male mould upon the laminate can be helpful to apply pressure to the L-shaped laminate at the corner side [51]. In the study of Flanagan [48] and Hubert [52], the interfacial shear stress was assumed to obey the Coulomb friction model, where the interfacial shear stress is proportional to the contact pressure and the constant of proportionality is the fiction coefficient until a critical shear stress is reached after which sliding with constant shear stress is observed. Hubert [52] used this stick-slip behaviour at the interface between the mould and the composite part in their 3D Finite Element Analysis that model the Resin Transfer Moulding (RTM) process of composite parts.

1.2.1.4. Resin Flow and Compaction. Among the large number of phenomena occurring during composite manufacturing, resin flow is an another important issue. It affects the fibre volume fraction distribution, the mechanical properties of the laminate and the final dimensions of the part [53]. Stress calculations require knowledge of the local elastic properties that are functions of the local fibre volume fraction. Resin rich and resin poor regions are a consequence of resin flow within the part. Resin flow and resin pressure distributions in the laminate play a critical role in void formation and migration. For sandwich panels, surface dimpling and core buckling also depend on the pressure distribution and therefore resin movement in the laminate [53].

For the purpose of increasing Fibre Volume Fraction (FVF) of the laminates bleeder is applied under the vacuum bag during manufacturing of composite laminates. Resin is at the liquid state at the beginning of the processing cycle, so that it moves and bleed through the thickness direction into the bleeder placed on the prepreg stack. Consequently local FVF gradients occur inside the laminate. For example for the flat parts, resin rich regions are formed at the tool side of the laminate while resin poor regions are formed at the bag side of the laminate, represented schematically in Figure 1.5. The thermal expansion coefficient of the laminate can vary through the thickness if there is a FVF gradient through the thickness because CTEs depends on FVF. The low CTE at the upper side of the laminate results in less shrinkage as compared to lower side of the laminate during the cool down. This unsymmetrical behaviour causes warpage for the flat parts. Although the distortion mechanism for the curved parts resembles the one that occur in flat parts, there is another factor, called fibre bridging, that is responsible for the non-uniform FVF through the thickness. The autoclave pressure is ineffective at the corner of the part due to fibre bridging, which causes a low pressure region at the corner which is then percolated by resin so that the thickness of the part at the corner increases and a resin rich layer is formed at the surface, as represented in Figure 1.6. This effect is more pronounced in tighter radius parts. Corner thickening results in higher resin fraction at the corner, higher through-the-thickness CTE. The higher CTE at the corner causes more spring-in since there will be more shrinkage through-the-thickness at cool down step.

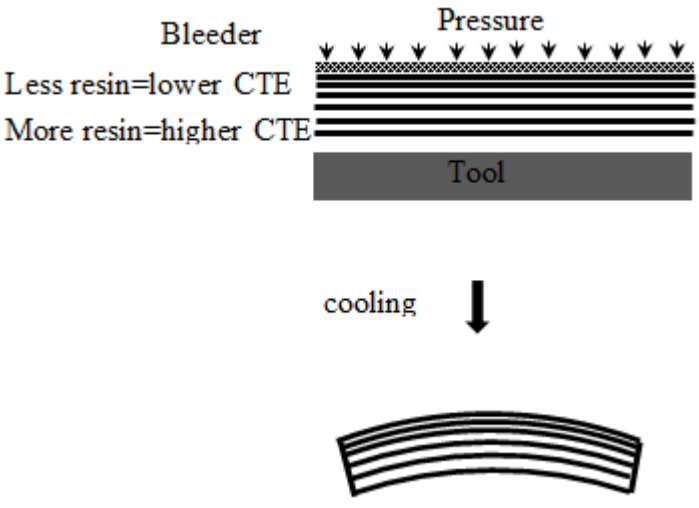


Figure 1.5. Effect of resin flow on the warpage in flat laminates.

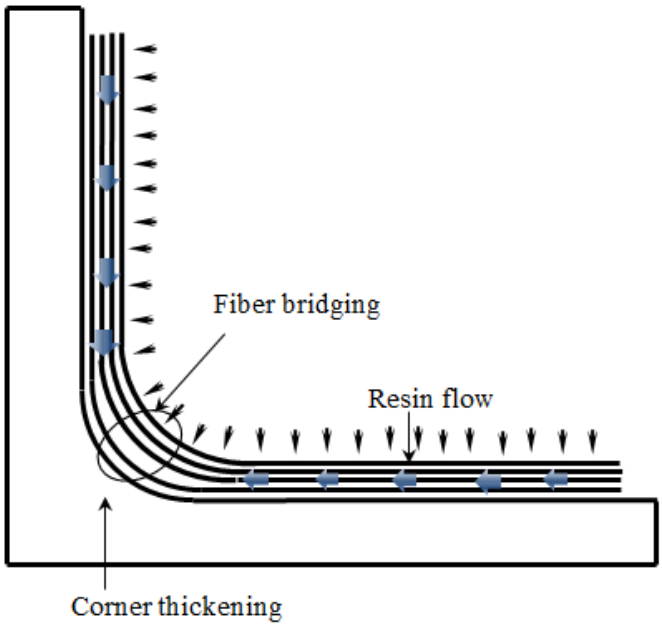


Figure 1.6. Corner thickening due to resin flow from arms to the corner.

A number of models have been developed to predict composite resin flow in autoclave processing [22, 54-59]. These studies were primarily focused on consolidation of simple shaped laminates. Gutowski *et al*. proposed a squeezed-sponge three-dimensional flow and one-dimensional compaction model and considered the composites as a deformable unidirectional fibre reinforcement system where the load is balanced by the average resin pressure and the average effective stress in the fibre network. Darcy's Law in a porous medium was used for flow in the vertical direction of the composite material. Dave *et al*. used the same approach but their model considered the flows in different directions to be coupled. Hubert *et al*. and Li and Tucker developed a two-dimensional flow-compaction model for L shaped composite laminates. They solved the equations by using finite element method. Hubert *et al*. used an incremental, quasi linear elasticity model for the solid bed stress. On the other hand Li and Tucker developed a special hyper-elastic model for fibre bed stress and their model updates the mesh geometry and fibre orientation as consolidation proceeds. Li and Tucker also observed the fibre buckling effect in their numerical analysis.

Darrow [60] observed that symmetric carbon fibre/epoxy laminates are warped while classical laminated plate theory predicts no warpage. The non-uniform fibre volume

fraction through the thickness, locally resin-rich near the tooling, uniform through most of the thickness, and resin-poor at the top surface adjacent to the bleeder results in a convex up curvature. Volume fractions of 0.52 and 0.59 have been observed at the bag side and the tool side respectively whereas for interior region the fibre volume fraction was 0.57. Darrow then included a number of volume fraction variations in a classical laminated plate analysis and predicted the mid-plane curvatures based on composite thermal expansion and matrix shrinkage. The results of this analysis for long uniaxial carbon fibre/epoxy sample strips of varying thickness match the curvature that is experimentally observed. Further, the results show that volume fraction gradient induced during top bleed autoclave cure is an important component of composite part warpage [60]. Darrow and Smith [24] examined the effect of the fibre volume fraction gradient on L-shaped laminate experimentally by applying a vacuum bag to the part with and without bleeder. Their model and experiment were compared for a unidirectional part with a 3 mm bend radius. It was observed numerically and experimentally that the effect of fibre volume gradient on the spring-in was small for thicker parts as compared to thinner ones.

Hubert and Poursartip [61] performed experimental investigation on the compaction of the angled composite laminates by using two types of material, low viscosity AS4/3501-6 and high viscosity AS4-8552. The laminates of low viscosity resin gave more resin loss compared to the high viscosity resin. The total compaction strain for low viscosity resin was caused by percolation flow under bleed condition but for high viscosity resin, the total compaction strain was caused by the collapse of voids. The laminate containing low viscosity resin was analyzed to determine the fibre volume fraction gradients for processes with or without bleeder. The data obtained from the experiments indicated that fibre volume fraction was low at the tool side and high at the bag side in the bleed condition. The fibre volume fraction measurements through the thickness and in the longitudinal direction showed that a net percolation flow from the tool to bleeder occurs. There was a small amount of internal percolation flow from the corner to the flat section of the part manufactured in convex tool in the no-bleed condition. They also observed that the parts manufactured on the convex tool have corner thinning whereas the parts manufactured on the concave tool have corner thickening. In the case of the convex tool, the reaction stress in the corner is higher and thus there is thinning and conversely for the concave tool, the reaction stress is lower and there is corner thickening.

1.2.1.5. Fibre Wrinkling. The increased use of fibre-reinforced composite materials in different areas encourages producers to manufacture more complex-shaped parts. It is difficult to manufacture parts with complex shapes due to undesired defects occurring during manufacturing. For example, wrinkles, buckling of plies during lay-up of prepreg-based multilayer composites, etc. are observed in the corner section of the L-shaped parts [61, 62-63]. These wrinkles have negative effect on the strength of the composite parts [64] and affect the amount of the deformation after curing. The elimination of wrinkles is difficult, especially in concave tools.

Most of the published studies have focused on the wrinkles and in plane fibre misalignment of woven cloths [65-67], on the other hand, little effort was given for the prepreg type composite parts [62, 68]. Potter *et al*. [68] have studied the fibre straightness by direct measurement of fibre misalignments in as-delivered prepregs, and by considering the tensile load response of the uncured prepregs. The lead-in region from their load-displacement graph showed that there is some fibre waviness within the uncured prepreg. Lightfoot *et al*. [62] tried to explain the mechanisms that are responsible for the fibre wrinkling and fibre misalignment of unidirectional plies during lay-up of prepregs on the mould. They found that large wrinkles observed in parts with 90^o plies surrounded by 45^o plies if FEP release film is used on the mould. Removing release film prevented the development of fibre wrinkles. No wrinkling was observed within the $[0]_{24}$ although some in-plane waviness was detected.

Fibre waviness has an adverse effect on the stiffness and strength of fibre reinforced composite materials [64, 69-74]. In order to quantify the influence of fibre waviness on stiffness and strength reduction of unidirectional composite materials some analytical studies have been introduced. [69-71]. Hasiao and Daniel [70, 71] developed an analytical model for investigating the effects of fibre waviness on stiffness and compressive strength of unidirectional composites under compressive loading by introducing three types of wavy patterns: uniform, graded and localized waviness. The geometry of waviness was assumed to be planar sinusoidal with an amplitude and a wavelength. The degree of waviness was defined by the amplitude to wavelength ratio. It was shown that stiffness

and compressive strength decreases seriously as the fibre waviness increases. For example, a uniform waviness of 0.043 (amplitude/ wavelength ratio) resulted in appreciable reduction in longitudinal elastic modulus, approximately 42 %. The used materials were IM6G/3501-6 carbon/epoxy and S-glass/epoxy material system in the analytical solution and the experiments. The compression tests were conducted by using Illinois Institute of Technology Research Institute (IITRI) test fixture. Predictions and experimental results were correlated with each other. In addition to analytical models there were also finite element micromechanical models to investigate the effect of fibre waviness on stiffness and strength reduction of composites [72-73]. Karami and Garnich [73-74] developed a micromechanics model including wavy-fibre materials within the resin material. A rectangular unit cell was defined to serve as a Representative Volume Element (RVE). The unit cell was consisted of circular fibres distributed within the matrix. The initial waviness was assumed to be sinusoidal. This sinusoidal shape of fibres was modelled by two methods: by assigning a wavy material orientation to the straight fibres and by drawing fibres like sinusoidal shape. In the model [73-74] AS4/3501-6 carbon/epoxy material system was used. The elastic modulus along the fibre direction decreased with an increase in amplitude to wavelength ratio (A/λ). A uniform waviness of 0.040 and 0.0667 (amplitude/ wavelength ratio) resulted in reduction in longitudinal elastic modulus, approximately 30 % and 53 % respectively.

1.2.2. Resin Property Development

The state of thermosetting resin is not constant during curing. There is considerable transformation from a low molecular weight monomer to a highly cross-linked polymer. The development of cure is usually defined by the degree of cure, α. The degree of cure can be measured using thermal analysis technique called Differential Scanning Calorimeter (DSC), that measures the heat flow rate. The degree of cure is found from the ratio of heat generated at a certain time during the process relative to the total heat generated through the complete cure [23]. The glass transition temperature T_g is an another important thermal property, where the resin transforms from a soft rubbery state to a hard glassy state. The development of degree of cure and glass transition temperature of AS4/8552 material system is shown in Figure 1.7 [50].

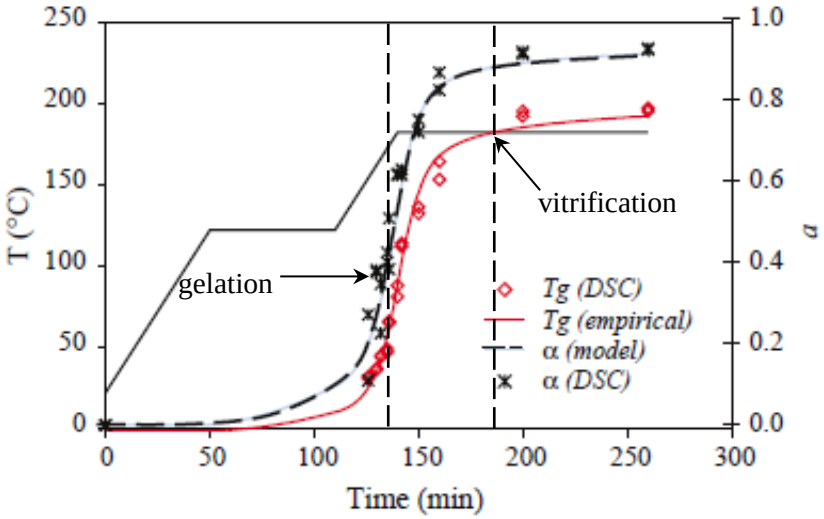


Figure 1.7. Development of the degree of cure and the glass transition temperature through the cure [50].

A sharp rise in the degree of cure during the second ramp of the cure cycle can be seen in Figure 1.7. The sharp rise is indicative of the resin transformation from a viscous fluid to a rubbery solid. Vitrification occurs approximately 45 min after the second hold period starts, at which point the instantaneous glass transition temperature reaches the process temperature. The degree of cure was around 0.7 at vitrification point. At the vitrification point resin transforms from rubbery to glassy state [50].

An experimental method was developed to study the frictional behaviour of AS4/8552 prepreg material system through cure [50]. A testing apparatus was designed to measure frictional resistance between the prepregs and between the prepreg and the tool material. The apparatus consisted of a pair of heated plates and a pressurizing system to simulate the MRCC conditions. Using apparatus to be mounted on tensile test machine the overlapping prepreg material were pulled against to each other. The tensile force, temperature and displacement were recorded during the cure cycle. Inter-ply shear stress was found by dividing the tensile force to the effective area. It was observed that there is sharp rise in shear stress around 160 ^{o}C, which corresponds to degree of cure of 0.3. The resin was believed to be gelled at this degree of cure, developing a measurable modulus to sustain mechanical loads.

The development mechanical properties such as elastic modulus, shear modulus and Poison's ratios were found experimentally, numerically and analytically during curing [75]. The development of shear modulus G_{23} was measured using Dynamic Mechanical Analyser (DMA). The shear modulus measured by DMA tests were compared to the predicted modulus using Group Interaction Modelling, as shown in Figure 1.8. The black continuous line and markers represents the predicted and measured values of G_{23} through the cure cycle respectively. The sharp increase in shear modulus during gelation and vitrification can be seen from Figure 1.8. The elastic modulus E_{22} and shear modulus G_{12}, and G_{23} were found using Self Consistent Field Micromechanics Model (SCFM) and Finite Element Based Micromechanics Model (FEBM) for AS4/8552 prepreg material system [75]. The shear modulus of resin in the rubbery state was determined using Group Interaction Modelling (GIM) and Poisson ratio was assumed to be 0.5 in the rubbery state. Young' modulus and Poisson's ratios of resin and the fibre were taken from Manufacturer's data sheet for the glassy state. Using constituent's properties, transverse elastic modulus and shear modulus of AS4/8552 prepreg material system were calculated by SCFM and FEBM. The evolution of the transverse elastic modulus and shear moduli of AS4/8552 prepreg material system using as well as the neat resin are shown in Figure 1.9.

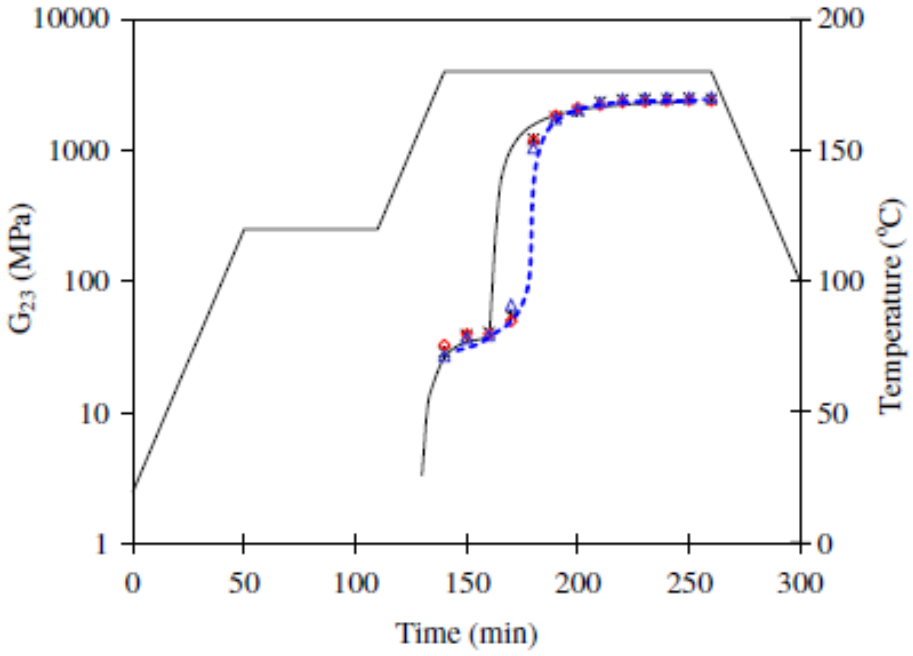


Figure 1.8. Development of shear modulus through cure [75].

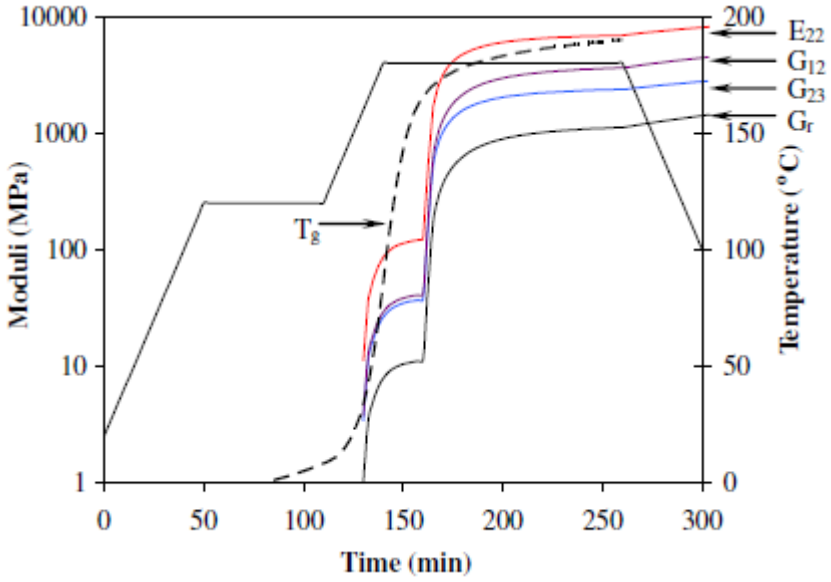


Figure 1.9. Development of mechanical properties of composite through cure [75].

1.2.3. Process Modelling of Stresses and Deformations

In the extensive body of literature published, researchers have spent a considerable effort to predict the distortion in fibre reinforced composite materials by using analytical and numerical methods. An early example of analysing residual stress generation by using Laminated Plate Theory only considered the cool down stage of the processing and it was only one dimensional [10]. However, different mechanisms such as material anisotropy, cure shrinkage, tool-part interaction, and resin flow have an effect on residual stresses and thus distortions. Some of these mechanisms occur from the beginning to the end of the manufacturing process or occur only at the some stages of the process. Due to this complexity, more sophisticated process models have been developed [17, 22, 27, 76].

The relationship given in Equation 1.1 was developed for determining the thermoelastic response of a composite material [16]. It included the effects of initial specimen geometry, the coefficients of thermal expansion and the change in temperature. In order to treat the non-thermoelastic response of cure shrinkage the relationship was extended in Equation 1.2 [8]. Non-thermoelastic distortion was a consequence of cure shrinkage, material property gradients, and stress gradients due to tool-part interaction. The thermoelastic and non-thermoelastic components were differentiated by reheating

technique. The thermoelastic response was determined by measuring the spring-out angle at various temperatures and it was concluded that the thermoelastic behaviour was linear and reversible. One of the main result of the study is that non-thermoelastic component was more effective than the thermoelastic one. Huang and Yang [77] performed some experiments to analyse the effect of mould angle on spring-in. The samples were varying with the enclosed angle of 45^{o}, 75^{o}, 90^{o}, 135^{o}, and 165^{o}. They observed that the spring-in angle significantly increased as the part angle decreased. The experimental data had greater (nearly 14%) spring-in than the predicted one. They used the extended relationship (Equation 1.2) in their numerical analysis and concluded that part angle, cure shrinkage and material anisotropy are responsible for the spring-in. Salomi *et al.* [78] applied this extended formulation to a thermoplastic matrix composite in order to determine the thermoelastic and non-thermoelastic contributions on distortion. The differences observed between experimental and analytical results came from the existence of fibre distortion at the corner. Yoon and Kim [79] analysed the effect of thermal anisotropy and the chemical shrinkage of epoxy on the process induced deformation of carbon fibre/epoxy composite laminates. They measured the spring-in angle of L sectioned laminates of various angle plies and compared the measurements with the numerical predictions. To express the angle change of curved parts due to thermal anisotropy and cure shrinkage, they used a two dimensional thermo-elastic model including changes of properties with respect to temperature. Their predicted spring-in values were well confirmed by experimental data although the predicted ones were slightly smaller than the experimental ones. They concluded that the main sources of spring-in in curved region were the difference between the through-the thickness and in-plane thermal expansion coefficients of plies and chemical cure shrinkage.

White and Hahn [17, 80] developed a process model which predicts a residual stress history during the curing of composite materials by including the effects of chemical and thermal strains. The mechanical properties of composite materials depend on the degree of the cure state of the composite materials. They used Bogetti and Gillespie's [27, 81] cure kinetics model in their study in order to find the degree of cure at the any moment during the cure cycle. The relation between the degree of cure and mechanical properties is modelled by a power law equation. In their elastic residual stress model, laminated plate theory was used and for viscoelastic residual stress model, the quasi elastic method was

used. They combined the cure kinetics and viscoelastic stress analysis to calculate residual moment and in turn find the curvatures simultaneously. In their model, unsymmetrical cross-ply flat laminates were used only. The model did not include the tool-part interaction.

Johnston *et al*. [44] developed a plane strain finite element model which employs a Cure Hardening, Instantaneous Linear Elastic Constitutive (CHILE) model to predict process-induced stress and distortion of composite laminates. They analysed the effect of thermal expansion, cure shrinkage, temperature gradients, degree of cure, resin flow and mechanical constraints on the deformation of the laminates. The tool-part interaction was modelled by elastic "shear layer", which performed until the tool is removed. Their predicted and measured spring-in values were correlated for $[0]_{24}$ lay-up; however the correlation was bad for $[90]_{24}$.

Manufacturing process of fibre reinforced composite materials can be modelled by taken into account the three states of resin. These states are viscous, rubbery and glassy states. In the viscous state, viscosity of resin is low and it can flow due to pressure gradients in the laminate. Flowing of resin through the fibres was modelled by using a two dimensional flow model for composite materials [56, 82]. The porous structure of composite laminate enables one to use Darcian flow theory. The Darcian flow theory was coupled with stress formulation in these studies. Generally, composite structures have one dimension that is much larger than other two dimensions so that they assumed a plane strain condition in the model [56, 82]. The resin was assumed to be an incompressible Newtonian fluid (for simplicity).

In their study Svanberg and Holmberg [6, 83, 84] developed a simplified mechanical constitutive model to predict the shape distortions. They assumed that the mechanical behaviour of the material is constant within rubbery and glassy states and there is a step change in the properties at the glass transition temperature. The rubbery properties they used were simply assumed to be about two orders of magnitude smaller than those in the glassy state. They used three different tool-part interaction models in their FE analysis; freestanding, fully constrained, and frictionless contact conditions. The predictions indicated that the contact boundary conditions give the closest agreement to the measured

spring–in. Then they used their finite element model to predict the spring-in in brackets produced by Resin Transfer Moulding. There were no experimental data about the rubbery properties and the tool-part interaction was oversimplified, which were the main drawbacks of their numerical analysis. Comparison between experimental and predicted shape deformations indicate that after the second cure step the predicted spring-in shows good agreement with the experimental values but after the third cure step the prediction is poor. Their predictions overestimate the spring-in angle after the third cure step.

Ersoy *et al*. [29] developed a two-step 2-D finite element model including anisotropy in the thermal expansion coefficient and cure shrinkage to predict the process induced stress and deformation. The two-step model was representing the rubbery and glassy states of the resin. The reason for preferring two-step approach was the complexity of the determining continuous development of material properties during cure schedule. In each step constant material properties were used. Gelation occurs at approximately 30 % degree of cure, and vitrification occurs at approximately 70 % degree of cure for the resin. Gelation and vitrification are considered to be two main transitions during the curing process. Ersoy used these transitions between the steps of his model. In the first step of the model, before vitrification, rubbery material properties were used, whereas in the second step, after vitrification, glassy material properties were used. The development of resin properties at the rubbery state were predicted by using Group Interaction Modelling (GIM) and then the mechanical properties of the composite were predicted through the two different micromechanics methods, namely Self Consistent Field Micromechanics (SCFM) and Finite Element Based Micromechanics (FEBM). The properties of the composite at the glassy state were determined by both experimentally and numerically. The predictions for the glassy properties were very close to experimental values [75]. In this study, a part geometry and tool material is chosen to minimise the issues related to tool–part interaction and consolidation and hence, the stresses developed before gelation is ignored. Spring-in values predicted by the two-step FEA are very close to the measurements for both unidirectional and cross-ply C-shaped composite parts. The predictions follow the trend of decreasing spring-in with increasing thickness, which matches well with experimental results. The measured spring-in angles are very close to predicted ones for the thicker parts, and slightly lower for the thinner parts, with a maximum difference of 15 %. Wisnom *et al*. explained the phenomenon of decreasing spring-in with increasing thickness

by some shear deformation (shear-lag) between plies to maintain the same arc length during curing, which in turn decreases the amount of in-plane stress and causes smaller spring-in values [28].

Arafat *et al.* [85, 86] developed a closed-form solution based on theory of elasticity for process-induced stresses and deformations in flat and curved composite structures. Their 2D analytic model resembles the classical bi-metallic beam under thermal load, and the axial stress distribution through the thickness depends on material properties that changes during the cure. These stress gradients is controlled by the ratio of fibre direction modulus to transverse shear modulus. The material constitutive model used was the Cure Hardening Instantaneously Linear Elastic (CHILE) model. They mainly concluded that the material properties at early stages of the process drive the final response of the part.

To the present most of work has been focused on two-dimensional models, 3-dimensional process models for composite materials are rather rare due to the complexity of the problem, number of material parameters involved, and the size of the model. As a result most models available in the literature is two-dimensional strain models, which predicts arm bowing and spring-in in one section of the part and these deformations are assumed to be constant though the third direction. Furthermore, the true nature of the tool-part interaction is rather not properly handled, and the tool-part interaction at the viscous state is ignored. However, observations on manufactured composite parts show that the deformation of L-and U-shaped parts is not constrained to a 2-D section, and plain strain (or generalized plane strain) model does not represent the true nature of the part. Furthermore, the tool-part interaction stresses develop at early stages of cure due to fibre friction, even before the resin gels and can sustain mechanical load. Another factor that is recently been studied in the open literature is fibre wrinkling in corner sections, however these studies only deal with wrinkle formation, and do not take into account the effect of fibre wrinkling on shape distortions.

First objective of this study is to investigate the effect of tool-part interaction, fibre wrinkling, stacking sequence and bagging condition on distortions. The second objective of this study is to develop two and three dimensional FE model to predict the process induced deformations for an autoclave processing of composite laminates by taking into

account the interactions in early stages of cure. The predictions of shape distortions of L- and U-shaped parts obtained by the process models are then compared to the distortions measured by 3d laser scanning. Another objective is to assess the relative importance of the various mechanisms that play a role in shape distortions. The process model is then optimized to include a minimum number of material and process parameters.

2. EXPERIMENTAL WORK

The experimental study presented in this chapter includes the manufacturing of various composite specimens with different shapes, the data collection process to measure the geometry of the specimens and various observations of manufacturing defects and shape distortions.

2.1. Materials and Manufacturing

The L and U-shaped laminates were manufactured in a U-shaped steel tool made of IMPAX P20 Hot Work tool steel with a Coefficient of Thermal Expansion of 12.6 μm/m-°C. The shape and dimensions of the tool are shown in Figure 2.1.a. The tool had two corners of radii 25 and 15 mm. The tool can be converted to a mini autoclave by mounting sealed top and side plates (Figure 2.1.b). Heat was applied through the flanges and the web of the tool with plate heaters. Pressure was applied through the compression port and vacuum can be applied through the vacuum port as represented in Figure 2.1.b. The temperature was controlled with a three-channel PID controller. The uniformity of the temperature around the surface of the U shaped tool was checked with 8 thermocouples.

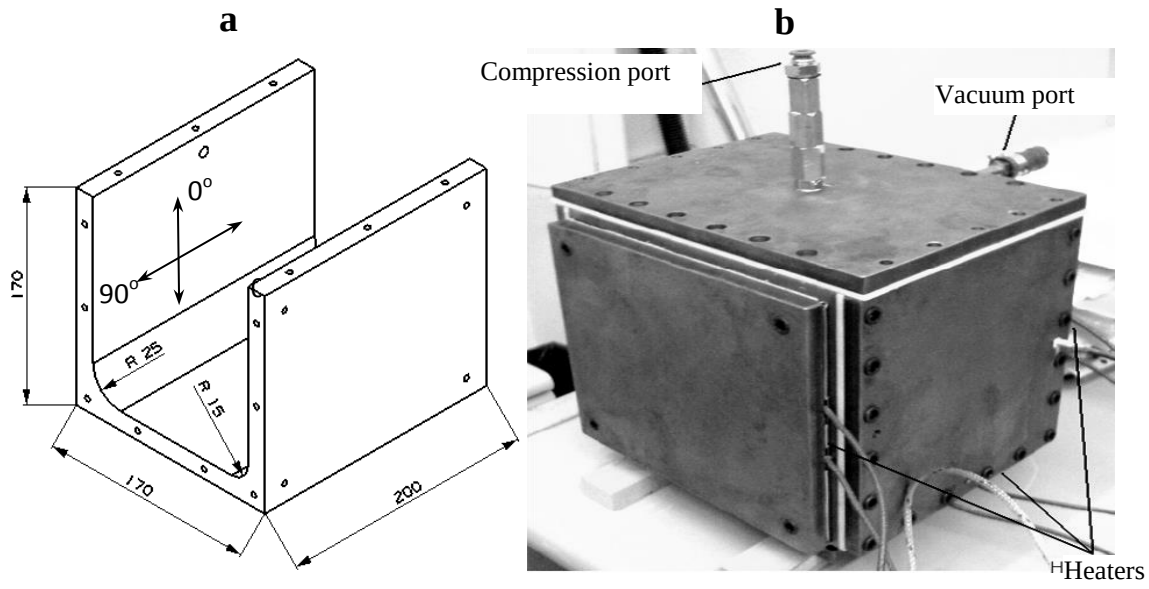


Figure 2.1. The mould used during manufacturing: (a) dimensions in mm. (b) closed to form an autoclave.

Long U-shaped specimens and flat specimens were manufactured by using an autoclave. The autoclave has a inner diameter of 1200 mm and a working length of 1500 mm. Figure 2.2 shows a flat composite laminate prepared within a vacuum bag on the flat tool plate prior to curing.

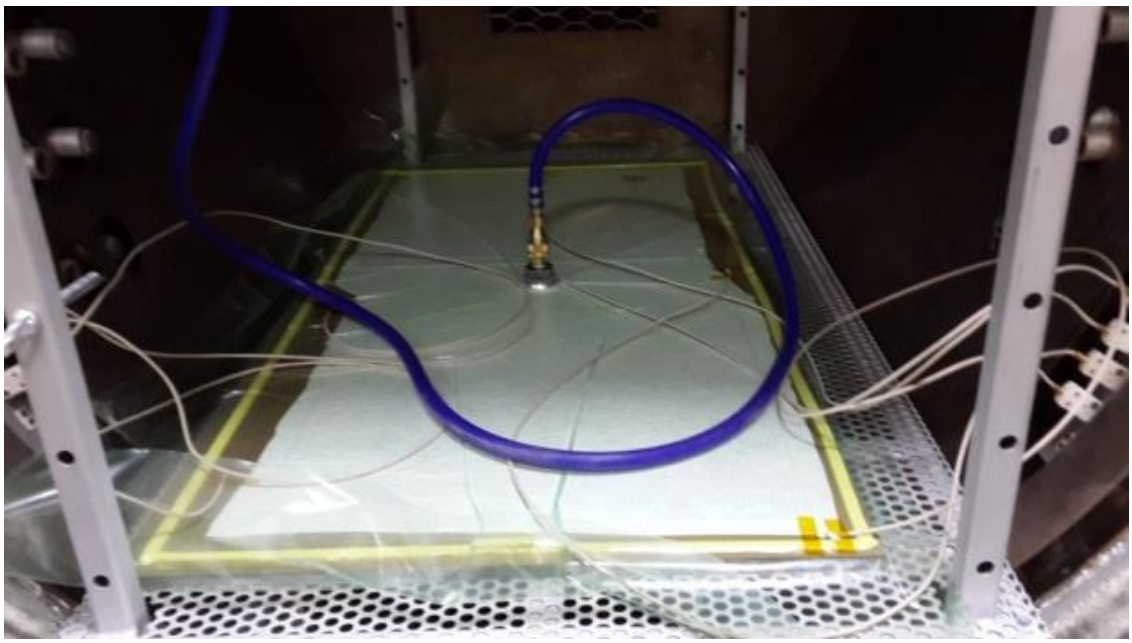


Figure 2.2. Flat composite plate bagged up on a steel tool inside the autoclave.

2.1.1. Materials Used

The material used was a unidirectional carbon-epoxy prepreg material produced by Hexcel Composites with a designation of AS4/8552. The nominal thickness of the single prepreg was specified to be 0.184 mm and the nominal fibre volume fraction as 57.4%. The physical properties of the prepreg used are given in Table 2.1 [87].

The manufacturer's Recommended Cure Cycle (MRCC) includes five steps. In the first step, the part is heated up to 120^{o}C at 2^{o}C/min. In the second step, it is held at 120^{o}C for 60 minutes. In the following step, it is heated up from 120^{o}C to 180^{o}C at 2^{o}C/min.

Then, the part is held at 180^{o}C for 120 minutes. Finally, the part is left to cool down to room temperature before removal from the mould. 0.7 MPa pressure is applied from the beginning to the end of the process and vacuum is applied up to the middle of the second step.

Table 2.1. Physical properties of AS4/8552.

	Value	**Units**
Fibre Density	1.79	g/cm^3
Resin Density	1.30	g/cm^3
Nominal Cured Ply Thickness	0.184	mm
Nominal Fibre Volume	57.42	%
Nominal Laminate Density	1.58	g/cm^3

2.1.2. Specimen Preparation

The vacuum bagging process is the same for home-made mini autoclave and the laboratory scale autoclave. The schematic representation of the vacuum bagging is shown in Figure 2.3. Teflon coated glass fabric release film with a thickness of 0.08 mm was applied over the entire surface of the tool, which allows easy removal of cured parts and good slip of the prepreg on the tool. Each ply was carefully laid-up on only one side of the mould to form an L-shaped stack. The length of the mould is taken as 90^{o}, and the direction running from one arm to the other across the corner is identified as 0^{o} as shown in Figure 2.1.a. Vacuum of approximately -0.9 bar was applied after laying every six plies to debulk the samples, to remove entrapped air and to minimize the possible effect of corner bridging. The stack was then covered with either a peel ply and a breather fabric or a Teflon coated glass fabric before applying a vacuum bag with the help of a sealant tape. For home-made autoclave the top and side plates of the mould were mounted. Finally, the MRCC process was started. After processing, the mould was left to cool down to ambient temperature before the composite part was debagged and removed from the mould.

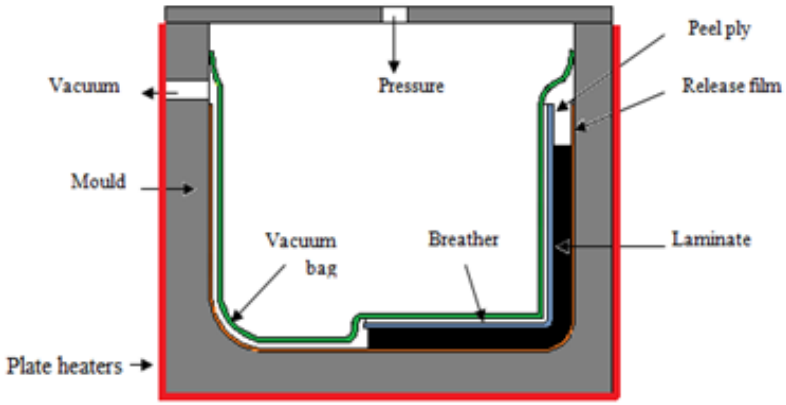


Figure 2.3. Schematic representation of specimen fabrication for L-shaped laminates.

2.1.3. Samples Manufactured

The effect of following parameters on distortion components such as spring-in and warpage is investigated.

- tool geometry
- stacking sequence
- thickness
- bagging condition; bleed and no-bleed
- lay-up condition and fibre wrinkling

The composite samples manufactured are listed in Table 2.2. A total of 75 unidirectional (UD) and cross ply (XP) specimens of various thicknesses (4, 8, 12, and 16 plies), geometries, bagging, and lay-up condition were manufactured. The combination of different parameters was chosen to obtain a wide range of processing conditions in order to examine the mechanisms that are responsible for the distortions.

Table 2.2. Samples manufactured during the study.

Designation	Geometry	Dimension Radius/Width		Bagging Condition	Lay-up Condition	Stacking Sequence	Quantity
UD4-R15	L shaped	15	150	non-bleeding	conventional	$[0]_4$	3
UD4-R15	L shaped	15	150	bleeding	conventional	$[0]_4$	3
UD4-R15	L shaped	15	150	non-bleeding	alternative	$[0]_4$	5
XP4-R15	L shaped	15	150	non-bleeding	conventional	$[0/90]_s$	3
XP4-R15	L shaped	15	150	bleeding	conventional	$[0/90]_s$	3
UD8-R15	L shaped	15	150	bleeding	conventional	$[0]_8$	1

Table 2.2. Samples manufactured during the study (cont.).

XP8-R15	L shaped	15	150	bleeding	conventional	$[0/90]_{2s}$	1
UD12-R15	L shaped	15	150	bleeding	conventional	$[0]_{12}$	1
XP12-R15	L shaped	15	150	bleeding	conventional	$[0/90]_{3s}$	1
UD16-R15	L shaped	15	150	bleeding	conventional	$[0]_{16}$	1
XP16-R15	L shaped	15	150	bleeding	conventional	$[0/90]_{4s}$	1
UD4-R25	L shaped	25	150	non-bleeding	conventional	$[0]_4$	3
UD4-R25	L shaped	25	150	bleeding	conventional	$[0]_4$	3
UD4-R25	L shaped	25	150	non-bleeding	alternative	$[0]_4$	5
XP4-R25	L shaped	25	150	non-bleeding	conventional	$[0/90]_s$	3
XP4-R25	L shaped	25	150	bleeding	conventional	$[0/90]_s$	3
UD8-R25	L shaped	25	150	bleeding	conventional	$[0]_8$	1
XP8-R25	L shaped	25	150	bleeding	conventional	$[0/90]_{2s}$	1
UD12-R25	L shaped	25	150	bleeding	conventional	$[0]_{12}$	1
XP12-R25	L shaped	25	150	bleeding	conventional	$[0/90]_{3s}$	1
UD16-R25	L shaped	25	150	bleeding	conventional	$[0]_{16}$	1
XP16-R25	L shaped	25	150	bleeding	conventional	$[0/90]_{4s}$	1
XP4-R15	L shaped	15	150	bleeding	conventional	$[90/0]_s$	1
UD4	U shaped	15-25	150	bleeding	conventional	$[0]_4$	1
XP4	U shaped	15-25	150	bleeding	conventional	$[0/90]_s$	1
UD8	U shaped	15-25	150	bleeding	conventional	$[0]_8$	1
XP8	U shaped	15-25	150	bleeding	conventional	$[0/90]_{2s}$	1
UD12	U shaped	15-25	150	bleeding	conventional	$[0]_{12}$	1
XP12	U shaped	15-25	150	bleeding	conventional	$[0/90]_{3s}$	1
UD16	U shaped	15-25	150	bleeding	conventional	$[0]_{16}$	1
XP16	U shaped	15-25	150	bleeding	conventional	$[0/90]_{4s}$	1
UD4-Long	U shaped	15-25	500	bleeding	conventional	$[0]_4$	1
XP4-Long	U shaped	15-25	500	bleeding	conventional	$[0/90]_s$	1
S-UD4	Strip	-	300	non-bleeding	conventional	$[90]_4$	3
S-UD4	Strip	-	300	bleeding	conventional	$[90]_4$	3
S-XP4	Strip	-	300	non-bleeding	conventional	$[0/90]_s$	3
S-XP4	Strip	-	300	bleeding	conventional	$[0/90]_s$	3
S-XP4	Strip	-	300	non-bleeding	conventional	$[90/0]_s$	3
S-XP4	Strip	-	300	bleeding	conventional	$[90/0]_s$	3

Specimen designation is as follows: for example UD16-R15 indicates a unidirectional L shaped specimen of 16 plies produced at the 15 mm radius side and XP16 is a cross ply U-shaped specimen.

2.2. Measurement of Part Geometry

The parts manufactured were scanned by a METRIS MCA II 7- axis laser scanner in order to capture the full deformation pattern of the parts. The scanned geometry of the part in the form of a point cloud was virtually placed on the nominal tool through three edge points and the gap distances between the tool and the part are mapped at discrete points over the surface, as shown in Figure 2.4a. In order to calculate spring in values, gap

distances were read on both flanges, at five equally spaced points along 5 stations, as represented in Figure 2.4b. The spring-in angle was measured by drawing secant lines on the arms.

For thickness measurement, both sides (tool and bag side) of the laminates were scanned, and the difference is mapped as thickness on the part. Thickness variation can be seen for UDR15-16 part in Figure 2.5. In order to reveal the effect of corner thickening, thickness measurement was performed at seven stations along the length of the parts.

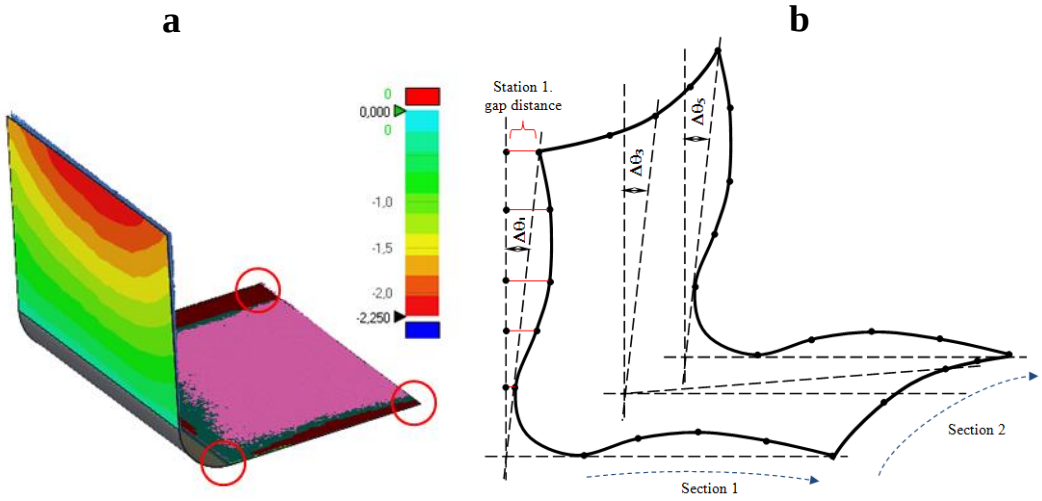


Figure 2.4. Measurement of part geometry. The deformation scale is in mm.

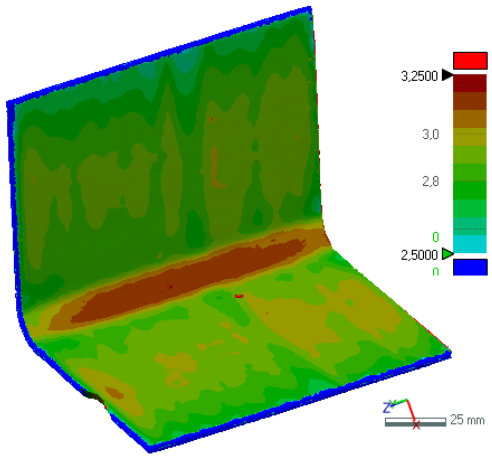


Figure 2.5. Thickness variation for UD16-15 laminate. The scale is in mm.

2.3. Observations on Manufactured Parts

It was observed that various phenomena such as corner thickening, fibre wrinkling, and resin bleeding that occur during production of composite materials affect significantly the amount of deformation. In the following subsections, the experimental procedures adopted to investigate the effect of these phenomena as well as the effect of the stacking sequence are explained.

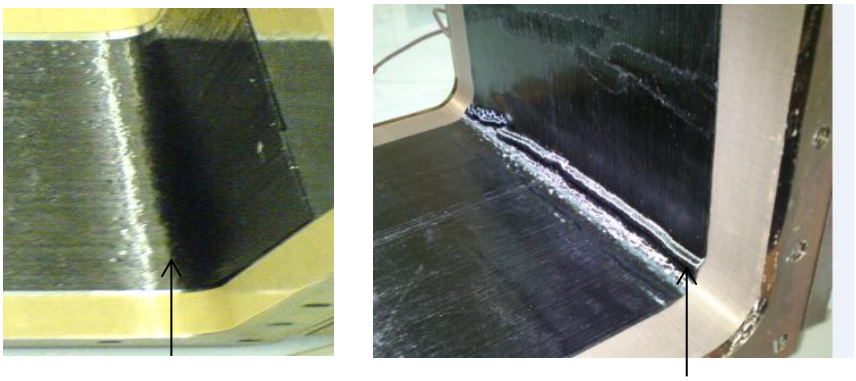
2.3.1. Corner Thickening

It can be seen clearly that in L-and U shaped parts, the resin at regions close to the corner has percolated into the corner, resulting in an increase in thickness of the corners above the nominal value. This phenomenon has also been observed by Hubert and Poursartip [61]. In order to assess the effect of bleeding on corner thickening samples with bleeding and no-bleeding condition were manufactured.

2.3.2. Fibre Wrinkling

Wrinkles are observed in the inner side of the corner of L-shaped laminates, as shown in Figure 2.6b. These wrinkles have negative effect on the strength of the composite parts and affect the amount of the spring-in after curing.

In order to determine the amount of deformation resulting from fibre wrinkling, two lay-up methods were used. First, using the conventional lay-up method, six parts with four-ply thickness were produced. Consistent with this method, the prepregs were laid sequentially layer-by-layer on the mould surface. In the second method, four layers of prepreg were first laid on a flat plate, and then the whole stack was bent to conform to the surface of the L-shaped mould. This method resulted in more fibre wrinkling in the inner surface of the parts as compared to the conventional method. Three unidirectional samples were produced from the conventional method and five unidirectional samples were produced from the alternative method.



(a) (b)

Figure 2.6. Wrinkled fibres during lay-up a) less fibre wrinkling b) more fibre wrinkling

After curing the parts according to MRCC, a water-cooled diamond saw was used to cut specimens (10 mm by 10 mm squares) from the corner and the arms of the manufactured unidirectional and cross-ply L-shaped parts. These trimmed sections were then potted in epoxy and polished by standard metallographic procedures. Digital micrographs were taken of each specimen using a Nikon ECLIPSE NV 150 microscope.

2.3.3. Bagging Condition

In some applications resin bleeding can be preferred to increase the fibre volume fraction. However resin bleeding has an effect on distortion. In order to examine how resin bleeding affects the deformation, some L-shaped composite laminates were manufactured under bleeding and without non-bleeding conditions. For the parts that are manufactured under bleeding condition, the prepreg stack was covered with a peel ply and a breather fabric before applying a vacuum bag. On the other hand for the parts that are manufactured under non-resin bleeding condition, Teflon coated glass fabric release film with a thickness of 0.08 mm was applied over the entire surface of the prepreg stack.

2.3.4. Effect of Stacking Sequence

The magnitude of warpage was compared by changing the stacking sequence of the samples. Bending stiffness of laminates obviously has an effect on distortion, and lower bending stiffness of the composite part causes more distortion. Some cross-ply strip

samples with different stacking sequences were manufactured to show the effect of bending stiffness on warpage. The length and the width of the strips are 300 mm and 50 mm respectively, as shown in Figure 2.7. The stacking sequence of the UD samples are $[90]_4$ and XP samples are $[90/0]_s$ and $[0/90]_s$.

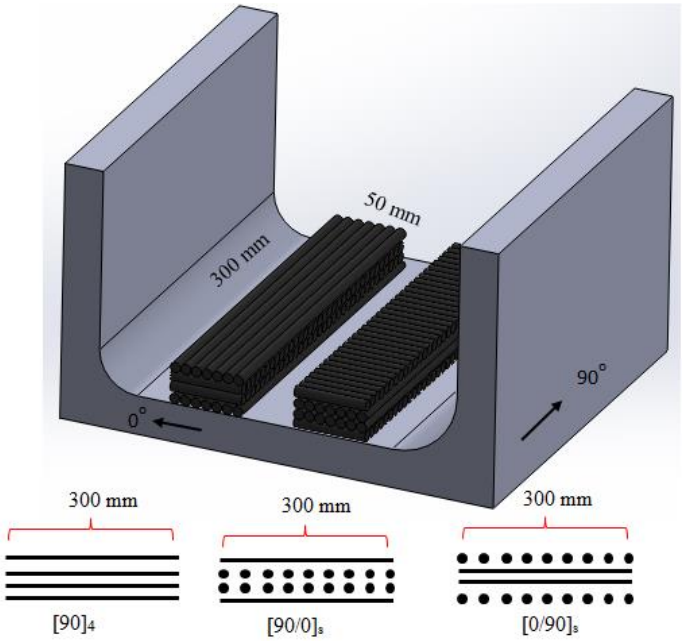


Figure 2.7. Schematic representation of strip placement and stacking configuration.

The effect of stacking sequence on distortion can be seen in L-shaped laminates by examining the warpage of the arms of the samples that have different stacking sequence along different sections such as Section 1 and Section 2, as represented in Figure 2.8.

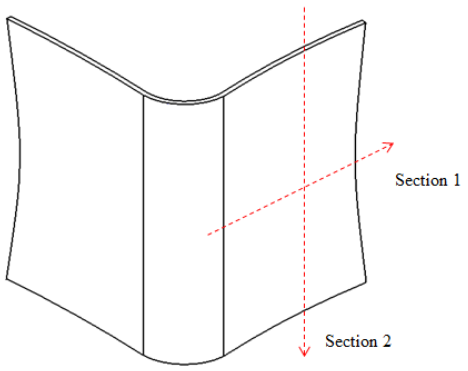


Figure 2.8. Warpage values are measured in Section 1 and Section 2.

3. 2-D FINITE ELEMENT ANALYSIS

A three-step 2-D finite element model including anisotropy in the thermal expansion coefficient, cure shrinkage, consolidation, and tool-part interaction was developed to predict the process induced stresses and deformation. The basic process model was developed and implemented in ABAQUS previously by Ersoy *et al.* [29] by a two-step model that represents the rubbery and glassy states of the resin. In this thesis, a third step is included to represent the viscous state of the resin. The reason for preferring a three-step approach is the complexity of determining continuous development of material properties during the cure cycle. The constitutive equations are based on the Cure Hardening Instantaneously Linear Elastic (CHILE) model previously proposed by Svanberg and Holmberg [84]. In each step constant material properties were used. The two main transitions during the curing process are gelation, occurring at approximately 30 % degree of conversion, and vitrification, occurring at approximately 70 % degree of conversion of the resin [29].

3.1. Steps of Analysis

The resin states with respect to the MRCC is shown in Figure 3.1a together with the glass transition temperature and degree of cure of the resin. The gel point which is defined as the point where the prepreg is cured enough to sustain in-plane shear stresses, and the vitrification point at which the instantaneous glass transition temperature reaches the process temperature are also indicated. The resin is believed to be gelled at around 160 ^{o}C during the second ramp as a sharp rise of the glass transition temperature. The vitrification where the glass transition temperature reaches the process temperature occurs 45 minutes after the 180 ^{o}C soak period starts [75]. The steps of the FE model are shown in Figure 3.1 b. The whole cure stage was divided into three distinct regions according to resin modulus development during curing. Actually resin in the viscous form does not sustain any mechanical loads but the entangled fibres within the resin can bear some mechanical load in the viscous state so that linear elastic behaviour is assumed in the viscous step.

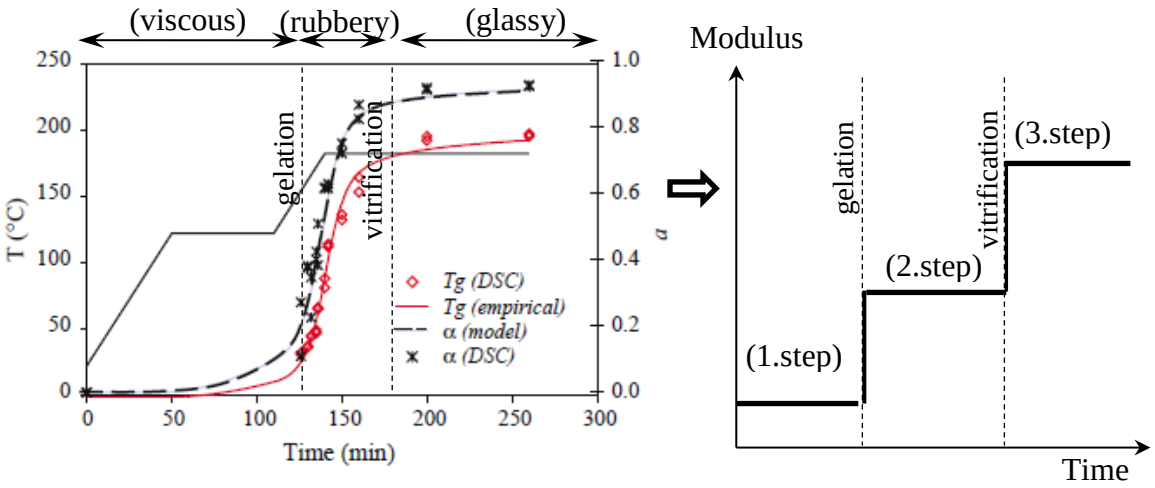


Figure 3.1. a)Various stages of the MRCC, b) Steps of FEM model.

In the first step, before gelation, consolidation takes place as the voids are suppressed, expelled from the composite, and extra resin bleeds out in this step. Due to the difficulty in measuring the mechanical properties in the viscous state, there is no reliable data available for this state in the literature. In order to investigate the effect of the shear modulus in the viscous state, a parametric study is carried out by taking the shear modulus as different fractions of the rubbery shear modulus.

In the second step, between gelation and vitrification, rubbery material properties were used. Due to cross-linking reactions, cure shrinkage takes place during the curing of thermosetting resins, which results in contraction in the through thickness direction.

In the last step, after vitrification, glassy material properties were used in the model. The resin vitrifies and transforms to the glassy state and the resin modulus increases to a magnitude of a few GPa. The stresses developed in the viscous and rubbery states are rearranged as the part is allowed to deform freely as it cools down to room temperature by removing the boundary conditions.

The properties of AS4/8552 composite in the rubbery and glassy states were found in previous work [75] and are shown in Table 3.1. Cure shrinkage and CTE of the composite

in the fibre direction assumed to be zero in Table 3.1. Gelation occurs when the temperature reaches to 160^{o}C during the second ramp and vitrification occurs at 45 min after the start of the second hold at 180^{o}C [29, 75]. The CTE value given in this table for glassy state is the nominal value, and actual values are calculated as a function of corner thickness. To obtain the experimentally measured 0.48% [81] transverse cure shrinkage in the rubbery state, an equivalent negative Coefficient Of Thermal Expansion is used as given in Table 2. In Step-1 and Step-2, an autoclave pressure of 0.7 MPa is applied on the bag surface of the part. In Step-3, the applied pressure is removed, the part is separated from the tool and spring-in and warpage develops. A uniform temperature was assigned to the parts because the temperature range measured across the thickness and in the plane of the part at eight stations was within a 3 ^{o}C band for even the thickest (16 plies) laminates.

Table 3.1.Material properties in the rubbery and the glassy state [29].

Property	**Unit**	**Rubbery**	**Glassy**
E_{11}	MPa	132200	135000
$E_{22} = E_{33}$	MPa	165	9500
$G_{12} = G_{13}$	MPa	44.3	4900
G_{23}	MPa	41.6	4900
$\nu_{12} = \nu_{13}$	-	0.346	0.3
ν_{23}	-	0.982	0.45
α_{11}	με/^{o}C	-	0*
$\alpha_{22} = \alpha_{33}$	με/^{o}C	-31.7	32.6
ε_{11}^{cure}	%	0*	-
$\varepsilon_{22}^{cure} = \varepsilon_{33}^{cure}$	%	0.48	-

*****Assumed to be zero.

3.2. Stress Calculation and Implementation of Mechanical Properties

The material coordinate system is represented in Figure 3.2, where the fibre direction is the *1*-direction, the transverse direction is the *2*-direction, and the through-thickness direction is the *3*-direction.

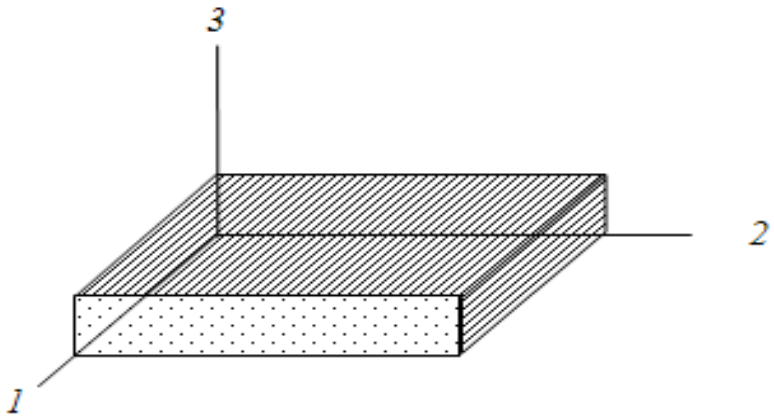


Figure 3.2. The fibre, transverse, and through-the-thickness directions.

The constitutive equation for the composite can be expressed using contracted notation as:

$$\begin{Bmatrix} \sigma_1 \\ \sigma_2 \\ \sigma_3 \\ \sigma_{23} \\ \sigma_{31} \\ \sigma_{12} \end{Bmatrix} = \begin{bmatrix} \frac{(1-\nu_{23}\nu_{32})}{E_2E_3\Delta} & \frac{(\nu_{12}+\nu_{32}\nu_{13})}{E_1E_3\Delta} & \frac{(\nu_{13}+\nu_{12}\nu_{23})}{E_1E_2\Delta} & 0 & 0 & 0 \\ & \frac{(1-\nu_{13}\nu_{31})}{E_1E_3\Delta} & \frac{(\nu_{23}+\nu_{21}\nu_{13})}{E_1E_2\Delta} & 0 & 0 & 0 \\ & & \frac{(1-\nu_{12}\nu_{21})}{E_1E_2\Delta} & 0 & 0 & 0 \\ & \text{Sym.} & & G_{23} & 0 & 0 \\ & & & & G_{31} & 0 \\ & & & & & G_{12} \end{bmatrix} \begin{Bmatrix} \varepsilon_1 \\ \varepsilon_2 \\ \varepsilon_3 \\ \varepsilon_{23} \\ \varepsilon_{31} \\ \varepsilon_{12} \end{Bmatrix} \quad (2.1)$$

where for a transversely isotropic composite, $\nu_{12} = \nu_{13}$, $E_2 = E_3$, $G_{12} = G_{13}$, and $G_{23} = E_2 / 2(1+\nu_{23})$, $\Delta = \dfrac{1-\nu_{12}\nu_{21}-\nu_{23}\nu_{32}-\nu_{31}\nu_{13}-2\nu_{21}\nu_{32}\nu_{13}}{E_1E_2E_3}$

Overall strains in a layer ε_j^t, are expressed as a sum of the mechanically induced strains ε_j^m, thermally induced strains ε_j^{th}, and chemically induced strains ε_j^{ch},

$$\varepsilon_j^t = \varepsilon_j^m + \varepsilon_j^{th} + \varepsilon_j^{ch} \tag{2.2}$$

$$\varepsilon_j^m = \varepsilon_j^t - \varepsilon_j^{th} - \varepsilon_j^{ch} \tag{2.3}$$

Using stress- strain Equation (2.1) the stresses in a layer are given by

$$\sigma_i = \sum_{j=1}^{6} C_{ij}\, \varepsilon_j^m, \qquad i = 1 \dots 6 \tag{2.4}$$

where $C_{ij}$is the stiffness matrix.

The incremental stress tensor $\Delta\sigma_i$ is calculated using the Jacobian matrix $J_{ij}$and is given by

$$\Delta\sigma_i = \sum_{j=1}^{6} J_{ij}\, \Delta\varepsilon_j^m, \qquad i = 1 \dots 6 \tag{2.5}$$

The mechanical properties in each step are different, so these properties are implemented in the analysis by means of a user subroutine UMAT, which updates the elastic properties at the beginning of each step, and the stresses locked-in at each step are added up to find the final stress state after removal from the mould. In this subroutine, during the first step, the material stiffness matrix is calculated using viscous properties and the stresses and strains are calculated. Then the stress is frozen as the material properties are switched from viscous to rubbery, and the new state of stress and strain is calculated using the rubbery stiffness matrix. At the last step, the material stiffness matrix is calculated using glassy properties and the stresses and strains are calculated [29]. The schematic block diagram of UMAT is represented in Figure 3.3.

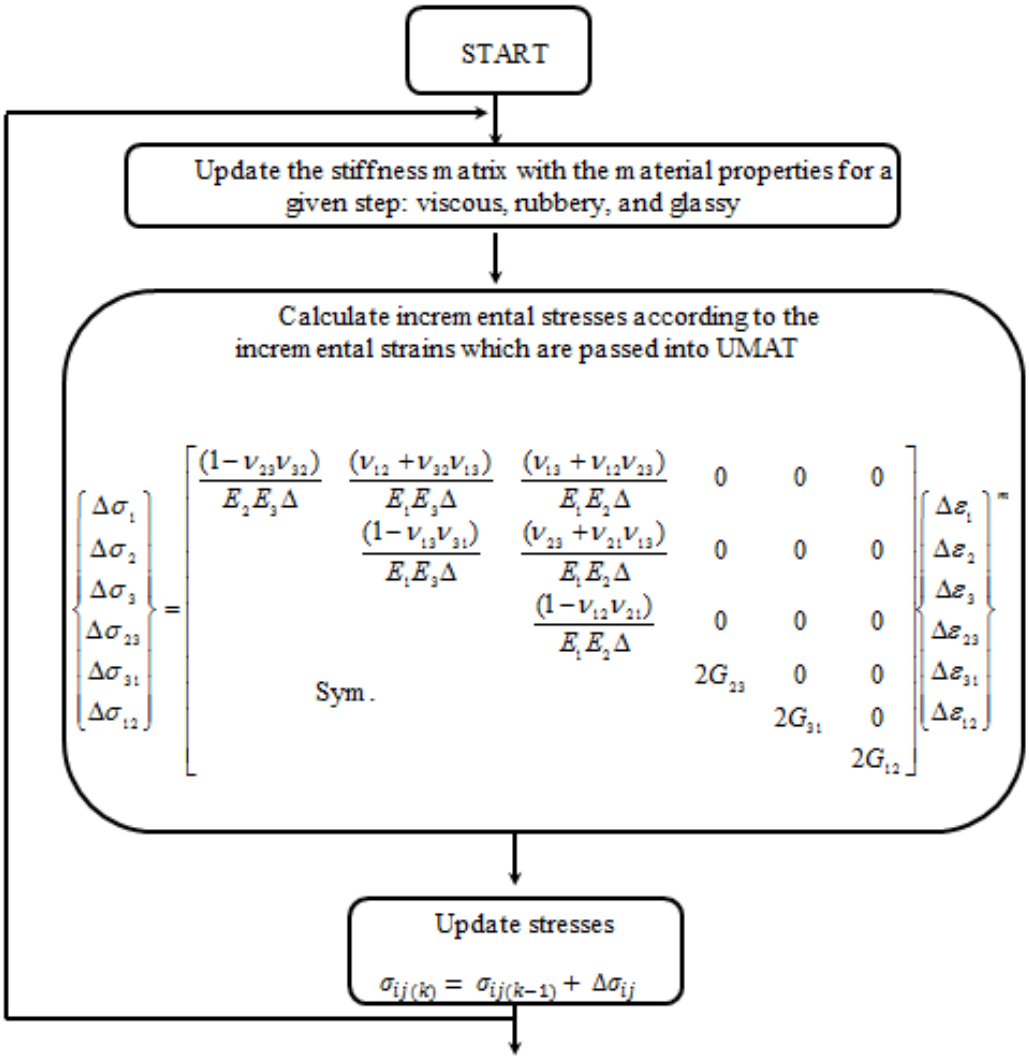


Figure 3.3. Schematic block diagram of UMAT for stress calculation.

The Poisson ratios v_{ij}, is assumed to be zero in the viscous state so that the material Jacobian matrix in the viscous state is given by,

$$J = \begin{bmatrix} E_1 & 0 & 0 & 0 & 0 & 0 \\ & E_2 & 0 & 0 & 0 & 0 \\ & & E_3 & 0 & 0 & 0 \\ & & & 2G_{23} & 0 & 0 \\ & & \text{Sym.} & & 2G_{31} & 0 \\ & & & & & 2G_{12} \end{bmatrix} \tag{2.6}$$

The material Jacobian matrix in the rubbery and glassy state is calculated using the mechanical properties in each state and given by,

$$J = \begin{bmatrix} \frac{(1-\nu_{23}\nu_{32})}{E_2E_3\Delta} & \frac{(\nu_{12}+\nu_{32}\nu_{13})}{E_1E_3\Delta} & \frac{(\nu_{13}+\nu_{12}\nu_{23})}{E_1E_2\Delta} & 0 & 0 & 0 \\ & \frac{(1-\nu_{13}\nu_{31})}{E_1E_3\Delta} & \frac{(\nu_{23}+\nu_{21}\nu_{13})}{E_1E_2\Delta} & 0 & 0 & 0 \\ & & \frac{(1-\nu_{12}\nu_{21})}{E_1E_2\Delta} & 0 & 0 & 0 \\ & \text{Sym.} & & 2G_{23} & 0 & 0 \\ & & & & 2G_{31} & 0 \\ & & & & & 2G_{12} \end{bmatrix} \quad (2.7)$$

3.3. Tool-part Interaction

Tool part interaction is examined in detail by Gartska *et al*. [88] for the same material by means of a method called instrumented ply technique. They found that when the resin is in the viscous state, the tool-part interaction is basically due to fibre friction, and a sliding friction with a constant shear stress of 0.1 MPa prevails. However, once the resin gels, the nature of the interaction changes to a stick-slip type, resulting in a stable state with a constant shear stress of 0.2 MPa at the interface. In the present study, although the tool material and the interface properties are different, constant shear stress of 0.1 MPa and 0.2 MPa are used for viscous and rubbery steps respectively as a reference, since the interfacial stress has not been measured directly, and the effect of varying them is investigated.

Interaction between tool and part is modelled by using ABAQUS mechanical contact interaction modelling capabilities [89]. In the model, contact surfaces are defined for interactions, using the ABAQUS option *SURFACE, and then these surfaces are matched by using the option *CONTACT PAIR. The characteristic of the contacting surfaces are defined by using the option *SURFACE BEHAVIOUR. Interaction normal to the surface is the default “hard” contact relationship, which allows no penetration of the slave nodes

into the master surface and no transfer of tensile stress across the interface. Interaction tangential to the surface is modelled by the classical isotropic Coulomb friction model. The interfacial shear stress is assumed proportional to the contact pressure up to a limiting sliding stress. The constant of proportionality is the friction coefficient, μ and the sliding stress is τ_{max}, shown in Figure 3.4.

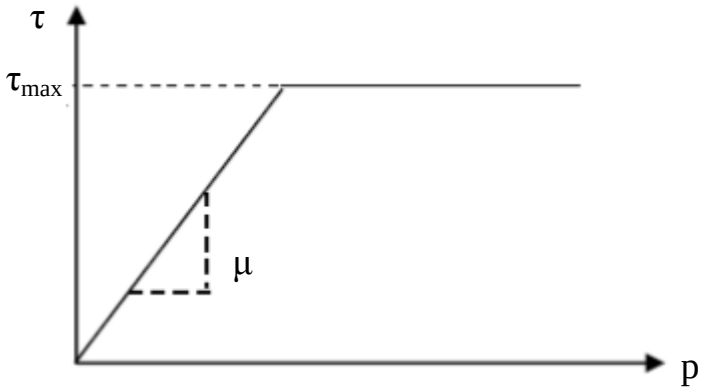


Figure 3.4. Interface friction characteristics.

In the first and the second step of the analysis tool-part interaction is active and in the third step tool-part contact is deactivated. Following the findings of Garstka *et al*. [9], the sliding stress τ_{max} is changed from 0.1 MPa to 0.2 MPa in the second step because the friction behaviour in these two steps (viscous and rubbery) are different.

3.4. Meshing and Boundary Conditions

The L-section-composite parts of 100 mm arm length and 15 and 25 mm corner radius were modelled together with the female steel tool, as shown in Figure 3.5. Only half of the part is modelled by taking advantage of the symmetry condition. A local coordinate system is used so that the 2-axis is aligned with the surface of the tool. The elastic modulus of the tool material was taken to be 200 GPa and thermal expansion coefficient to be $12.6x10^{-6o}C^{-1}$.

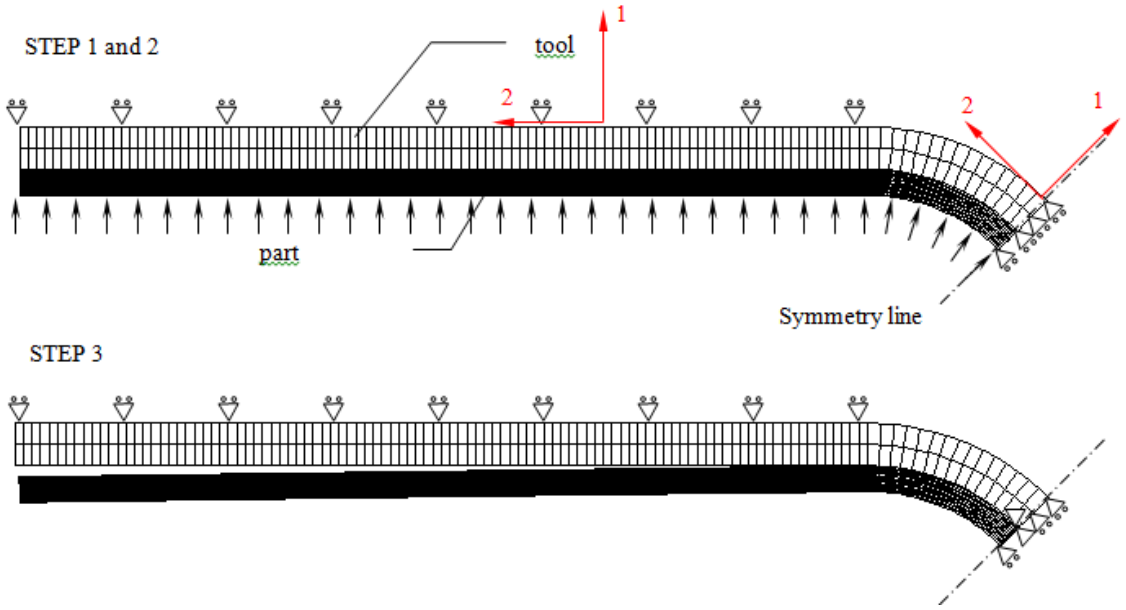


Figure 3.5. The finite element mesh and boundary condition for the L-shaped sections in Step-1and 2 (a) and Step-3 (b).

The elements used in the model are 8-node biquadratic quadrilateral generalized plane strain elements with reduced integration. Aspect ratio of the elements is 5.4 and 3.8 for laminate's flat and curved regions respectively and it is 2.7 for tooling part. The name of the element in ABAQUS is CPEG8R [89]. The generalized plane strain theory used in ABAQUS assumes that the model lies between two planes that can move with respect to each other. It is assumed that the deformation of the model is independent of position with respect to axial direction. The relative motion of the two planes results in a direct strain in the direction perpendicular to the plane of the model only. The defined generalized plane strain elements have an extra node with 3 degrees of freedom; an out-of-plane translation and two rotations. Restraining this node gives a plane strain condition, whereas releasing the node gives no overall stress in the out-of plane direction [89]. In the model, two reference nodes are defined, for the tool and the part, in all the steps for unidirectional parts. These reference nodes are coupled and restrained for rotation in the first and second steps so that the two bounding planes displace with respect to each other but do not rotate, which allows the thermal expansion effect of the tool perpendicular to the plane of the model to be considered, and such restraint prevents the spread of the part on the tool under

pressure in the first and second steps. In cross-ply parts, only one reference node is defined, since the fibres perpendicular to the plane restrain the part from spreading on the tool. In Step-3, removal of the part from the tool is simulated by removing the FE model for tool by the help of *MODEL CHANGE option of ABAQUS, so that the part is now in an overall plane stress condition; the absence of external forces in Step-3 validates this condition. However, in the cross-ply laminates, there are still stresses in the out of plane direction due to the mismatch in CTE values of individual plies in this direction.

The sliding boundary conditions on the flat upper side of the tool enable the tool to expand or contract along the longitudinal direction but prevent free body motion of the tool. On the symmetry line, symmetry boundary conditions are used. Autoclave pressure is applied at the lower side of the laminate as a surface pressure.

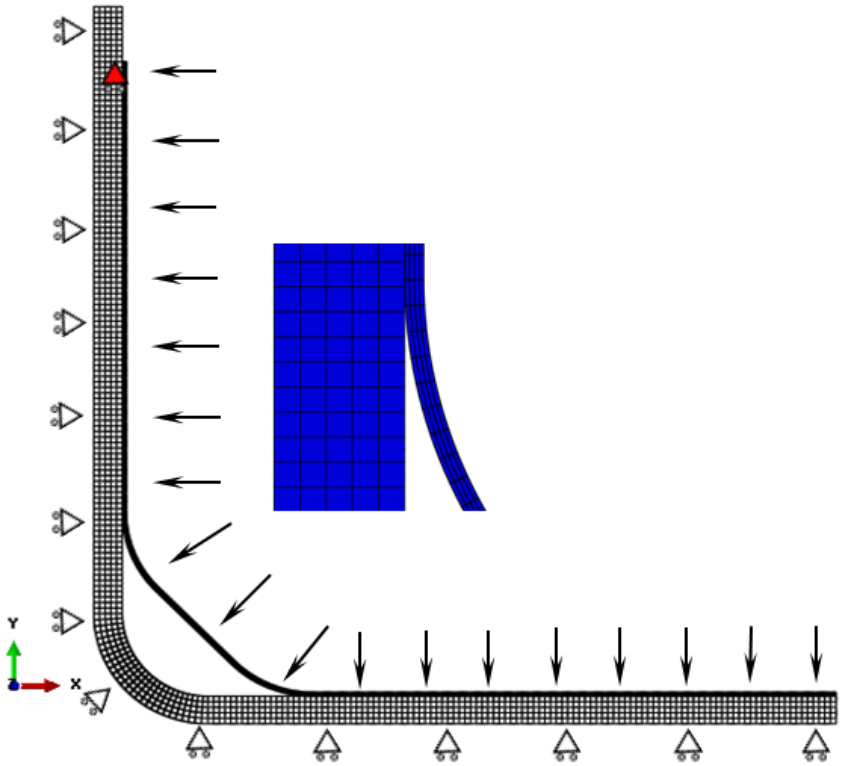
3.5. Implementation of Fibre Wrinkling into FEA

An initial step was added to our previous three-step 2D finite element model for modelling the prepreg placement to explain how initial stresses and strains due to wrinkling affect the resulting residual stresses and deformations. This study includes the initial step and the reduction of the elastic modulus along the fibre direction in the first and second steps, in addition to the three-step model.

In the initial step of the model, the part was made to conform to the mould on the curve side using mechanical loading. The aim was to create compressive strains inside the part, especially on the curve side, to represent the fibre wrinkles. A pressure of 0.4 MPa was applied to the inner surface, and was enough for the part to conform to the mould surface in the curved region. The meshing and loading conditions used can be seen in Figure 3.6.a. The elements used in the model were 8-node biquadratic quadrilateral generalized plane strain elements with reduced integration (CPEG8R). Interactions between the tool and the part were modelled using ABAQUS' mechanical contact interaction modelling capabilities. The interaction normal to the surface was the default "hard" contact relationship, which allowed no penetration of the slave nodes into the master surface, and no transfer of tensile stress across the interface. The tangential

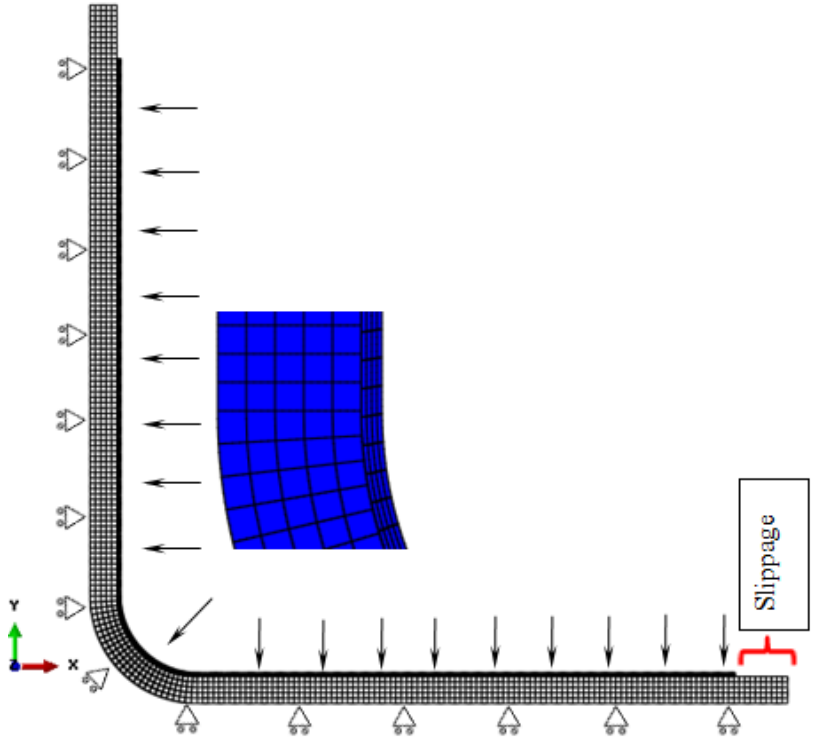
interaction was set to be frictionless in the initial step. At the end of the initial step (after conformation), all strain values were retained whereas all stress values were set to zero; it was assumed that an uncured prepreg does not sustain any mechanical stress under compressive loading during the initial conformation.

The loading conditions and the shape of the part taking the form of the mould at the curved region are shown in Figure 3.6b for the first (viscous) and second (rubbery) step. In the current model, the elastic modulus of the prepreg along the fibre direction (E_{11}) was reduced at the curved region where compressive strains occur due to the initial conformation of part. This can be justified on the basis that for a ply with non-straight fibres, a smaller elastic modulus is expected. Non-straight fibres are not able to sustain mechanical load in the viscous and rubbery states of the resin. In order to see the effect of this reduction on the deformation, the elastic modulus in the fibre direction was reduced by factors of two and ten in the viscous and rubbery steps, respectively. The compressive strains after the initial step, and the elements that have reduced elastic moduli, are shown in Figure 3.7.

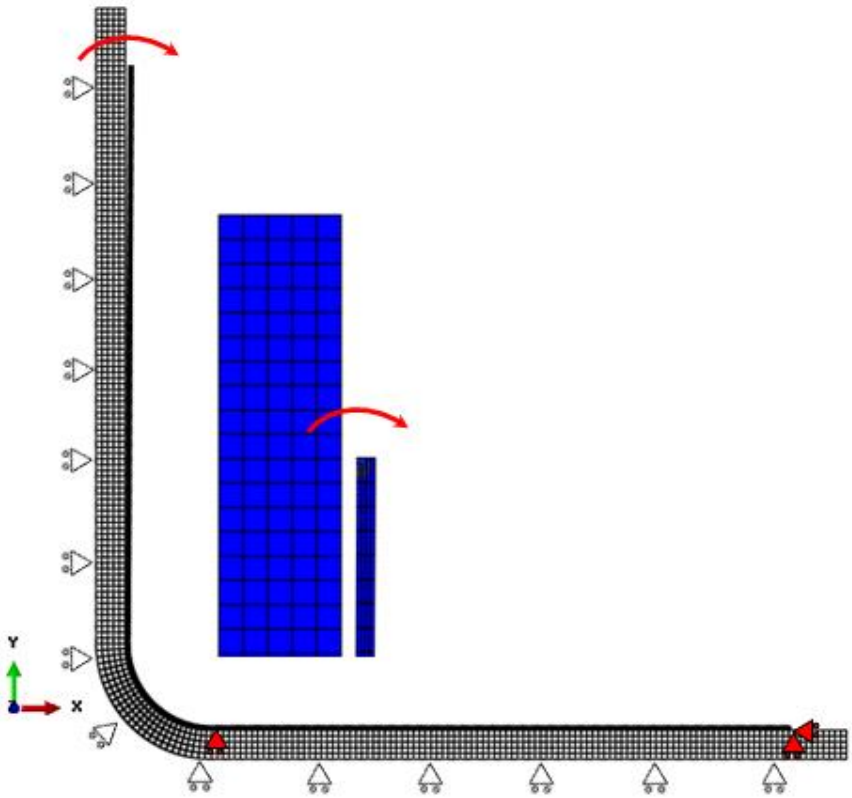


a) Loading, boundary conditions and meshing for initial step.

Figure 3.6. FEM steps of the model.



b) Loading, boundary conditions and meshing for the first and second step.



c) Loading, boundary conditions and meshing for the last step.

Figure 3.6. FEM steps of the model (cont.).

In the third step, part was hold from two points to prevent free motion in space, shown in Figure 3.6c. Glassy material properties were used in this step. Since the resin was in the glassy state at this point and held the fibres that were able to sustain mechanical loads, the elastic modulus in the fibre direction (E_{11}) was assigned its full value even though wrinkles were observed at the end of the process.

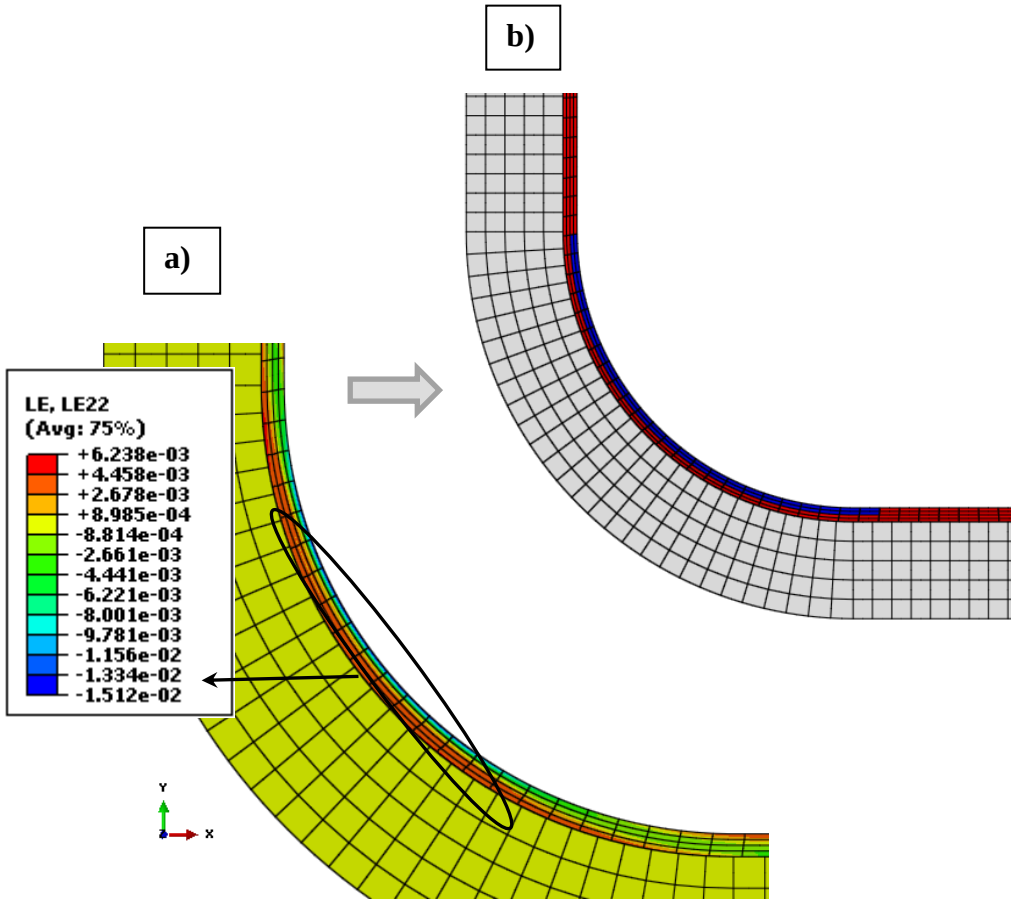


Figure 3.7. a) compressive strains occurred after initial step, b) reduction of elastic modulus for the elements that have compressive strains.

4. 3-D FINITE ELEMENT ANALYSIS

Experimental results show that a simple two dimensional analysis is not sufficient to capture the complex distortion patterns. Spring-in values are not constant along the length of the parts so that a 3D Finite Element model has been developed for predicting shape distortions during curing of fibre reinforced composite parts. The total curing process is divided into three steps that corresponds the states that resin is passing through during curing: viscous, rubbery, and glassy. The material property changes during curing are implemented in the model through a three-step user subroutine. Composite parts of various geometries (U-section, L-section and flat laminates), stacking sequences, and thicknesses are manufactured. These parts were scanned using a 3D laser coordinate scanner to obtain the geometry of the distorted parts to compare to the results of 3D FEA.

The three-step 3-D finite element model is same as the three-step 2-D finite element model including anisotropy, cure shrinkage, consolidation, and tool-part interaction. The only difference is the number of dimension of the model. The finite element analysis is explained in detail in the previous chapter. Meshing and boundary conditions are explained in the following sections.

4.1. Meshing and Boundary Conditions for L Section Parts

L-section parts are modelled with only a quarter of the full part by using symmetry boundary conditions. The symmetry planes and symmetry boundary conditions are shown in Figure 4.1. The sliding boundary conditions on the back side of the tool enable the tool to expand or contract along in plane directions (*Y* and *Z*) at flat section and tangential (*T*) and axial (*Z*) directions at curved region but prevent free body motion of the tool. The tool can extend or contract freely. Contact elements are used between the ply and the tool. The tool-part interaction is explained in Section 3.3 to be sliding with constant shear stress and is assumed to be same for the two in-plane directions. Autoclave pressure is applied as a surface pressure on the laminate. Boundary conditions can be seen in Figure 4.2.

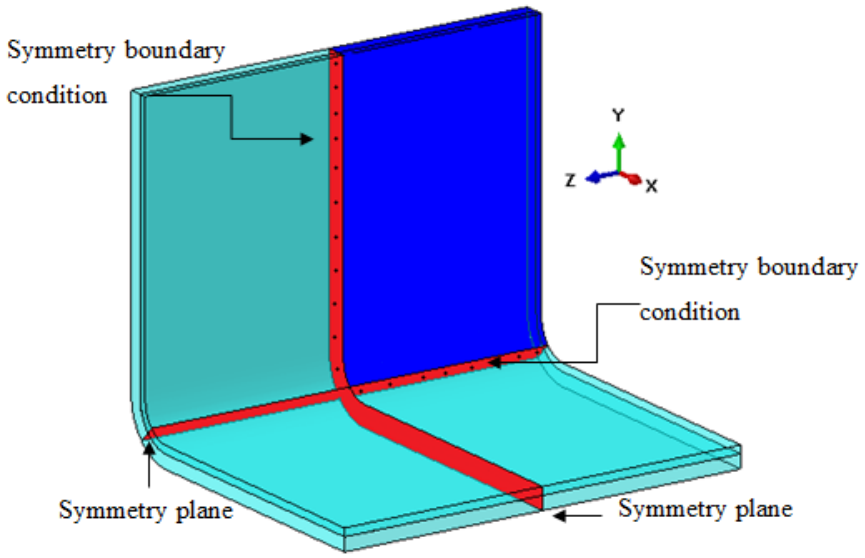


Figure 4.1. 3D modelling of L shape parts.

The sliding boundary conditions on the back side of the tool enable the tool to expand or contract along in plane directions (*Y* and *Z*) at flat section and tangential (*T*) and axial (*Z*) directions at curved region but prevent free body motion of the tool. The tool can extend or contract freely. Contact elements are used between the ply and the tool. The tool-part interaction is explained in Section 3.3 to be sliding with constant shear stress and is assumed to be same for the two in-plane directions. Autoclave pressure is applied as a surface pressure on the laminate. Boundary conditions can be seen in Figure 4.2.

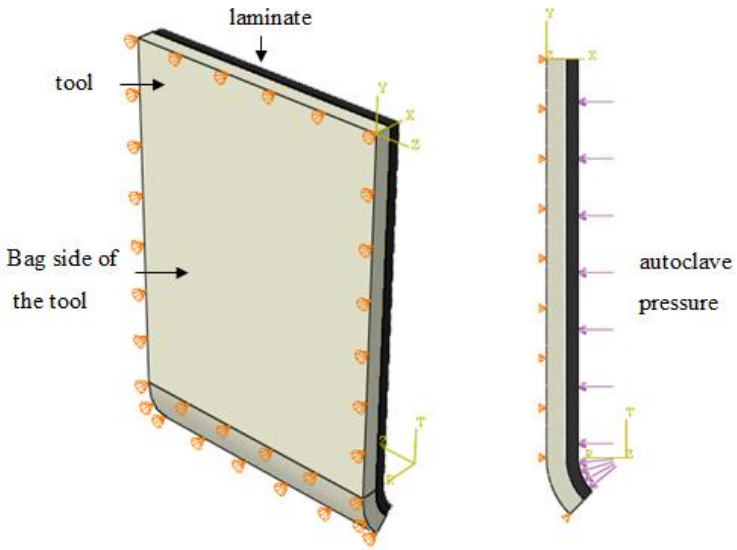


Figure 4.2. Loading and boundary conditions for L shaped parts.

Each ply is represented by one element through the thickness. A 4-ply laminate is shown in Figure 4.3. 8 Node Linear Brick Elements (C3D8) and 20 Node Reduced Quadratic Brick Elements (C3D20R) are used.

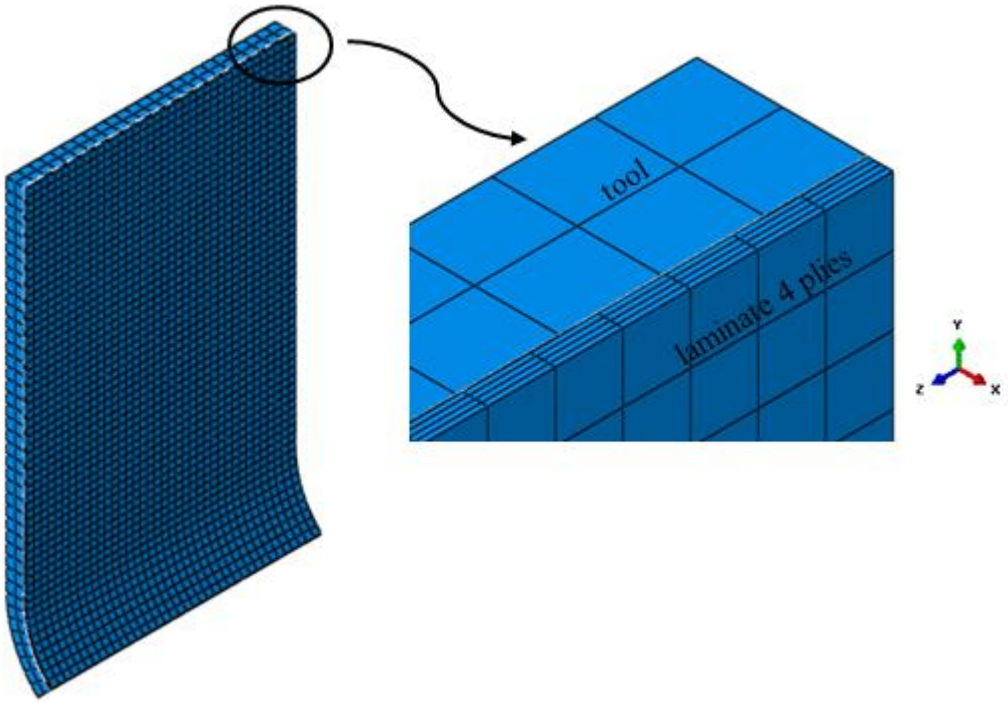


Figure 4.3. Finite element mesh for the tool and 4-ply laminate.

A convergence study was performed I order to find the optimum mesh size. CPU times and deformation at the tip of a laminate were compared between C3D8 and C3D20R elements for UD4R25 sample (4-ply L shaped unidirectional laminate) by changing the element size. The results were represented in Table 4.1. According to mesh convergence all 3D analysis were done using C3D20R elements of 3x3 mm

Table 4.1. Mesh convergence for UD R25 4 plies L shaped part.

Element type	Tip deflection (mm)	Element size (mm)	Number of elements through length direction	Number of.elements through thickness direction	Aspect ratio	CPU times (h)*
C3D8	0.730	3x3	25	4	16.30	0.012
C3D8	0.882	2x2	38	4	10.86	0.024
C3D8	1.124	1x1	75	4	5.43	0.140
C3D8	1.216	0.5x0.5	150	4	2.71	0.517

Table 4.1. Mesh convergence for UD R25 4 plies L shaped part (cont.).

C3D8	1.241	0.25x0.25	300	4	1.36	11.613
C3D20R	1.221	3x3	25	4	16.30	0.094
C3D20R	1.227	2x2	38	4	10.86	0.236
C3D20R	1.234	1x1	75	4	5.43	1.819
C3D20R	1.212	2x2	38	8	21.73	0.513

Material orientation for 4 ply cross-ply laminate (XP4) is shown in Figure 4.4. For this stacking sequence the bottom and the upper plies are fibre dominated along 1 direction, whereas the plies between the bottom and upper ply are resin dominated along the 1 direction.

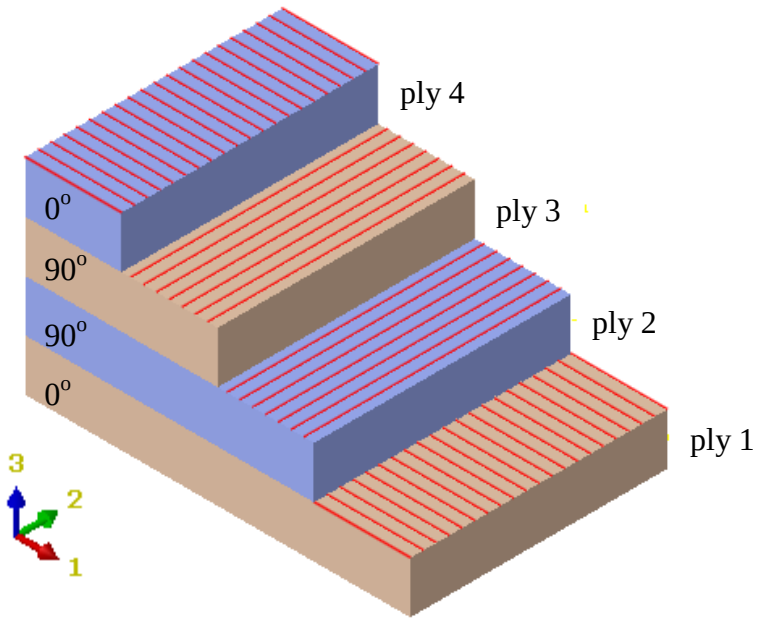


Figure 4.4. Material orientation used in ABAQUS for 4 -ply cross-ply laminate (XP4) with the designation of $[0/90]_s$

4.2. Meshing and Boundary Conditions for U Section Parts

U-section parts are modelled with half of the full part by using symmetry boundary conditions. The symmetry planes and symmetry boundary conditions are shown in Figure 4.5. Because of the unequal radii on the two corner sections, there is only one symmetry plane. Contact elements are used between the ply and the tool. The tool-part interaction is

explained in Section 3.3 to be sliding with constant shear stress and is assumed to be same for the two in-plane directions.

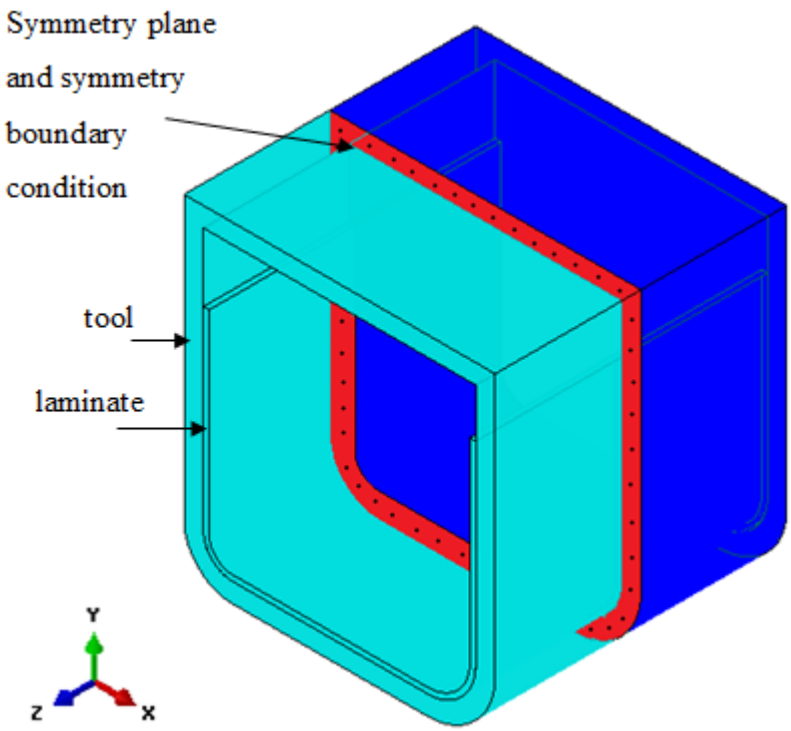


Figure 4.5. Symmetry boundary condition for U shaped parts.

The sliding boundary conditions on the back side and bottom side of the tool enable the tool to expand or contract along the in plane directions (*Y* and *Z*) at left flat surface, in plane directions (*X* and *Z*) at the bottom flat surface and the tangential (*T*) and the axial (*Z*) directions at curved region but prevent free body motion of the tool. The tool can extend or contract freely. Contact elements are used between the ply and the tool. The tool-part interaction is explained in Section 3.3 to be sliding with constant shear stress and is assumed to be same for the two in-plane directions. Autoclave pressure is applied as a surface pressure on the laminate. Boundary conditions and autoclave pressure can be seen in Figure 4.6.

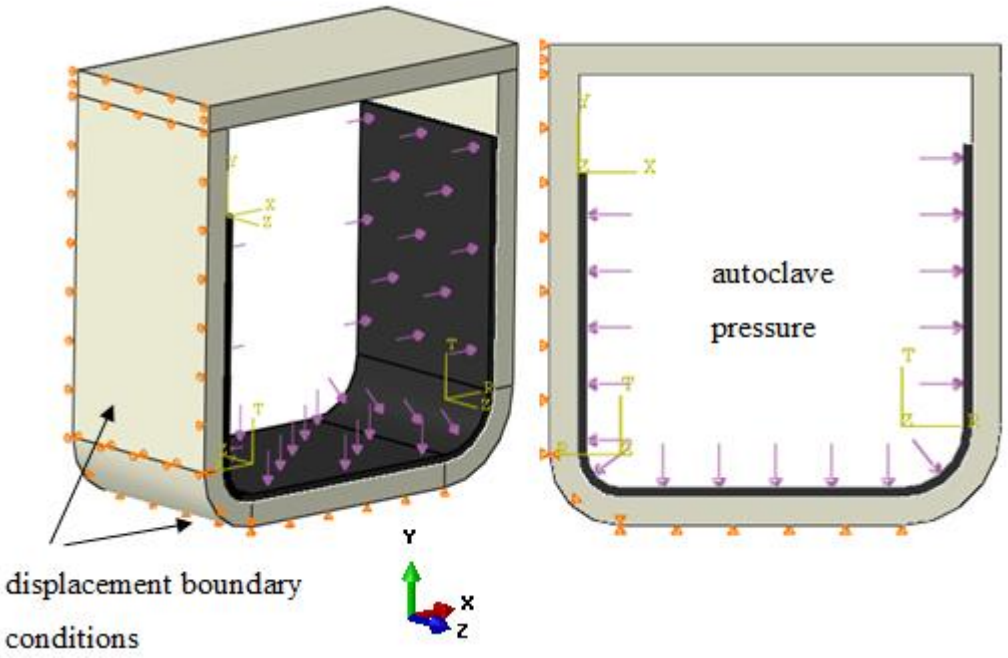


Figure 4.6. Loading and boundary conditions for U shaped parts.

4.3. Meshing and Boundary Conditions for Flat Parts

Flat strip parts are modelled with quarter of the full part by using symmetry boundary conditions. The symmetry planes and symmetry boundary conditions are shown in Figure 4.7.

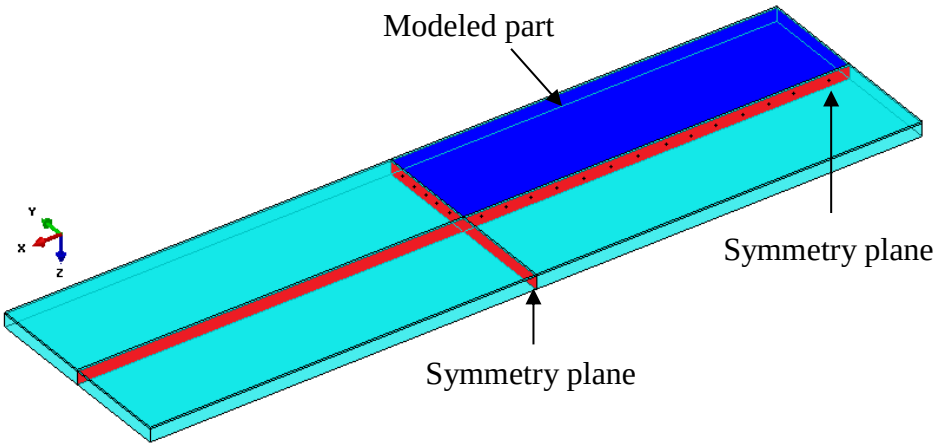


Figure 4.7. The symmetry planes and symmetry boundary conditions for flat strips parts.

The sliding boundary conditions applied on the bottom surface of the tool that enables the tool to expand or contract along the in plane directions (x and y). The tool can extend or contract freely. Autoclave pressure is applied as a surface pressure on the upper surface of the laminate. Contact elements are used between the ply and the tool. The tool-part interaction is explained in Section 3.3 to be sliding with constant shear stress and is assumed to be same for the two in-plane directions. Boundary conditions and applied autoclave pressure can be seen in Figure 4.8.

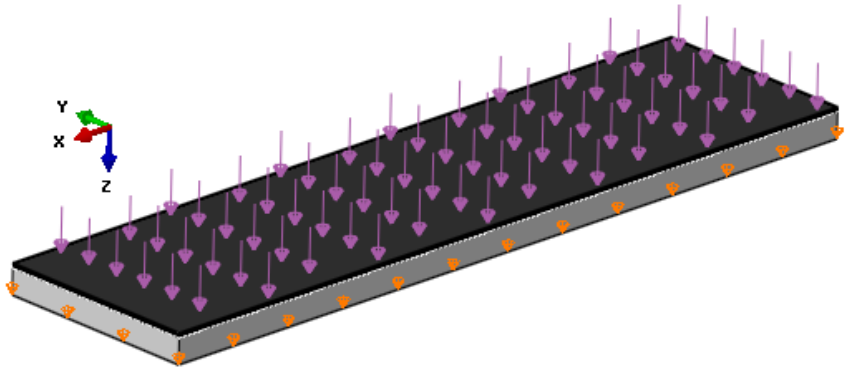


Figure 4.8. Loading and boundary conditions for flat strip parts.

5. RESULTS AND DISCUSSION

In this study, composite parts of various shapes were produced and finite element models were developed in order to predict process induced deformations and the predictions and measurements are then compared to assess the validity of assumptions behind the model. In this context, various experiments were also performed to understand the deformation mechanisms. Some experiments were carried out to determine how the amount of deformation is affected by the factors such as manufacturing method, thickness of the laminate, and stacking sequence of the laminate.

5.1. Observations on Parts Manufactured

5.1.1. Corner Thickening

The corner thickening can be seen easily from the scanned 16-ply thick parts in Figure 5.1 and 5.2. It can be seen clearly that the resin at regions close to the corner has percolated into the corner, resulting in an increase in thickness of the corners above the nominal value. This phenomenon has also been observed by Hubert and Poursartip [61].

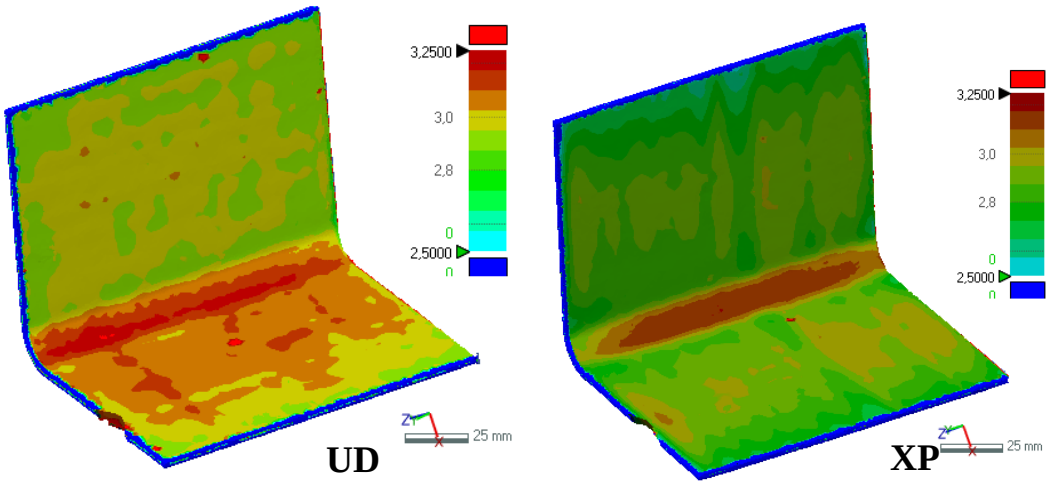


Figure 5.1. Thickness variation for UD16-R15 laminate and XP16-R15 The scale is in mm.

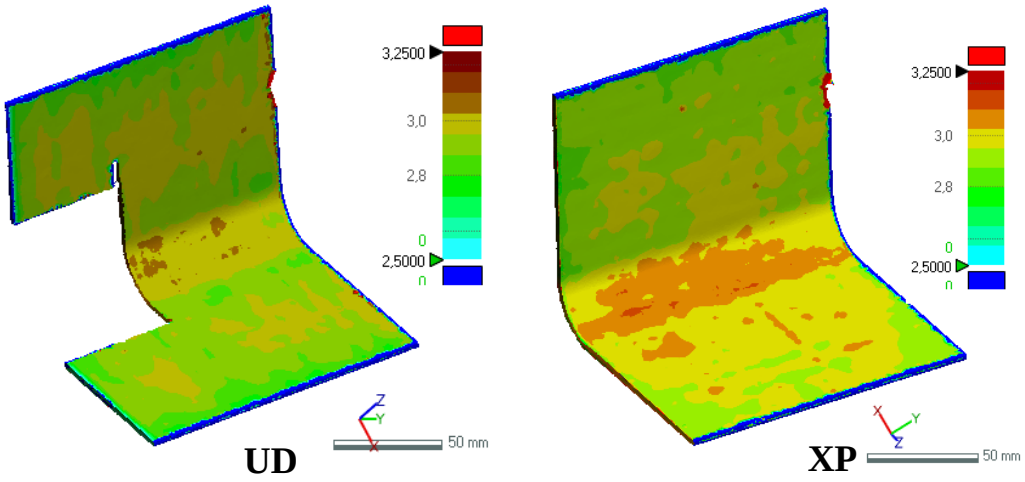


Figure 5.2. Thickness variation for UD16-R25 laminate and XP16-R25. The scale is in mm.

The corner thickening from the thickness measurement along the length of the laminates is represented in Figure 5.3. This figure shows the thickness at the mid-section normalized by the nominal thickness along the part. The parts with 15 mm radius have greater corner thickening as compared to the parts with 25 mm radius and unidirectional parts have greater corner thickening compared to cross-ply parts. The resin flow is lower in cross-ply parts compared to unidirectional parts due to the fact that the cross fibres block the resin movement along the length direction.

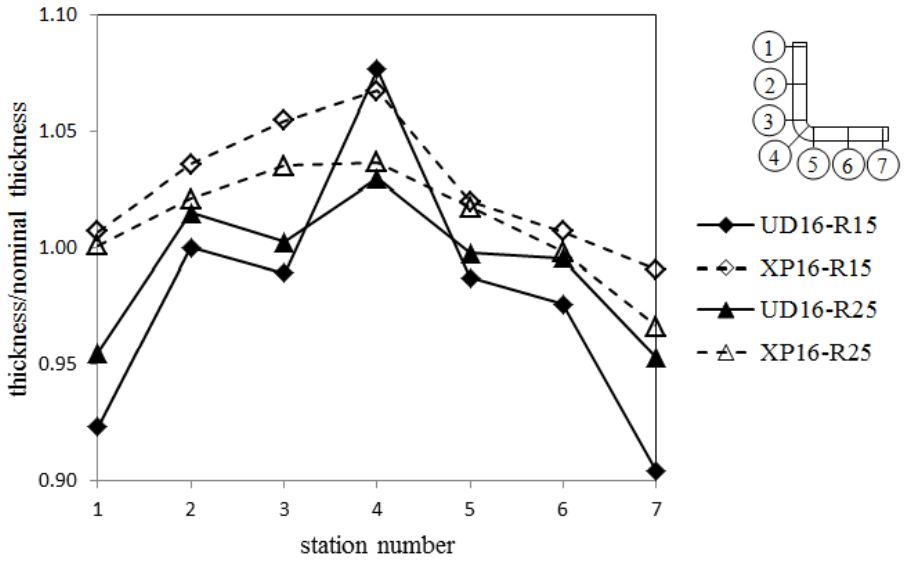
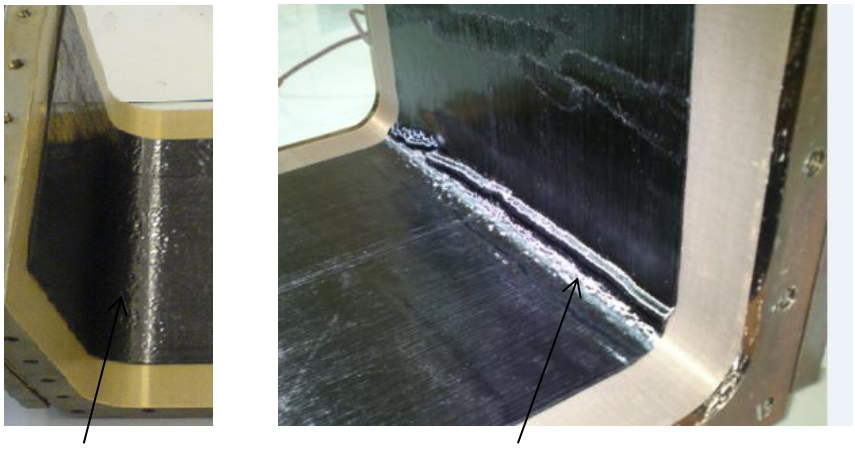


Figure 5.3. Thickness measurement at the mid-section of the laminates.

5.1.2. Fibre Wrinkling

In order to determine the amount of deformation resulting from fibre wrinkling, two lay-up methods were used. First, using the conventional lay-up method, six parts with four-ply thickness were produced. Consistent with this method, the prepregs were laid sequentially layer-by-layer on the mould surface. In the second method, four layers of prepreg were first laid on a flat plate, and then the whole stack was bent to conform to the surface of the L-Shaped mould. This method resulted in more fibre wrinkling in the inner surface of the parts as compared to the conventional method. Three unidirectional samples were produced from the conventional method and five unidirectional samples were produced from the alternative method.

More wrinkling occurred on the curved region of the L-shaped part manufactured using the alternative lay-up procedure as compared to the conventional lay-up procedure. The photographs taken after lay-up using the two methods are shown in Figures 5.4a and 5.4b. A photograph taken from a part manufactured with the conventional lay-up method is given in Figure 5. 4a, and a corresponding photograph for the alternative lay-up method is given in Figure 5.4b. More fibre buckling in the through-thickness direction can be clearly seen in Figure 5.4b.



a) less fibre wrinkling b) more fibre wrinkling

Figure 5.4. Observed wrinkled fibres during lay-up.

Fibre wrinkles were observed after the laying-up of every single ply. These wrinkles changed to in-plane fibre waviness after rolling and applying vacuum and pressure in the autoclave. The schematic representation of this mechanism is shown in Figure 5.5.

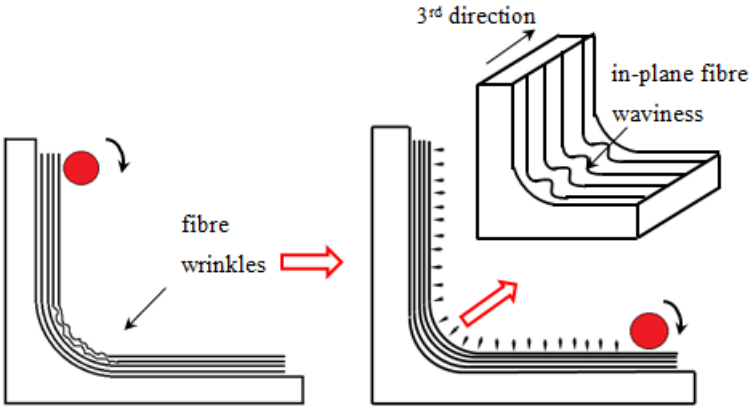
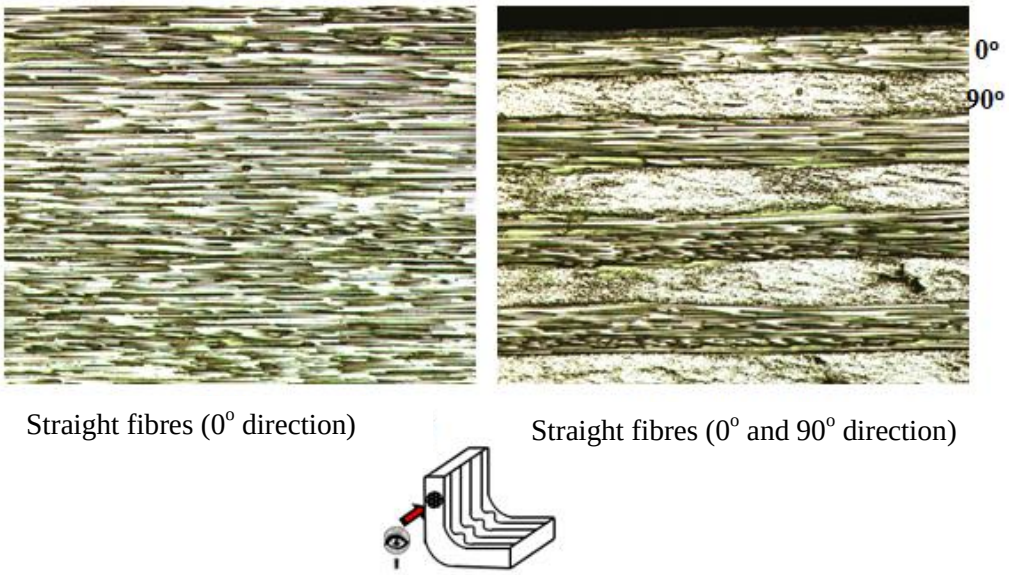


Figure 5.5. Initial fibre wrinkles convert to in-plane fibre waviness after curing.

Some micrographs of the arm and corner regions were taken from unidirectional and cross-ply parts with corner radii of 15 mm. In Figure 5.6, micrographs of the arm regions of a part manufactured by the conventional lay-up method are presented. It can be seen that all fibres are straight and parallel for both stacking sequences at the flat arms of the parts. There is neither fibre wrinkling nor in-plane fibre waviness in the flat arm of the L-shaped unidirectional and cross-ply parts.



Straight fibres (0^o direction)

Straight fibres (0^o and 90^o direction)

Figure 5.6. Photomicrograph at 5x magnification from the arm of the L-shaped laminate. The left one is 4 plies unidirectional $[0]_4$ laminate and the right one is 12 plies cross-ply $[0/90]_{3s}$ laminate.

Micrographs captured from the corner side of the unidirectional and cross-ply parts laid up by the conventional method are shown in Figure 5.7. These micrographs reveal that there is in-plane fibre waviness within the plies that extends along the circumferential direction (0^o direction) for both stacking sequences. In some regions an elliptical shape of the buckled fibres can be seen, which reveals the in-plane fibre waviness. These regions are highlighted in Figure 5.7.

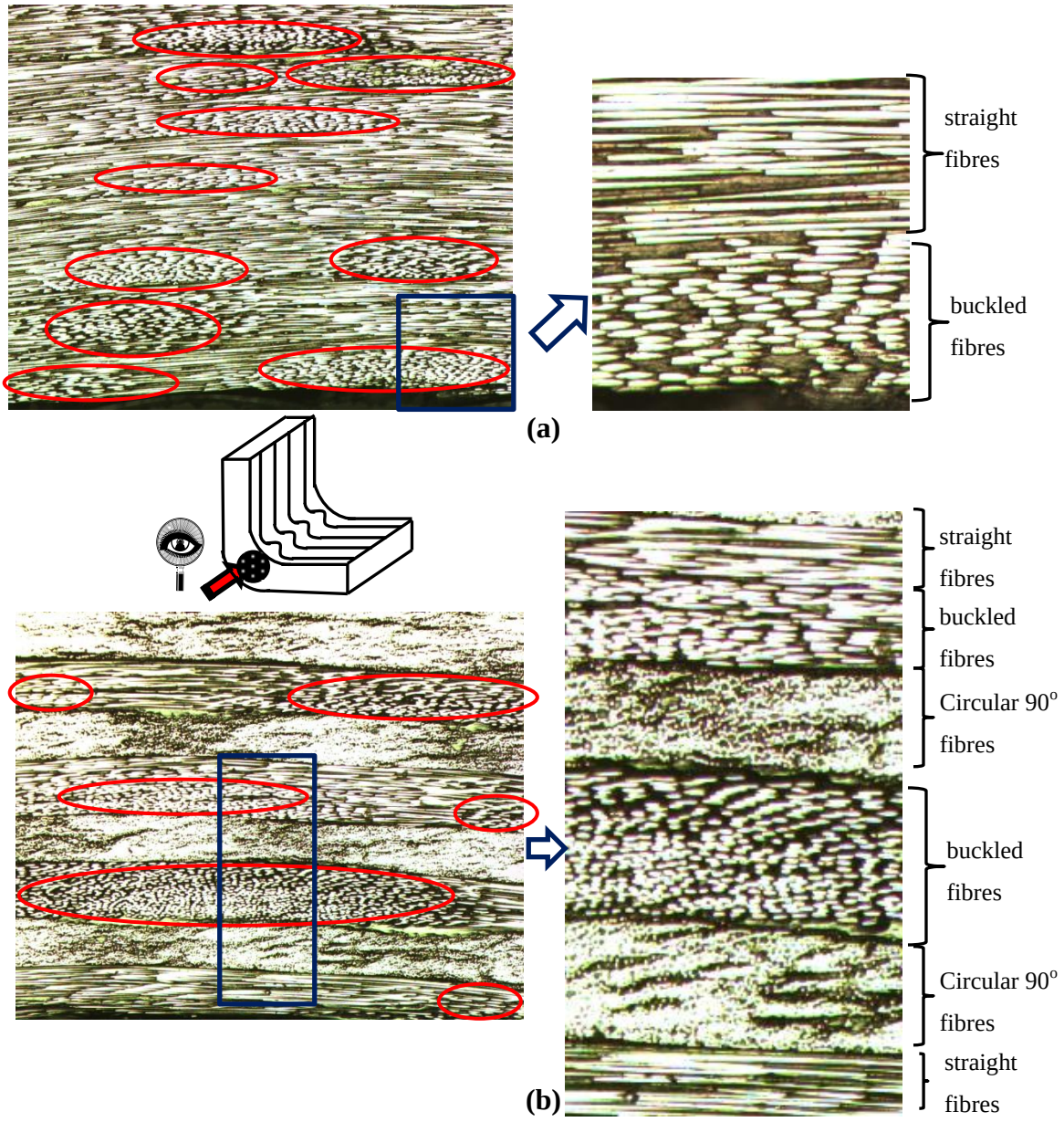


Figure 5.7. Photomicrograph at 5x magnification from the corner of the L-shaped laminate. The upper one (a) is 4 plies unidirectional $[0]_4$ laminate and the lower one (b) is 12 plies cross-ply $[0/90]_{3s}$ laminate.

Micrographs captured from the corner side of the unidirectional parts laid up by the alternative method are shown in Figure 5.8. Most regions include buckled fibres with an elliptical shape throughout the thickness of the curved region of the part.

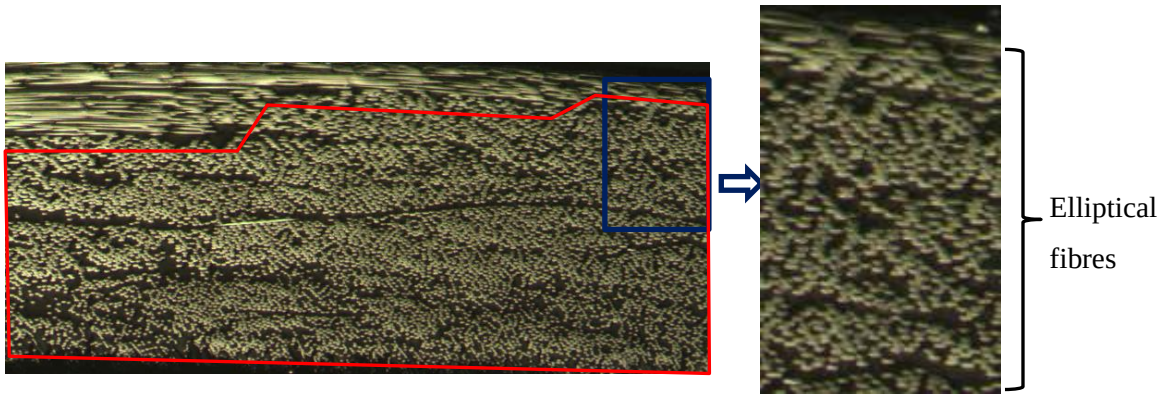


Figure 5.8. Photomicrograph at 5x magnification from the corner of the L-shaped 4 plies unidirectional $[0]_4$ laminate that manufactured in the second way of lay-up.

Spring-in values taken at various stations along the 3rd direction (perpendicular to the curved region) were measured for unidirectional 4–ply thick ($[0]_4$) parts, and are compared for the two lay-up methods in Figure 5.9 for a 15 mm corner radius and in Figure 5.10 for a 25 mm corner radius. The 3rd direction was indicated in Figure 5.5, and the fibres run along the radius from one arm to the other. Using the conventional lay-up method, 3 unidirectional parts with 4 plies were produced, whereas 5 unidirectional parts with 4 plies were produced using the alternative lay-up method. Each part has 0.736 mm thickness. It is observed in Figures 5.9 and 5.10 that less spring-in occurs for the parts that have more in-plane fibre waviness due to the initial fibre wrinkling. In these figures, the dashed lines represent the spring-in values for the parts that have more fibre waviness, laid up by the alternative method. The reason behind this can be explained by two phenomena. The first is that there are compressive strains in the inner corner side after laying-up. These initial circumferential compressive strains at the inner surface of the corner region reduce the residual tensile stresses occurring due to fibre bridging, cure shrinkage and thermal anisotropy. In-plane waviness of the fibres at the corner side can be helpful for maintaining the same arc length during curing, which in turn decreases the amount of in-plane stress and causes smaller spring-in values. The second reason is the low bending stiffness due to fibre waviness at the corner side. Residual stresses occurring due to tool-part interaction cause the parts to spring-out. More fibre waviness results in less bending stiffness.

Therefore, spring-out values increase due to the low bending stiffness. The total amount of spring-in including all effects was reduced.

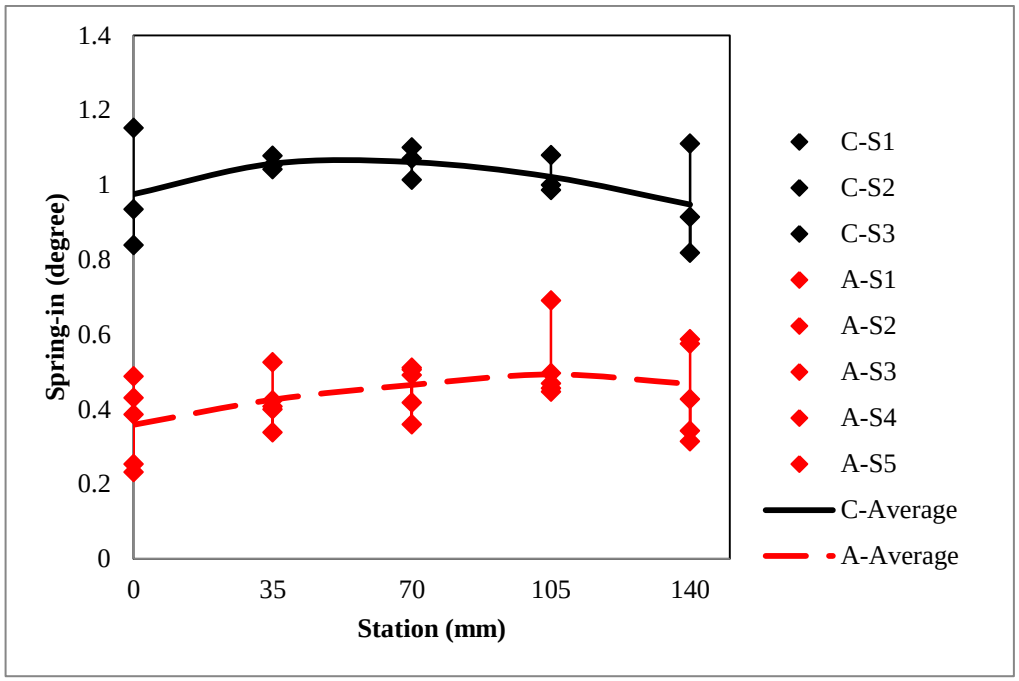


Figure 5.9. Measured spring-in for $[0]_4$ L-section parts with R15 mm corner radius.

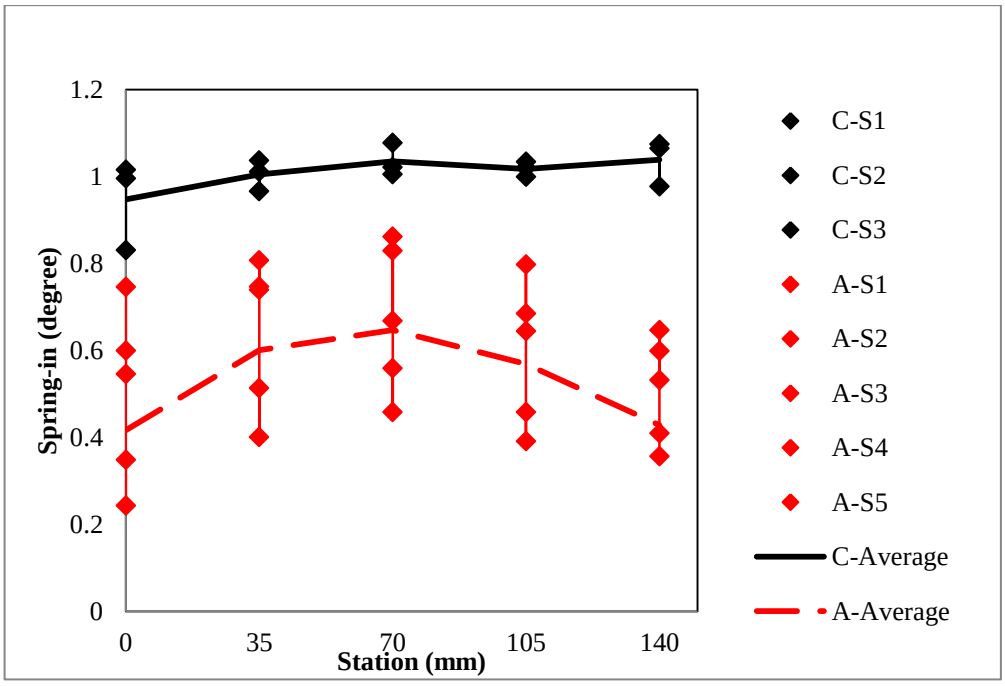


Figure 5.10. Measured spring-in for $[0]_4$ L-section parts with R25 mm corner radius.

5.1.3. Bagging Condition

In some applications resin bleeding can be preferred to increase the fibre volume fraction. However resin bleeding is known to be a cause of shape distortion. In order to examine how resin bleeding affects the deformation, some L-shaped and flat strip composite laminates were manufactured under bleeding and non-bleeding conditions. For the parts that are manufactured under bleeding condition, the prepreg stack was covered with a peel ply and a breather fabric before applying a vacuum bag. For the parts that are manufactured under non-bleeding condition, Teflon coated glass fabric release film with a thickness of 0.08 mm was applied over the entire surface of the prepreg stack.

Flat strip were manufactured under resin bleeding and non- bleeding conditions composite laminates with dimensions of 300 mm x 50 mm, and the warpage of these flat strips are in Figure 5.11- 5.13. The stacking sequence of the UD samples are $[90]_4$ and XP samples are $[90/0]_s$ and $[0/90]_s$. For the parts that manufactured under resin bleeding condition gave more warpage for all configurations as compared to the no-bleeding condition. The reason for this is Fibre Volume Fraction (FVF) gradients resulting from resin bleeding from the bag side. Resin is at the liquid state at the beginning of the processing cycle, so that it moves and bleed through the thickness direction into the bleeder placed on the prepreg stack. Consequently local FVF gradients occur inside the laminate. For the flat parts, resin rich regions are formed at the tool side of the laminate while resin poor regions are formed at the bag side of the laminate. The thermal expansion coefficient of the laminate can vary through the thickness if there is a FVF gradient through the thickness because CTEs depends on FVF. The low CTE at the upper side of the laminate results in less shrinkage as compared to lower side of the laminate during the cool down. This unsymmetrical behaviour causes a concave-up warpage for the flat parts.

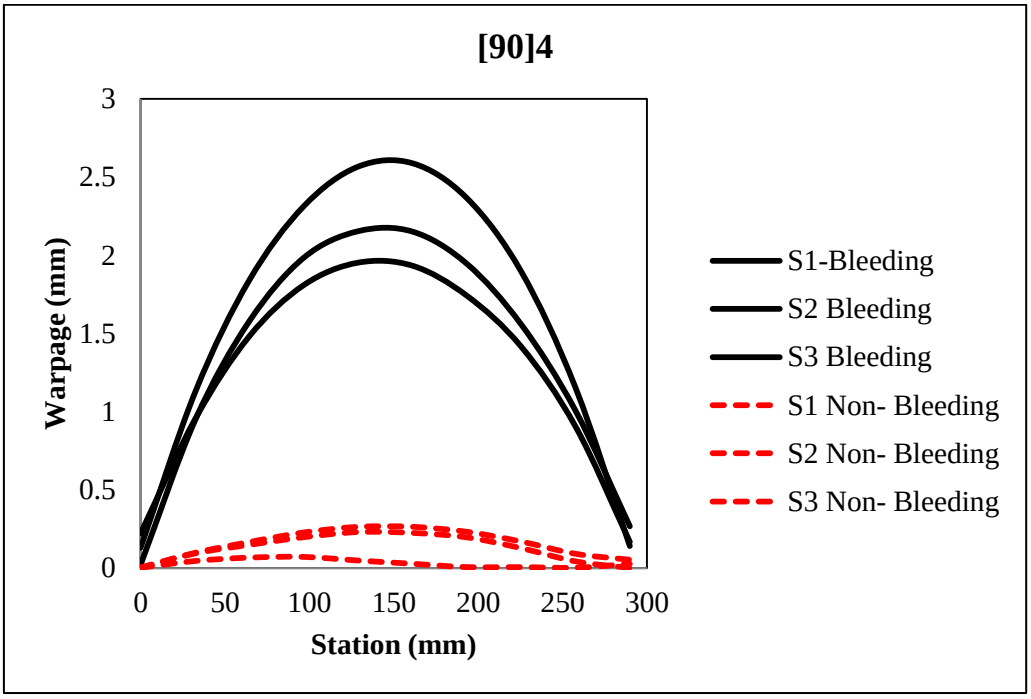


Figure 5.11. Measured warpage in the fabricated strips of UD4 plies.

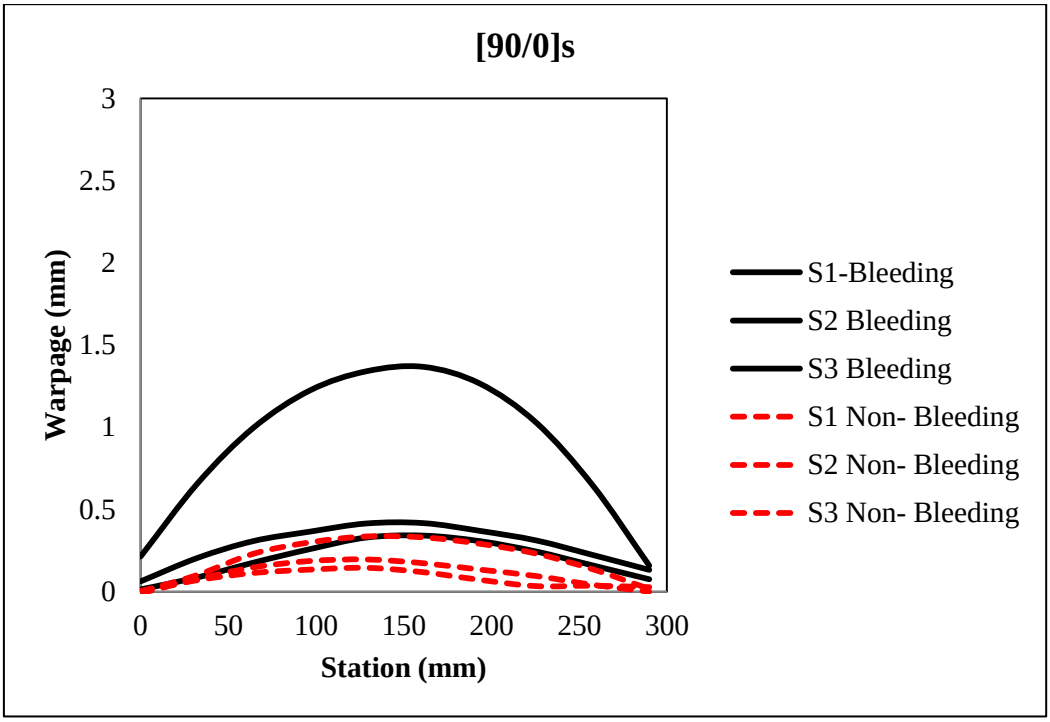


Figure 5.12. Measured warpage in the fabricated strips of XP4 plies.

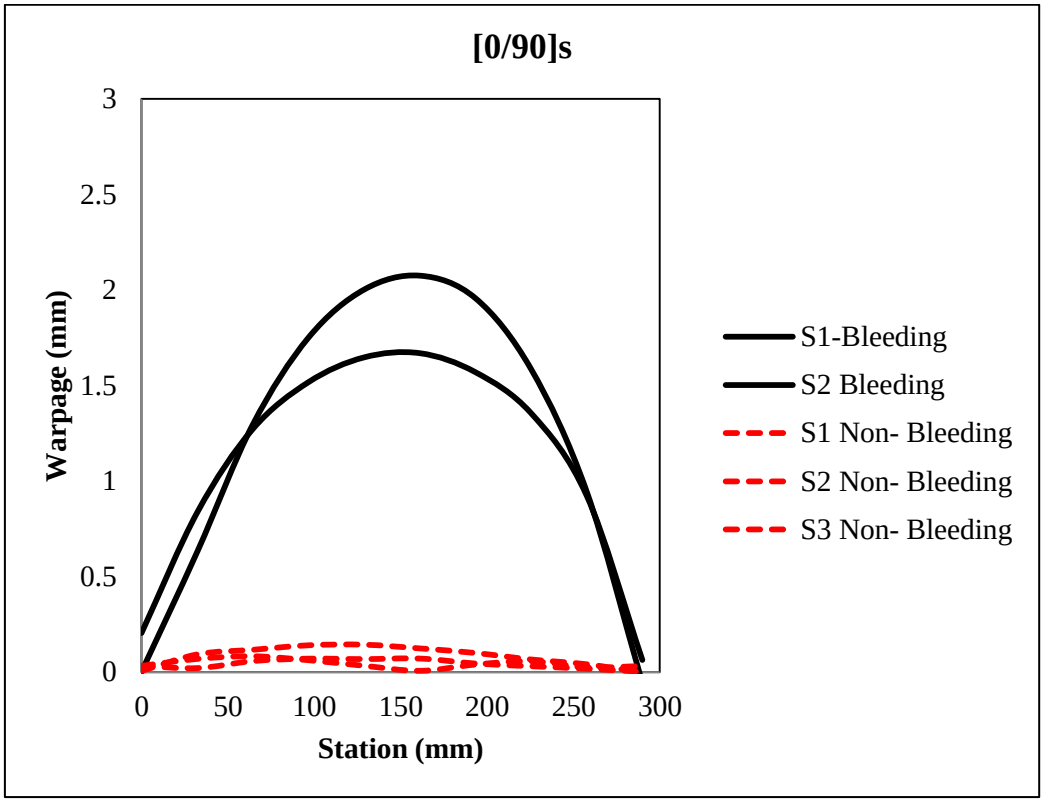


Figure 5.13. Measured warpage in the fabricated strips of XP4 plies.

For the L-shaped laminates were also manufactured under bleeding and non-bleeding conditions. The comparison between these two conditions for unidirectional and cross-plies was made in Figure 5.14-5.17. It was observed that spring-in values are higher in the bleeding condition as compared to the non-bleeding condition.

Although the distortion mechanism for the curved parts resembles the one that occur in flat parts, there is another factor, called fibre bridging, that is responsible for the non-uniform FVF through the thickness. The autoclave pressure is ineffective at the corner of the part due to fibre bridging, which causes a low pressure region at the corner which is then percolated by resin so that the thickness of the part at the corner increases and a resin rich layer is formed at the surface, as represented in Figure 1.6. This effect is more pronounced in tighter radius parts.

Thickness of the laminates that were manufactured under bleeding and non-bleeding conditions was measured. The thickness profiles were shown in Figure 5.18-5.19. Thickness is less in the arm close to the vacuum port in bleed condition. There is internal

percolation to the corner in non-bleed condition, which reduces tension on the fibres close to the bag-side surface in the corner region and through-thickness bleeding increases compaction in corner region and increases fibre tension on the fibres close to the bag-side surface in the corner region.

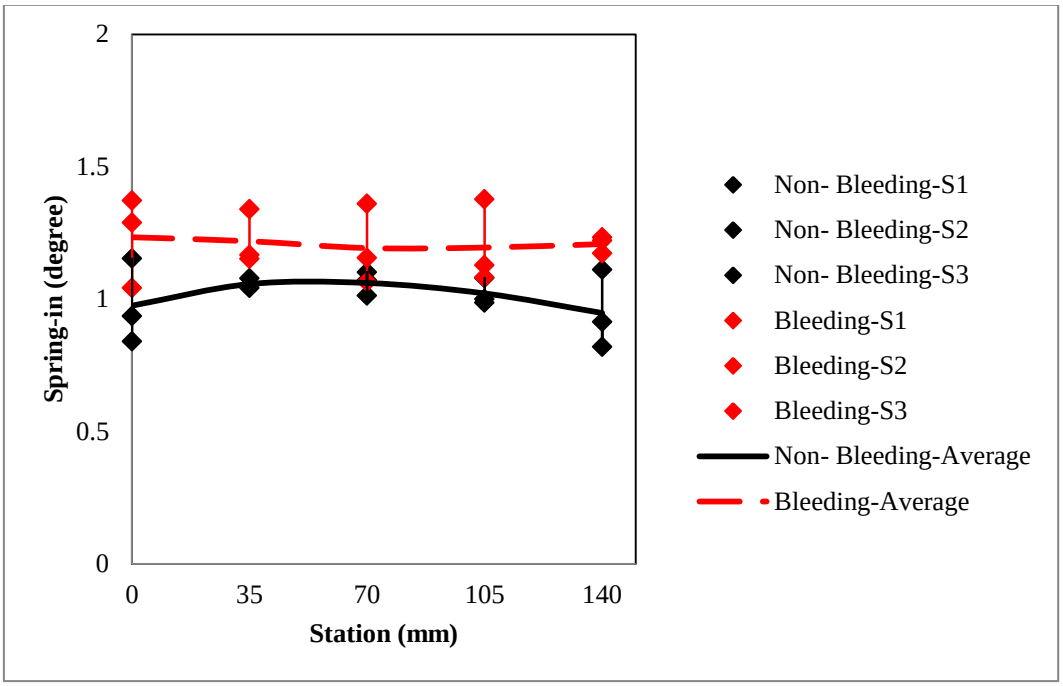


Figure 5.14. Measured deformation patterns in the fabricated UD4-R15.

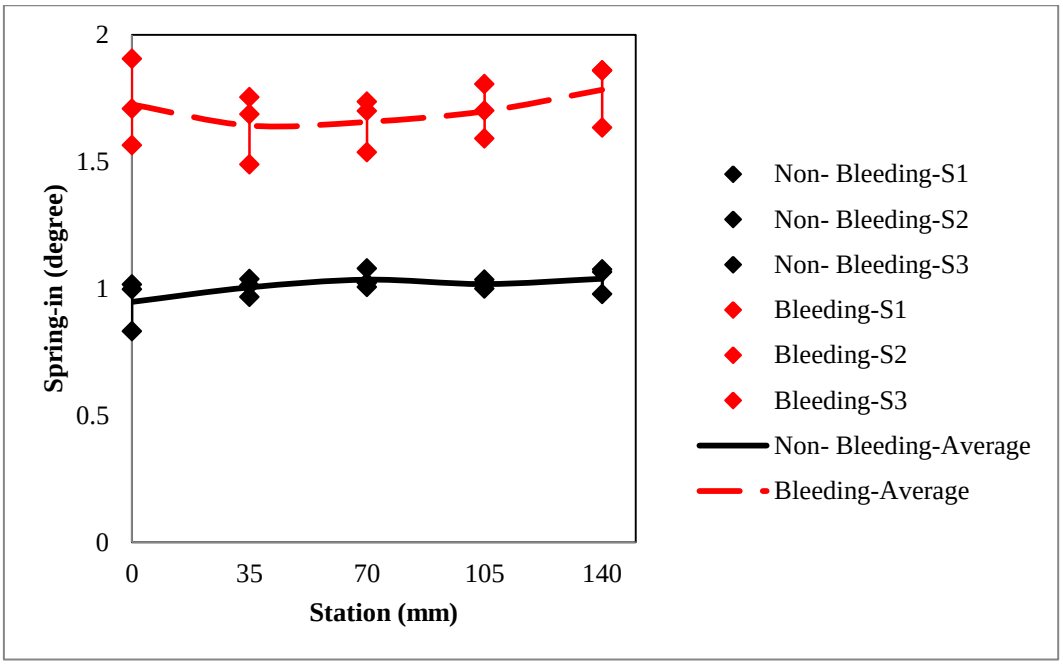


Figure 5.15. Measured deformation patterns in the fabricated UD4-R25.

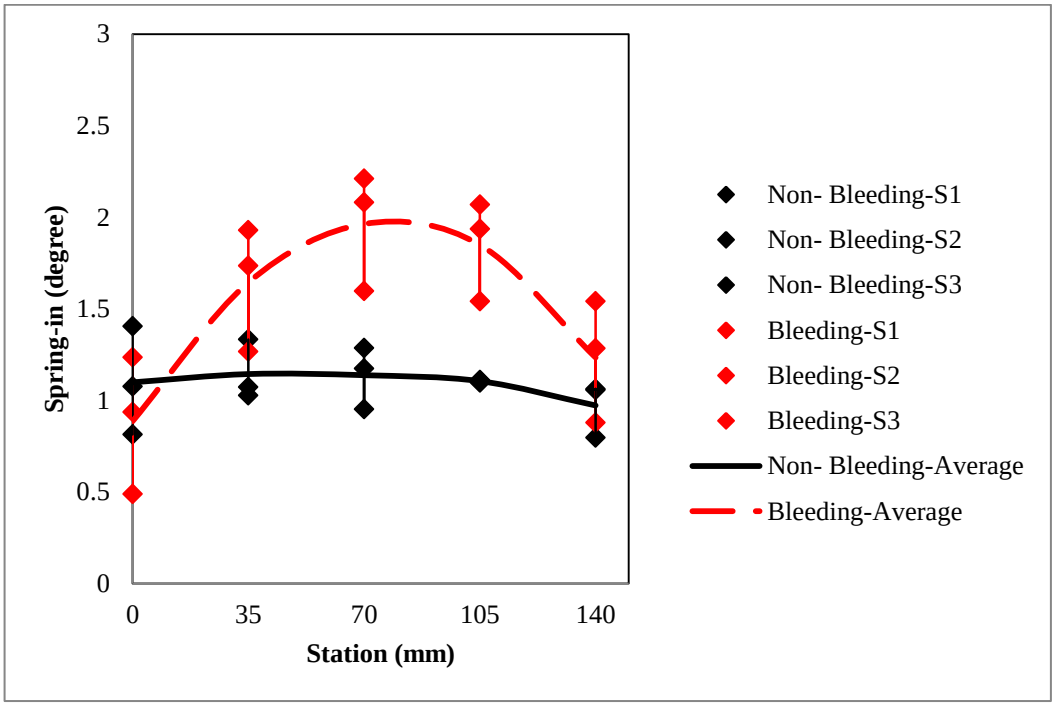


Figure 5.16. Measured deformation patterns in the fabricated XP4-R15.

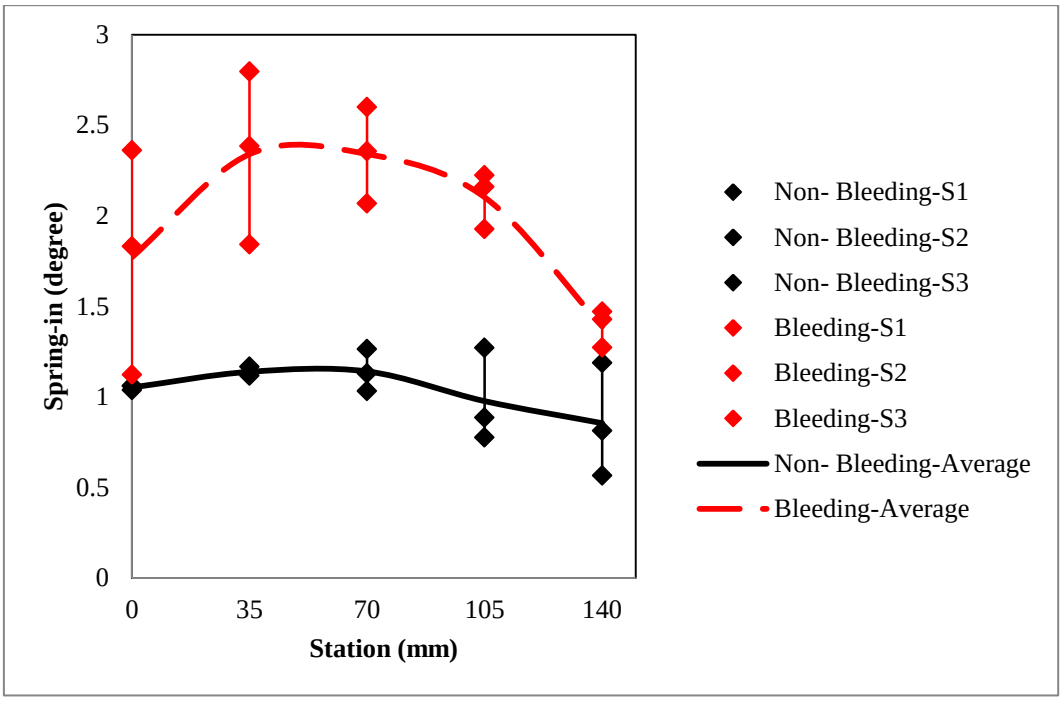
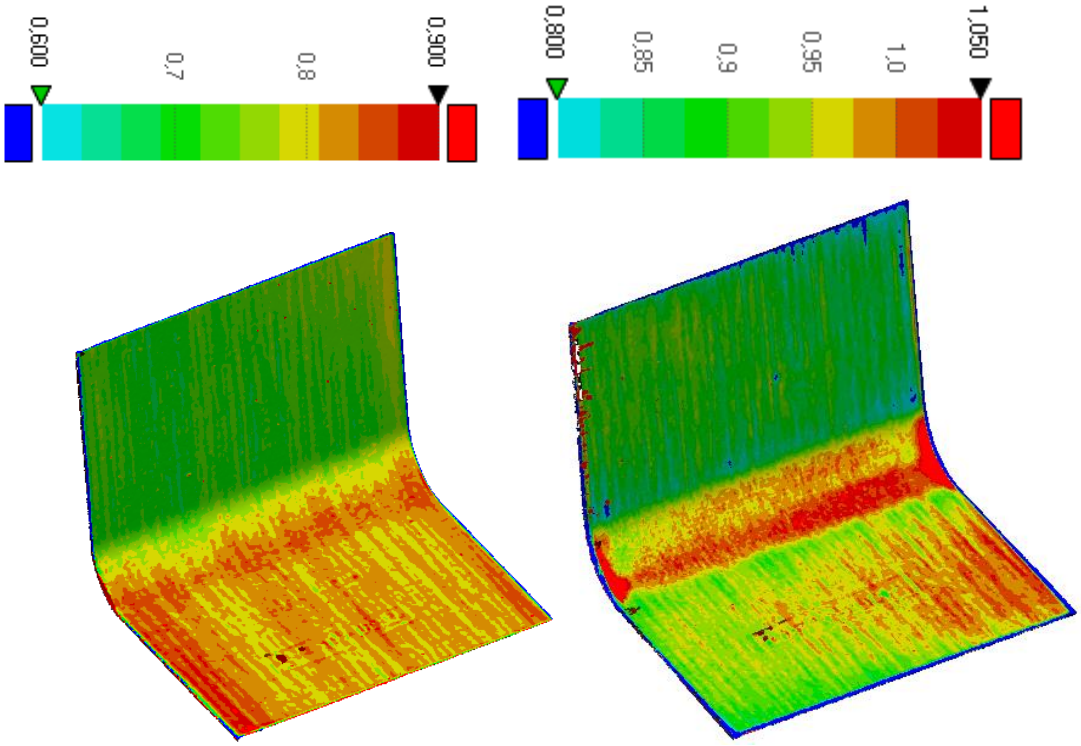
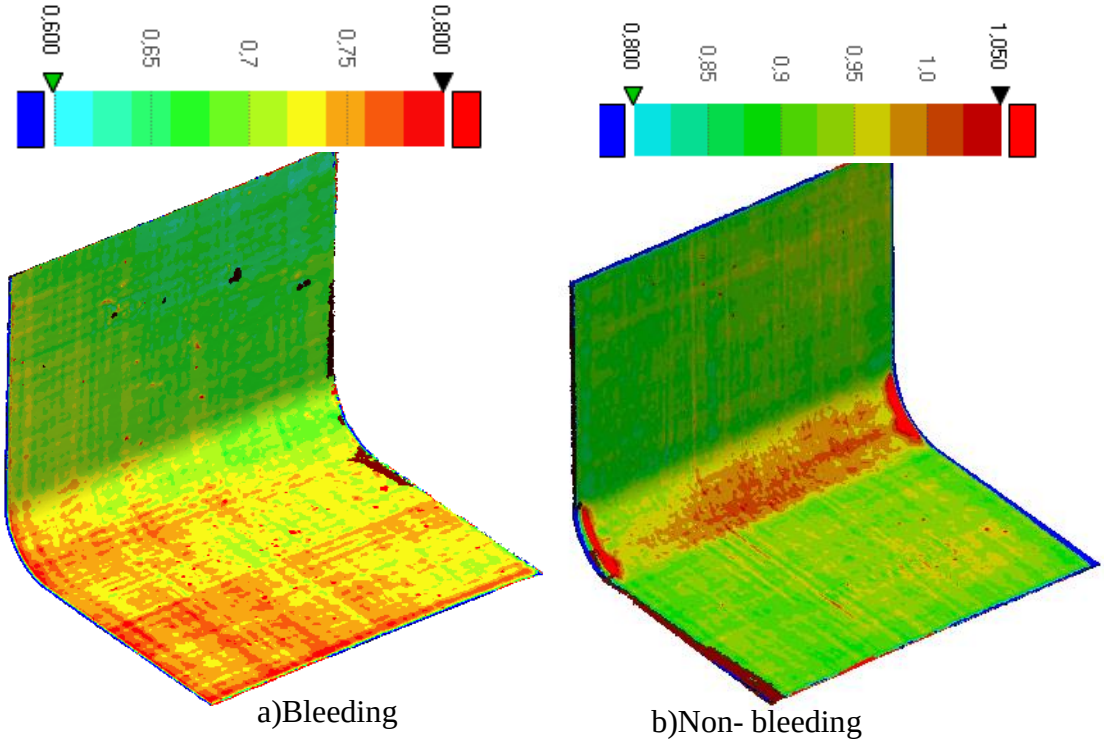


Figure 5.17. Measured deformation patterns in the fabricated XP4-R25.



a)Bleeding b)Non- bleeding

Figure 5.18. Thickness variation for UD4-R25 laminate.



a)Bleeding b)Non- bleeding

Figure 5.19. Thickness variation for XP4-R25 laminate.

5.1.4. Effect of Stacking Sequence on the Warpage

The magnitude of warpage in unidirectional and cross-ply laminates was compared by changing the stacking sequence of the samples. It was observed that stacking sequence has a pronounced effect on distortion basically because of the effect of bending stiffness on warpage. The strips are has dimensions of 300 mm x 50 mm, as shown in Figure 5.20. The stacking sequence of the UD samples are $[90]_4$ and XP samples are $[90/0]_s$ and $[0/90]_s$.

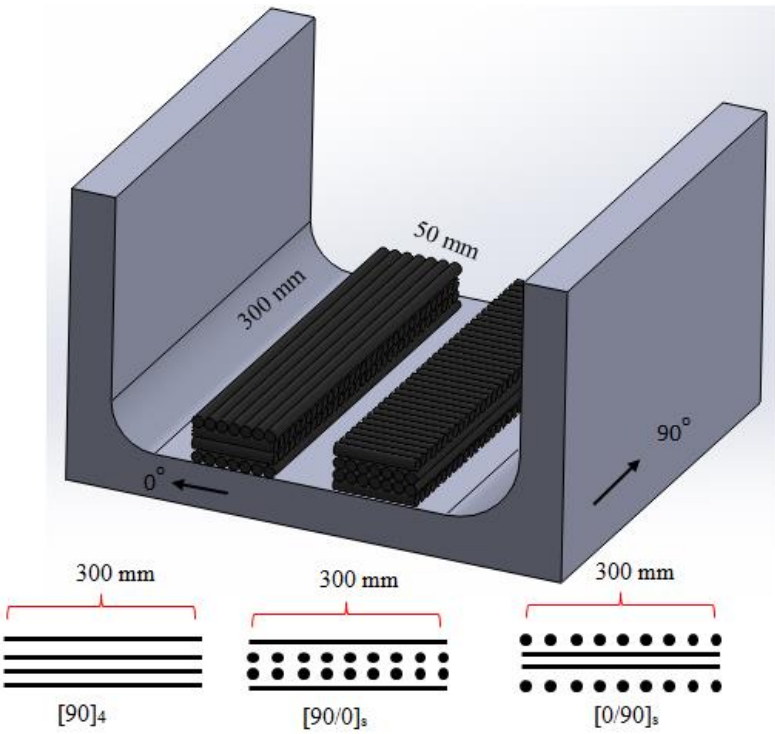


Figure 5.20. Schematic representation of strip placement and stacking configuration.

It was observed that unidirectional $[90]_4$ strip gives more warpage than cross-ply strips of $[0/90]_s$ and $[90/0]_s$ lay-up although both samples were subjected to the same tooling constraints. The reason behind this observation is as follows: tool-part interaction effect is more pronounced for the $[90]_4$ samples due to stretching of fibres in 90 degree ply close to the tool. This generates more residual stress inside the laminate as compared to the other configurations. The warpage values are represented in Figure 5.21.

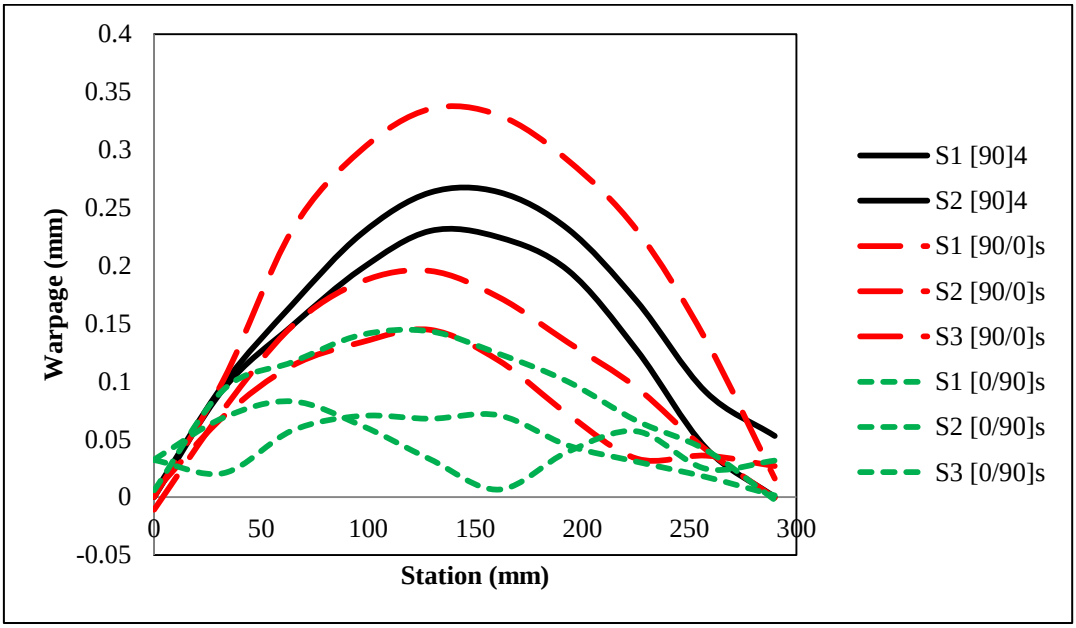


Figure 5.21. Warpage values for different stacking sequence.

The effect of stacking sequence on distortion can be seen in L-shaped laminates by examining the warpage of the arms of the samples along different sections such as Section-1 and Section-2, as represented in Figure 5.22.

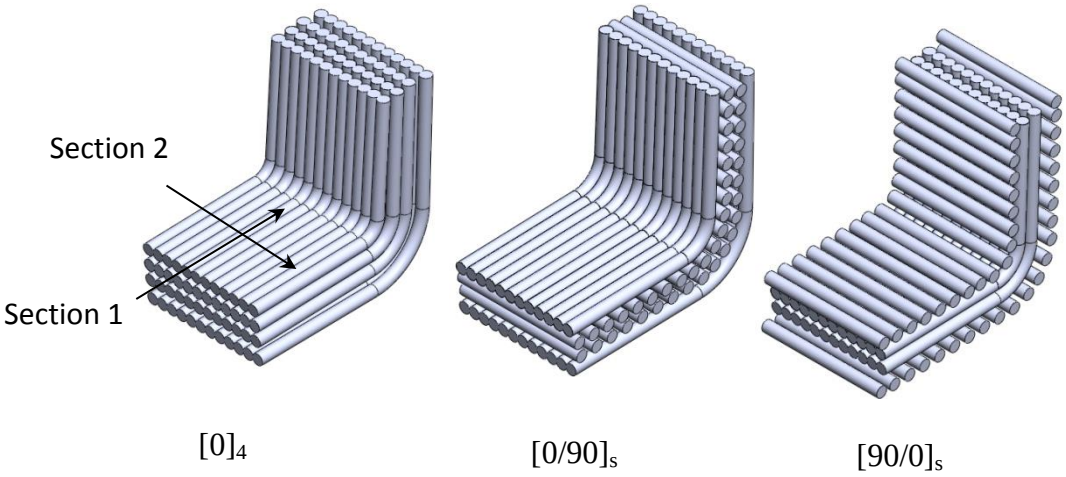


Figure 5.22. Warpage values are measured in Section-1 and Section-2.

These measured data were taken from the laminates that were manufactured under bleeding condition where warpage values were higher. Comparison of warpage values between Section-1 and Section-2 shows that warpage values along Section-2 is higher than

Section-1 for $[0]_4$ samples, as shown in Figure 5.23. The bending stiffness at this section is higher than Section-2. Section-1 is the fibre dominated section.

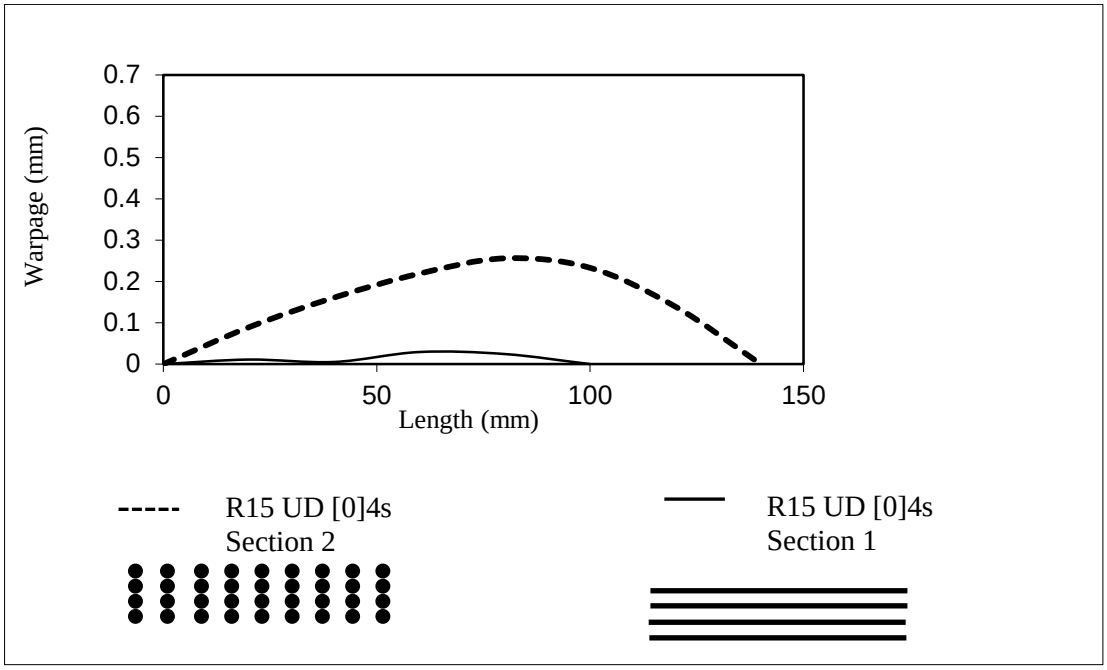


Figure 5.23. Warpage values measured in section 1 and section 2 for UD-R15 $[0]_4$.

Same comparison was made for cross-ply parts of different stacking sequences. For the cross-ply laminates of $[0/90]_s$ stacking sequence, Section-2 gave more warpage values as compared to Section-1. As opposed to this stacking configuration, it was observed that Section-1 gives more warpage for the stacking sequence of $[90/0]_s$. These observations are represented in Figures 5.24 and 5.25.

Effect of stacking sequence on angular distortion such as spring in was also measured for different cross-ply parts. The part that has [90/0]s stacking sequence spring out and gave negative spring-in values. Displacement of the part with respect to the tool values can be seen in Figure 5.26 for [0/90]s laminate and in Figure 5.27 for [90/0]s laminate (negative displacement values represent spring-in).

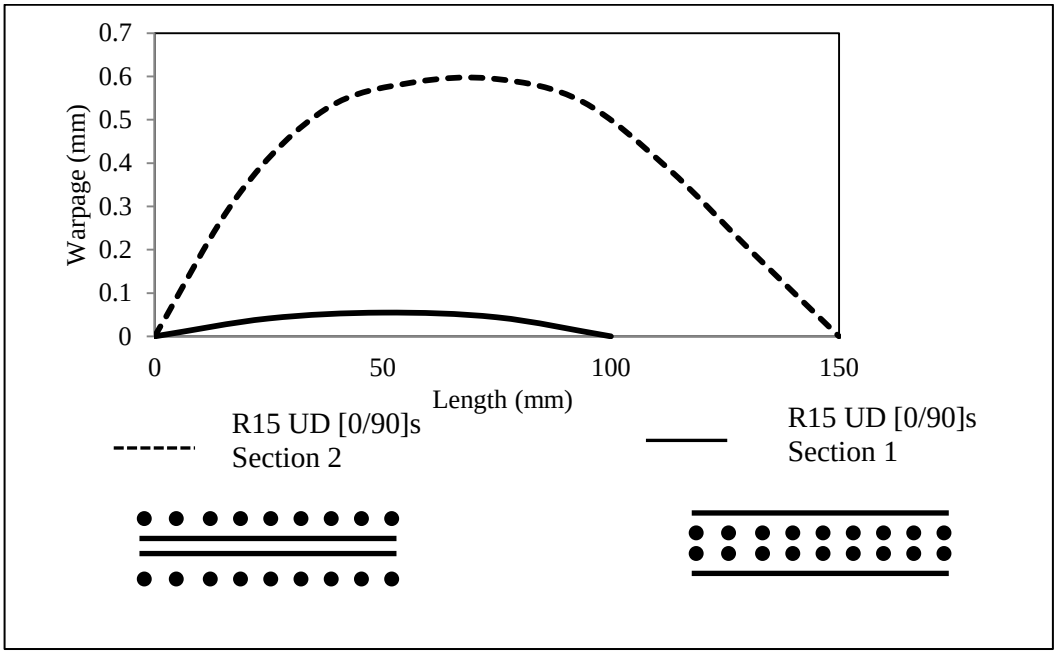


Figure 5.24. Warpage values measured in section 1 and section 2 for XP-R15 [0/90]s.

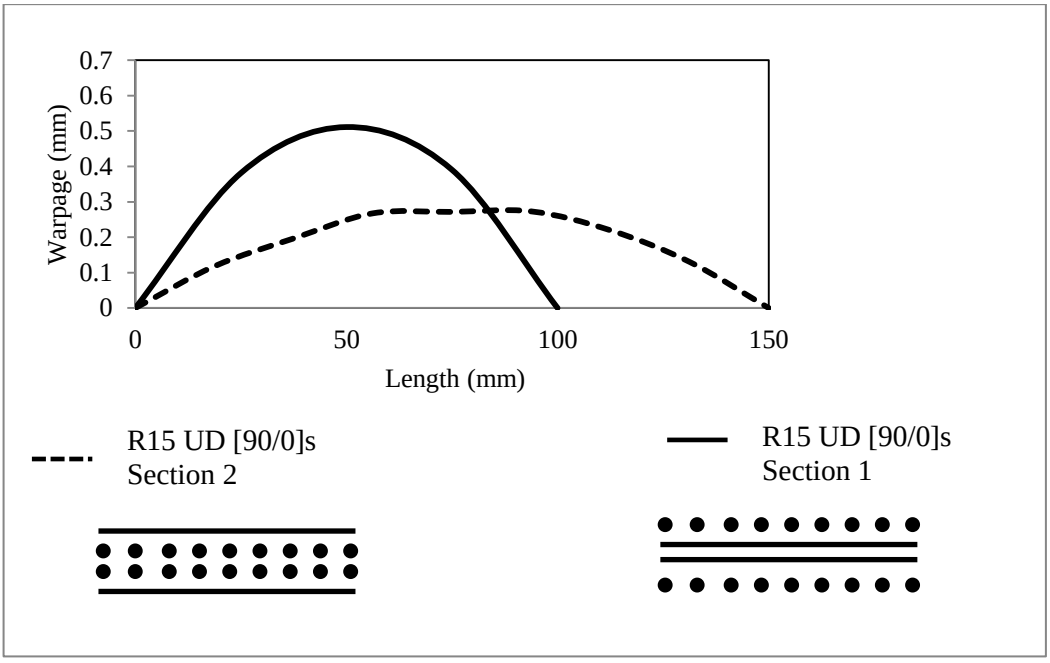


Figure 5.25. Warpage values measured in section 1 and section 2 for XP-R15 [90/0]s.

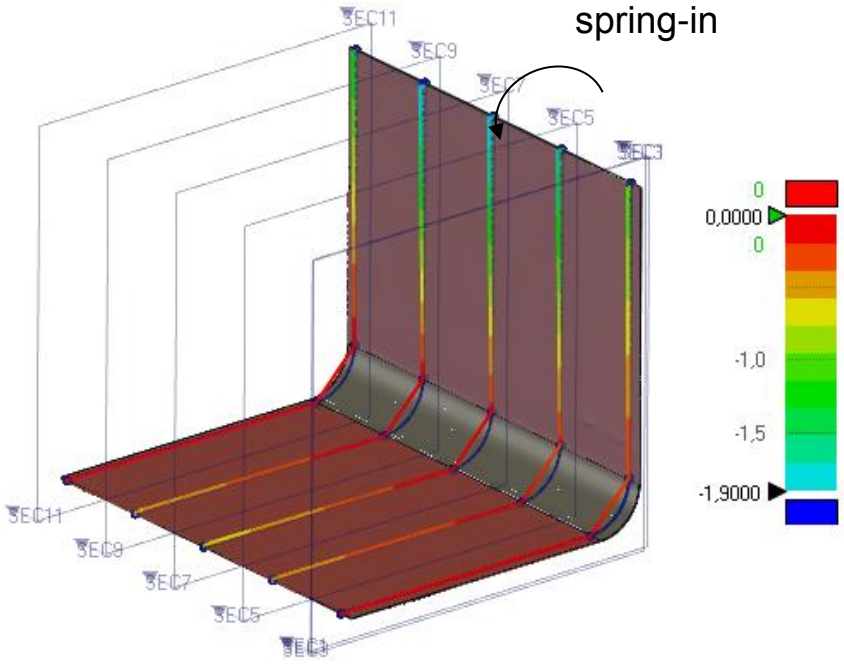


Figure 5.26. Spring-in values for XP-R15[0/90]s laminate. Scale is in mm.

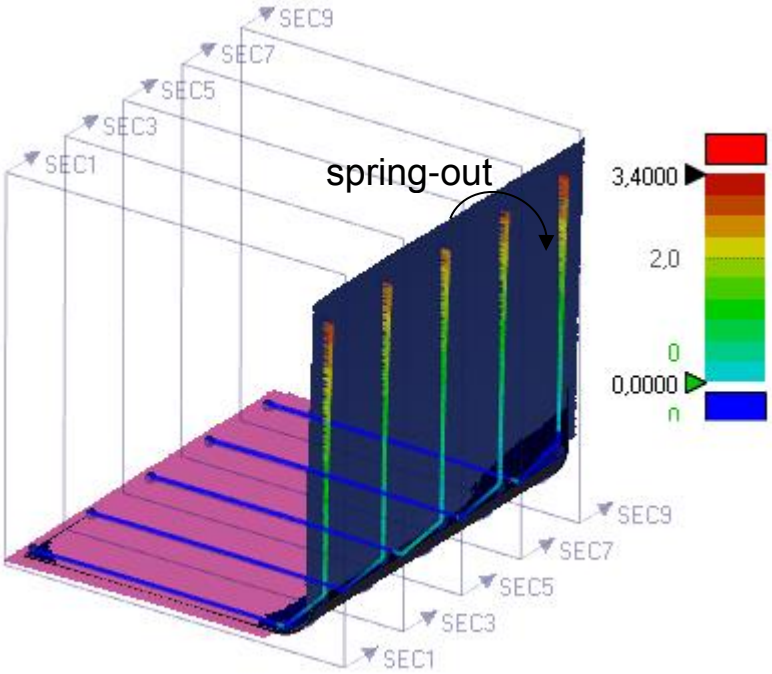


Figure 5.27. Spring-out values for XP-R15 [90/0]s laminate. Scale is in mm.

5.2. 2D Comparison between Predicted and Manufactured Samples

A three-step 2-D finite element model including anisotropy in the thermal expansion coefficient, cure shrinkage, consolidation, and tool-part interaction was developed to predict the process induced stresses and deformation. The three-step Finite Element model has been implemented to predict the spring-in of L-shaped parts. The effect of various material and geometric variables on the deformation of L-Section parts are investigated by a parameter sensitivity analysis. The spring-in predictions obtained by the Finite Element Method are compared to experimental measurements for unidirectional and cross-ply parts of various thicknesses and radii. Results indicate that although a 2D plane strain model can predict the spring-in measured at the symmetry plane fairly well, it is not sufficient to capture the complex deformation patterns observed.

5.2.1. Thermoelastic Spring-in

In order to distinguish the contributions of thermoelastic (thermal contraction), and non-thermoelastic (cure shrinkage, and tool part interaction) factors on spring in, a study was carried out and the results are shown in Figures 5.28-5.31. To show the effect of anisotropic thermal contraction, only the third (cool-down) step is run, with glassy state material properties, and calculated CTEs which alter from the nominal value due to corner thickening. Corner thickening results in a higher resin fraction, and higher through-the thickness CTEs. The effect of thermal contraction on spring-in does not change significantly by corner thickening, as shown by the approximately constant values of thermoelastic contraction for the different thickness cases with different degrees of corner thickening in Figures 5.28-5.31. Highest corner thickening takes place in the thickest unidirectional specimen with the smallest radius, namely UD16-R15 (Figure5.3), and this increases the thermoelastic contribution from 0.37 to 0.43 degrees.

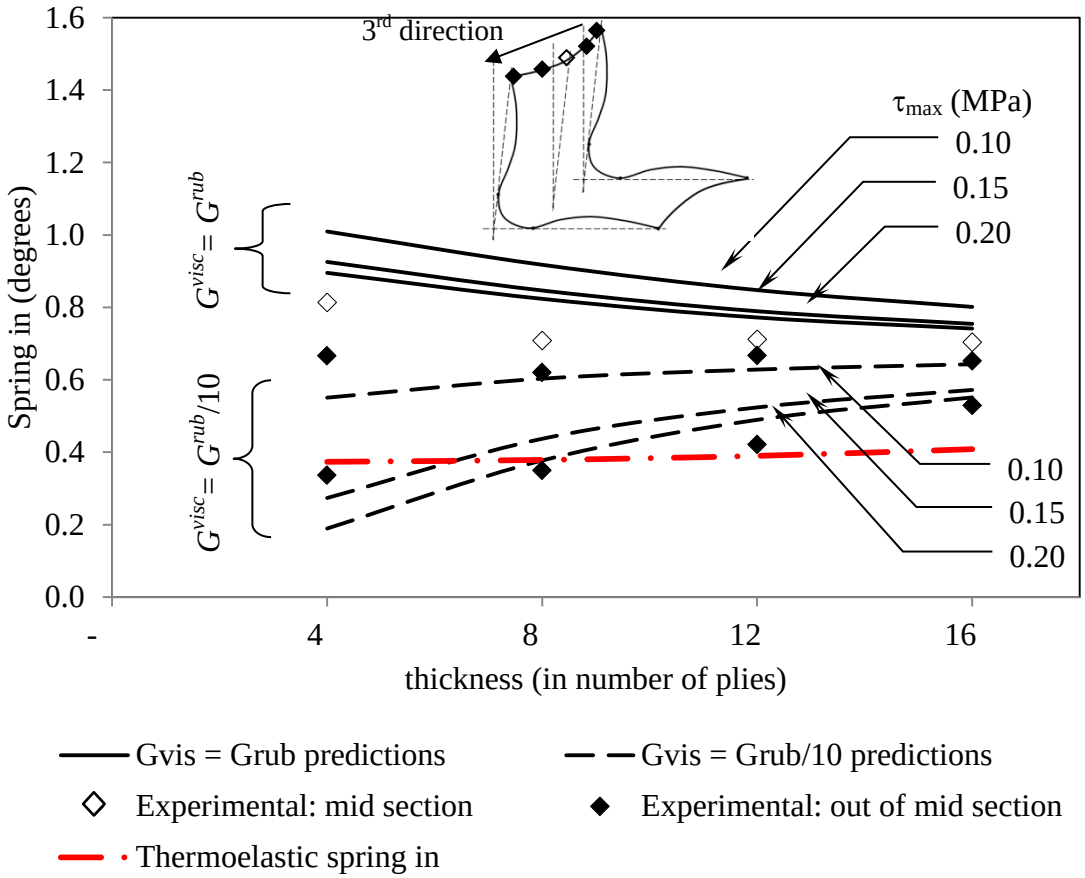


Figure 5.28. Effect of sliding shear stress and viscous shear modulus on spring-in predictions for UD-R25 parts.

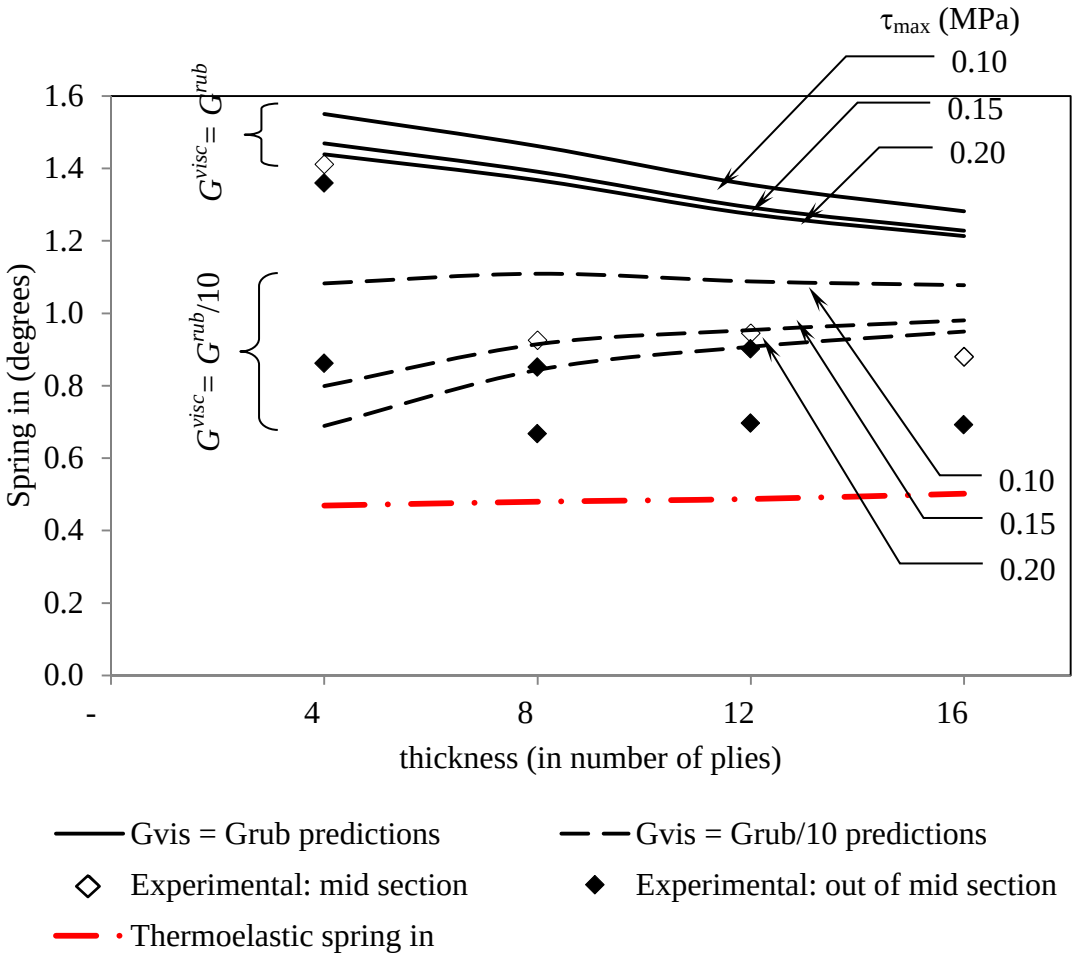


Figure 5.29. Effect of sliding shear stress and viscous shear modulus on spring-in predictions for XP-R25 parts.

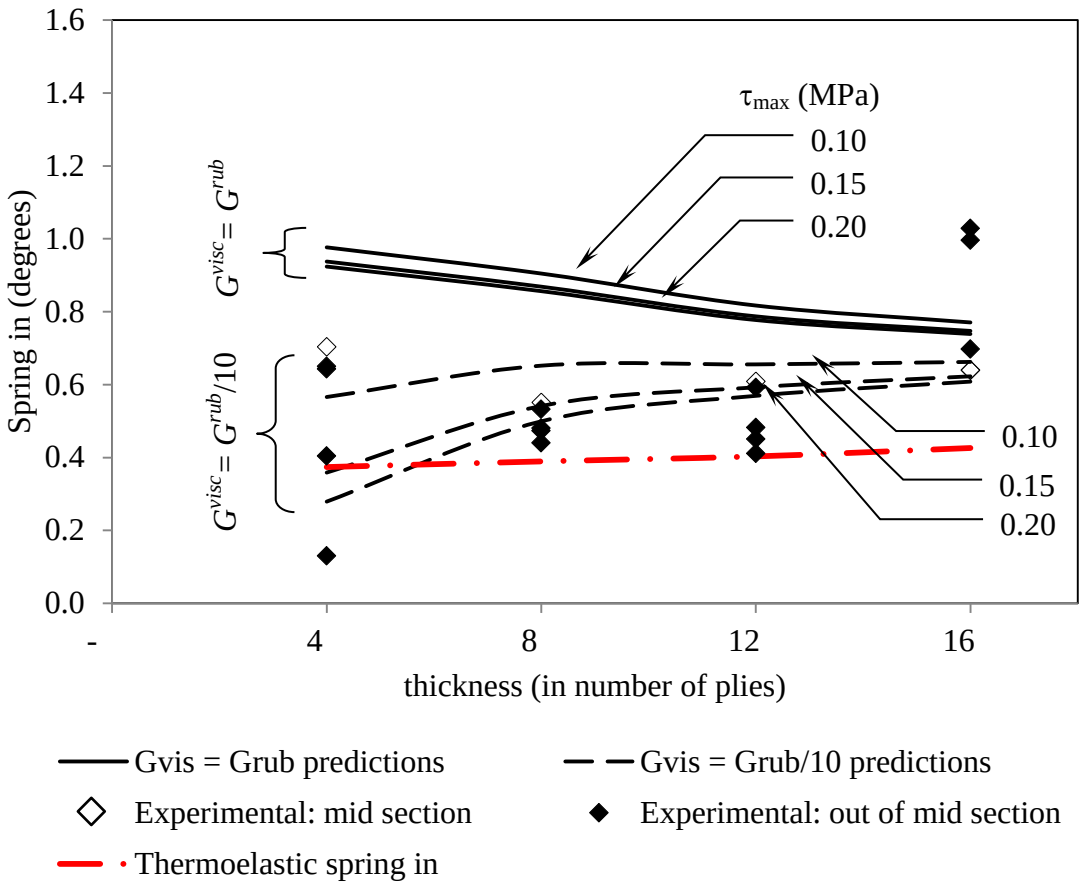


Figure 5.30. Effect of sliding shear stress and viscous shear modulus on spring-in predictions for UD-R15 parts.

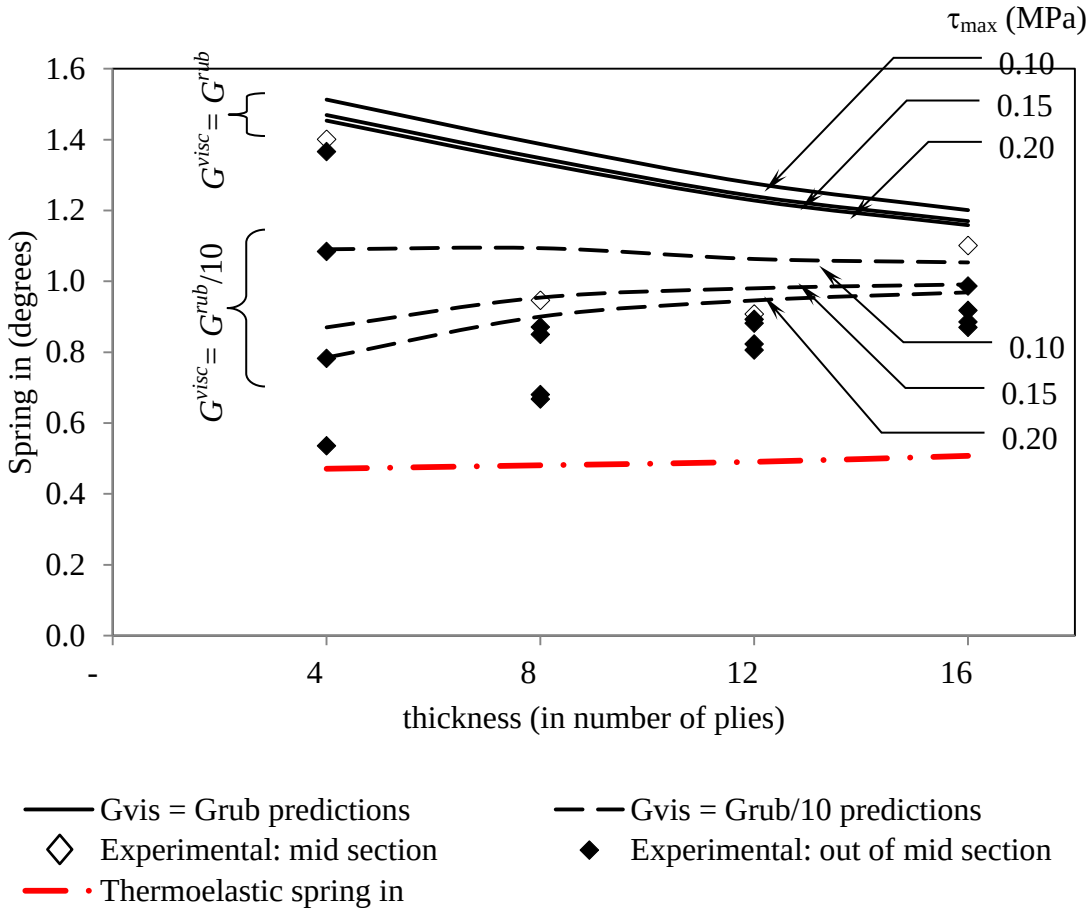


Figure 5.31. Effect of sliding shear stress and viscous shear modulus on spring-in predictions for XP-R15 parts.

5.2.2. Effect of Sliding Stress and Viscous State Shear Modulus.

In the finite element model, the curing of the composite was modelled as step transitions between the viscous, rubbery, and glassy states. The material properties in the rubbery and glassy states were determined with proper experimental or analytical methods [70], however the nature of the material during the viscous state is rather difficult to assess. The resin is in a viscous state, and it is assumed not to carry any stress, however it has been observed that considerable fibre stress may develop in the early stages of cure due to fibre friction within the plies and at the tool-part interface [2, 82]. This observation suggests that the tool-part interaction stress is transferred through the thickness of the material to a certain extent, and the material should exhibit a certain shear modulus. This property is difficult to measure, and a parametric study was carried out in this study to assess the effect of the interface shear stress and shear modulus of the material in the viscous state.

For this reason, the interface sliding shear stress is varied between τ_{max} = 0.10, 0.15, and 0.20MPa. These are typical values for the AS4/8552-Al tool system [2, 82]. The viscous shear modulus of the composite is taken to be either the full rubbery modulus $\left(G_{12}^{rub}, G_{23}^{rub}\right)$ or one-tenth of the rubbery modulus $\left(G_{12}^{rub}/10, G_{23}^{rub}/10\right)$. In Figures 5.28-5.31, predicted spring-in values are plotted together with the experimental values as a function of thickness. Due to the warpage in the 3rd direction (perpendicular to the plane of the 2-D model) the spring in values are not constant along the length of the specimens. Hence corresponding values at the mid-section (unfilled diamonds), as well as the values at other stations (filled diamonds) are plotted on the same graph. It can be seen that the effect of the viscous shear modulus is more dominant than the interface sliding shear stress, and if the viscous shear modulus is high, increasing the interface sliding shear stress has a smaller effect on the predicted spring-in values. It can also be observed that closer predictions are obtained with the lower viscous shear modulus. Another observation can be made regarding the trend of predicted spring-in values with thickness. In order to explain this observation one should keep in mind that spring in is a result of counteracting mechanisms: consolidation and cure shrinkage in the early stages of cure results in tensile stresses on the bag side fibres resulting in spring-in and tool part-interaction on the tool side resulting in spring-out. The observed net effect of these mechanisms depends on their relative magnitudes as well as the thickness of the part, since as the thickness increases; stiffness of the part also increases reducing deformation due to residual stresses. This explains why the spring-in angle reduces with increasing thickness. When the viscous shear modulus is taken to be equal to rubbery shear modulus, $\left(G^{vis} = G^{rub}\right)$, the effect of tool part interaction is minimal due to shear lag along the thickness. However, if the viscous shear modulus is sufficiently low as compared to rubbery shear modulus, $\left(G^{vis} = G^{rub}/10\right)$, the fibre stress gradient due to tool-part interaction is effective, resulting in a lower spring-out in thinner specimens with a lower bending stiffness. Lower viscous shear modulus increases the relative effect of the tool-part interaction in the overall spring-in value, and reverses the trend observed in spring-in with increasing thickness.

It can be seen clearly that thinner specimens have more variation in spring-in values, showing the obvious non constant nature of the spring in along the length of the specimens due to warpage in the 3rd direction (axial, or perpendicular to the model plane). This effect

is expected to be less prominent for thicker specimens, giving less scatter in the spring-in measurements in Figures 5.28-5.31.

This can be explained by the fact that tool-part interaction along the 3rd direction (axial, or perpendicular to the model plane) is less effective than in the 2nd direction for UD parts due to easy deformation of the very compliant resin along the 3rd direction during the viscous and rubbery states, hence warpage due to tool-part interaction along the 3rd direction is low for UD parts. On the other hand for XP parts, fibres along the 3rd direction constrain the composite against expansion of the tool, so that tool-part interaction is more effective along the 3rd direction and causes more warpage as can be seen in Figure 5.32.

In addition to tool-part interaction along the 3rd direction, varying consolidation can be another reason for non-constant spring-in along length direction. A different deformation pattern and more scatter in spring-in values were observed in the UD16-R15 casein Figure 5.30. For this specimen, the spring in value at the mid-section is lower than at the edge sections. This observation can be explained by referring to the thickness measurement along the 3rd direction at the corner (4th station in Figure 5.3). The thickness of the mid-section at the 4th station is higher as compared to the thickness of the edges at the 4th station, as seen in Figure 5.1. The higher consolidation at the edges results in higher fibre stresses at the bag side towards the edges. These residual stresses cause the part to bend inward along the 3rd direction so that spring-in values at the edges will become higher than at the mid-section compared with the other specimens.

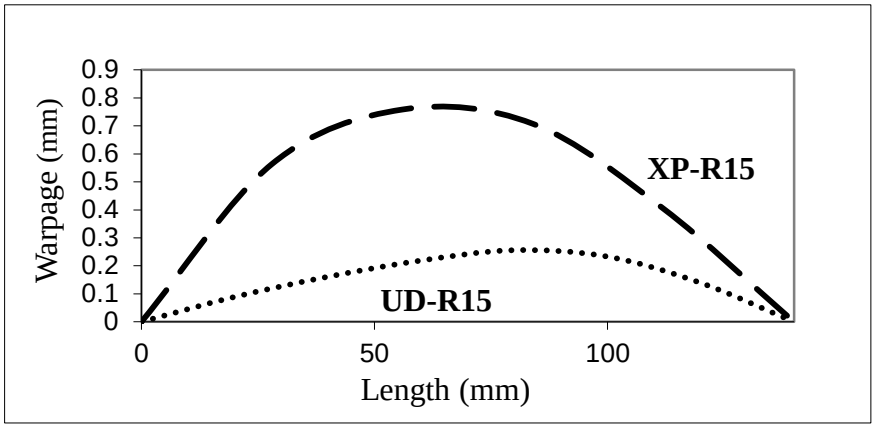


Figure 5.32. Representation of warpage along 3rd direction for 4 ply R15 parts.

5.2.3. Stresses Developed During Curing

Figure 5.33 shows the numerical results for the fibre direction stress distribution through the thickness taken from the FE Model solution for the UD4-R15 part at the end of the second and third step. Here the stresses are calculated according to the local coordinate system shown in Figure 3.3. It can be seen that the fibre direction stress, σ_{22} , increases towards the corner of the part. It has been observed that during the 1st and 2nd Steps tensile stresses are developing at the corner in the bag and tool side. Consolidation and cure shrinkage taking place during the 1st and 2nd Steps causes stretching of the fibres on the bag side. Tool-part interaction causes stretching of the fibres on the tool side. The resulting stress distribution is tensile along the thickness direction, with higher tensile stresses on the tool and bag side. The stresses are rearranged to give a residual stress distribution at the end of third step.

As can be seen from Figure 5.34 which shows the σ_{22} values for the cross-ply samples, which exhibits a zig-zag pattern and a curvilinear distribution superimposed together. The zig-zag distribution is the typical self-balancing residual stress pattern that can be observed in cross-ply laminates during cooling from processing temperature, whereas the curvilinear stress distribution similar to the unidirectional parts is due to the combined effect of consolidation, cure shrinkage, and tool-part interaction.

Another observation is the fact that fibre direction stresses on the bag side at the end of the second step are higher in the cross-ply compared to the unidirectional parts. This is basically due to higher cure shrinkage in XP parts due to the constraints imposed by the fibres in the two planar directions. This observation, in addition to the fact that the cross-ply samples have less bending stiffness explains why the cross-ply parts give more spring-in than the unidirectional ones.

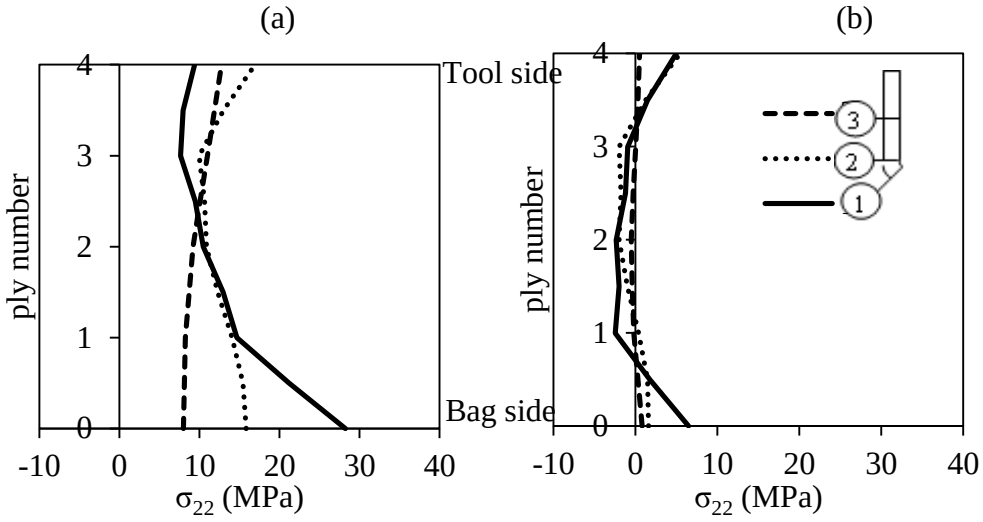


Figure 5.33. Fibre direction stress for UD4-R15 part at the end of (a) 2nd step (b) 3rd step.

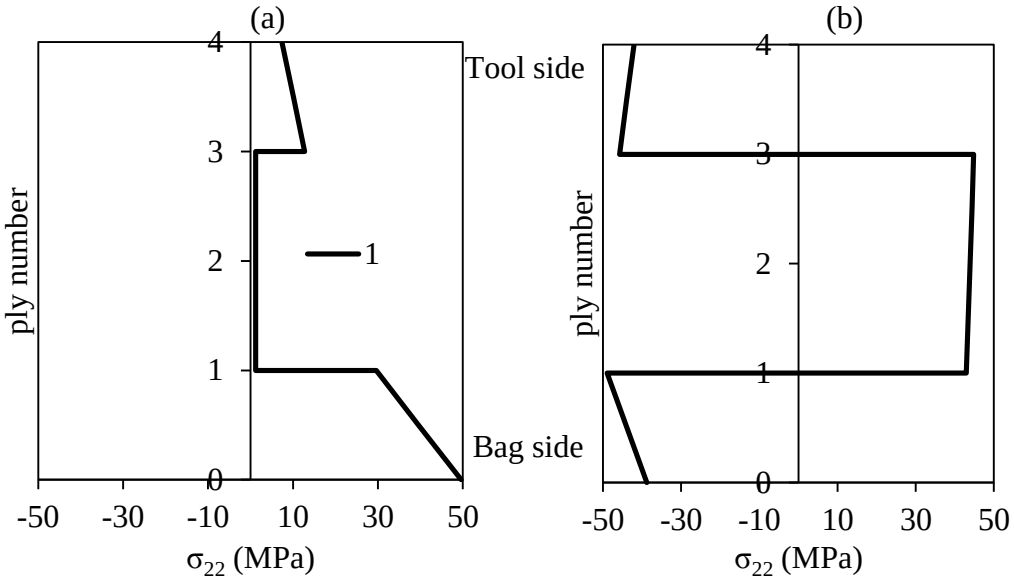


Figure 5.34. Fibre direction stress for XP4-R15 part at the end of (a) 2nd step (b) 3rd step.

5.2.4. Tool-part Interaction

As seen in Figure 5.35, the finite element analysis showed that opening of the contact interface occurs at the corner of the L-shaped parts, which results from cure shrinkage in the second step of the model and fibre bridging of the corner. Experimental results confirm

this opening by corner thickening and the poor surface finish of the corner as seen in Figure 5.36. In Figure 5.37 the autoclave pressure, frictional shear stress, separation from the tool, and relative displacement between the tool and the part are shown at the end of step 2 for the UD16-R25 part. The autoclave pressure is ineffective at the corner of the part due to fibre bridging, which causes the part to disengage from the tool at the corner. The opened region at the corner is percolated by resin so that the thickness of the part at the corner increases and a resin rich layer is formed at the surface. The corner thickness of the parts with 15 mm radius is greater than the parts with 25 mm radius so that cure shrinkage is higher in the former parts. It can also be seen from Figure 5.37 that slipping with constant shear stress prevails for most of the interface on the arms.

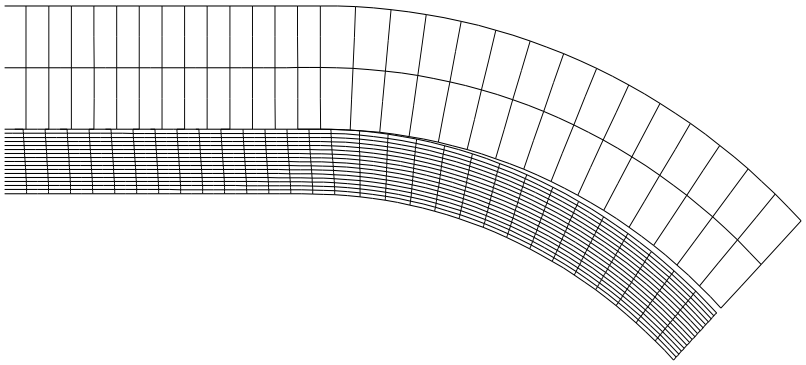


Figure 5.35. Representation of opening at the end of 2nd step for 16UD-R15 part.

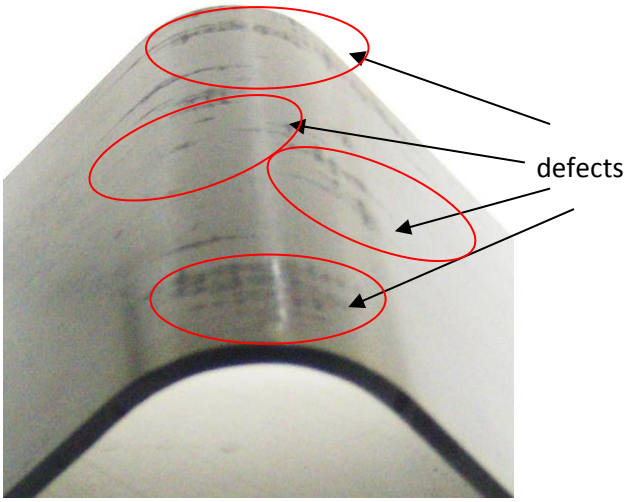


Figure 5.36. Surface defects created by separation of part from the tool during manufacturing.

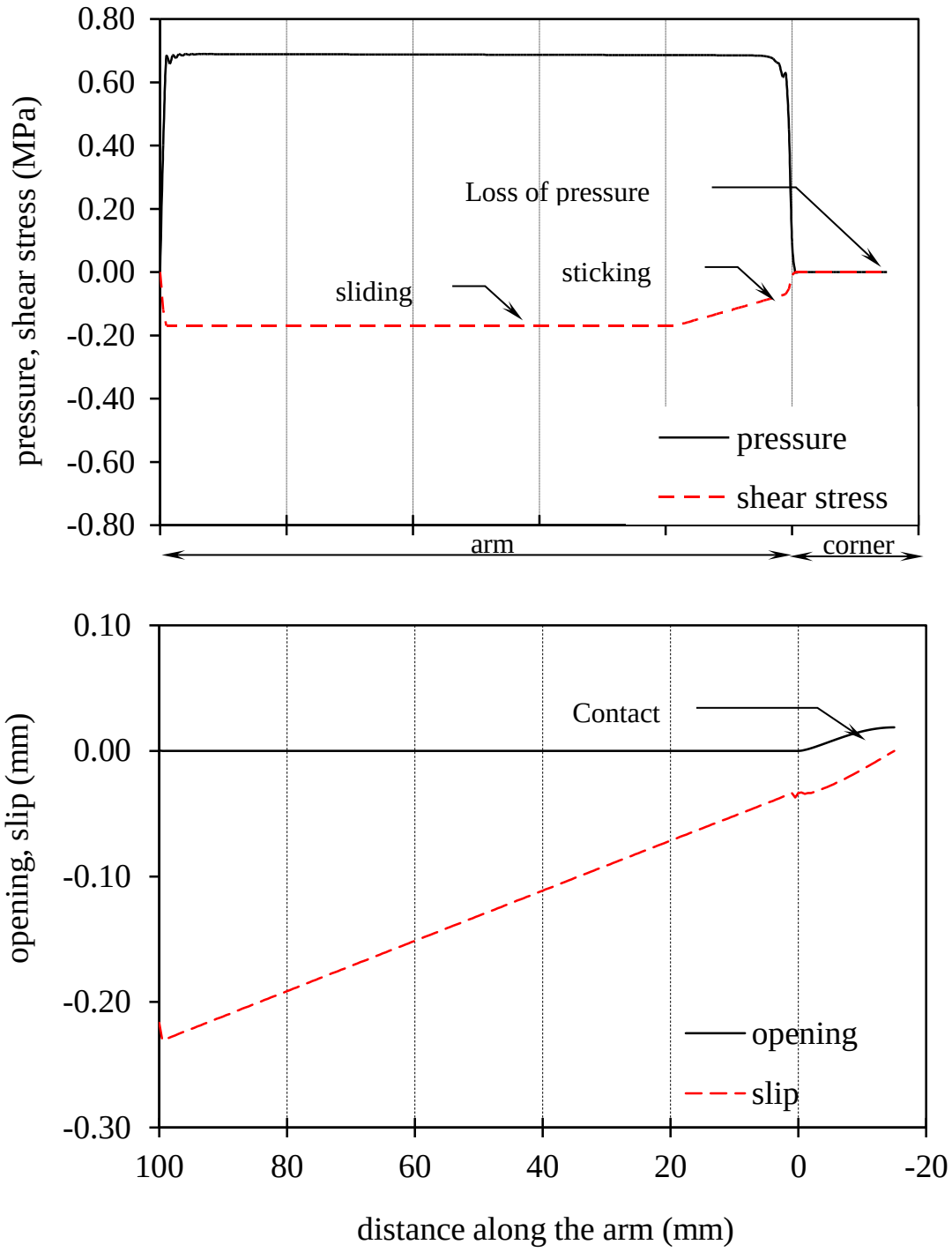


Figure 5.37. Stresses and displacements at the contact interface at the end of the second step for 16UD-R25 part.

5.2.5. Parameter Sensitivity Analysis

Although there are certain values available for the elastic and shear moduli in the rubbery state (E_{22}^{rub}, G_{12}^{rub}) it is not easy to measure or estimate the corresponding pseudo-elastic moduli values in the viscous state (E_{22}^{vis}, G_{12}^{vis}). In order to assess the effects of the various geometric and material parameters on spring-in, a parametric study was conducted using the 2D FEA model. The parameters investigated are: stacking sequence, corner radius, number of plies, transverse and shear moduli in the viscous and rubbery states, E_{22}^{vis} G_{12}^{vis}, E_{22}^{rub}, G_{12}^{rub}, friction coefficient and sliding stress in viscous and rubbery states, μ^{vis} $\tau_{\max}^{vis}$, μ^{rub}, and $\tau_{\max}^{rub}$. Factors and their values are summarized in Table 5.1.

Table 5.1. Factor values used in parameter study.

Factors	Baseline	Values			
Radius (mm)	15	15	25		
Number of plies	4	4	8	12	16
E_{22}^{vis} (MPa)	80	64	80	96	
G_{13}^{vis} (MPa)	20	16	20	24	
E_{22}^{rub} (MPa)	165	132	165	198	
G_{12}^{rub} (MPa)	44.3	35.4	44.3	53.1	
$\tau_{\max}^{vis}$ (MPa)	0.10	0.08	0.10	0.12	
$\mu_{\max}^{vis}$	0.30	0.24	0.30	0.36	
$\tau_{\max}^{rub}$ (MPa)	0.20	0.16	0.20	0.24	
$\mu_{\max}^{rub}$	0.30	0.24	0.30	0.36	

In total, 32 parameter study runs were solved by FEA. Main effects of the DOE factors on spring-in are shown in Figure 5.38. A main effect for a factor is based on the differences in sample averages for all of the runs at each values of the factor. Each factor has its main effects calculated independently of all other factor.

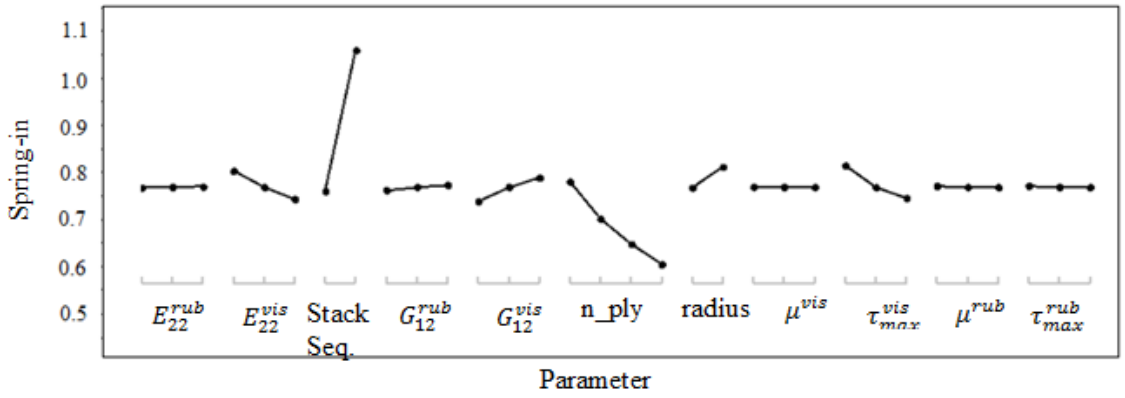


Figure 5.38. Main effects of the DOE factors on the results of spring-in. Refer to Table 5.1 for values of the parameters.

The percent effects of geometric and material parameters for spring-in are shown in Figures 5.39 and 5.40 respectively. The percent effects of each factor were found through the spring-in values of main effects represented in Figure 5.38. It is seen that the stacking sequence, number of plies, $\tau_{\max}^{vis}$, E_{22}^{vis}, and G_{12}^{vis} are the most important parameters for the spring-in.

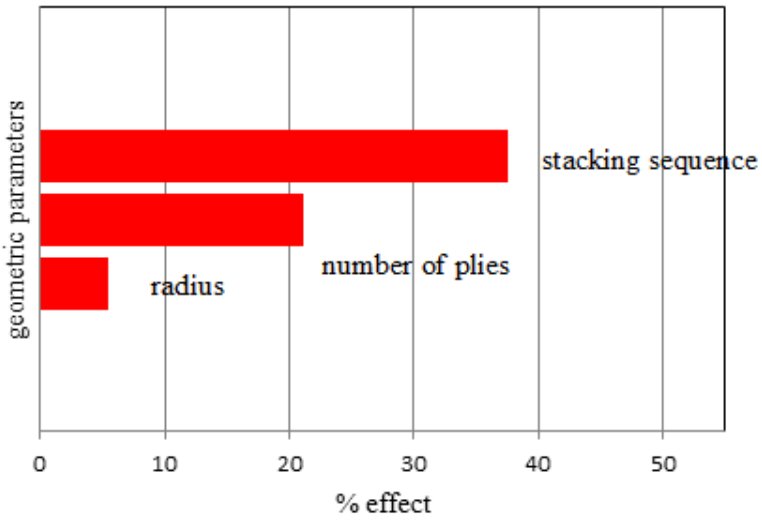


Figure 5.39. Percent effect on spring-in of the geometric parameters.

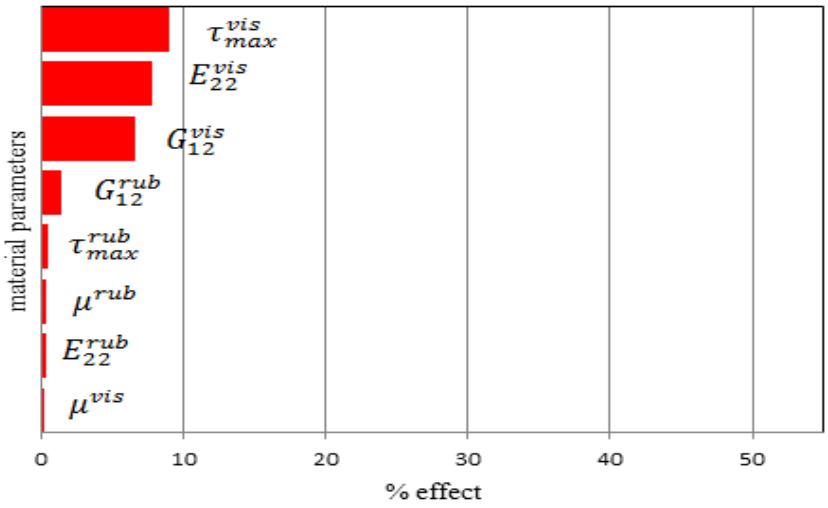


Figure 5.40. Percent effect on spring-in of the material parameters.

5.2.6. Results of 2D Fibre Wrinkling Model

The through-thickness strain distribution at the curve side of the part at the end of each analysis step is represented in Figure 5.41 for parts laid up by alternative method (actually, the FEM developed here has only been carried out for the parts laid up by the alternative method). Compressive strains occurred at the bag side of the part. These compressive strains remain at the bag side of the part at the end of analysis. This argument is supported by the observation of buckled fibres in Figures 5.8.

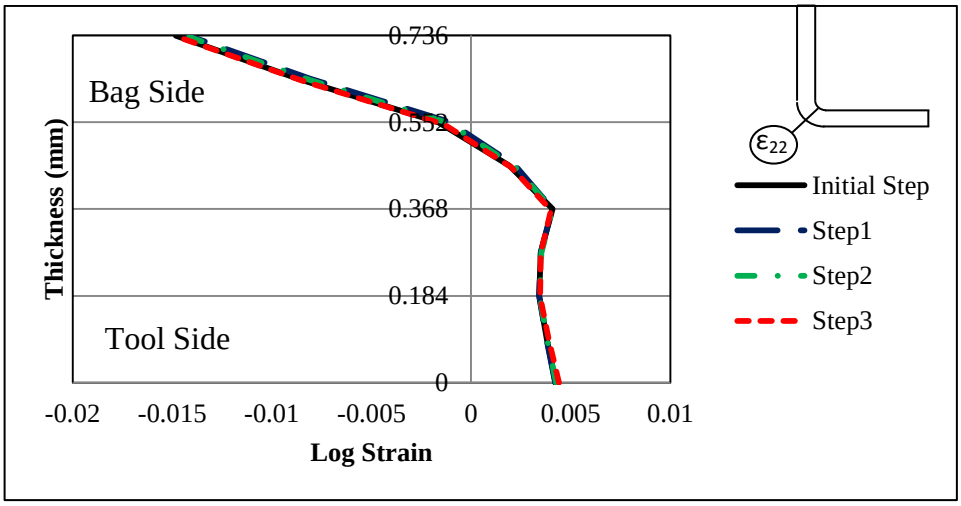


Figure 5.41. Strain distribution through the thickness at the curve side of the part at the end of each steps of analysis.

The through-thickness stress distribution can be seen in Figures 5.42-43 for the current model. Stress values at the bag side of the part after Step 2 were reduced with the reduction of the E11 elastic modulus. The stress distribution for the conventional model, in which there was no initial step simulating ply conformation to the tool, is represented in Figure 5.44.

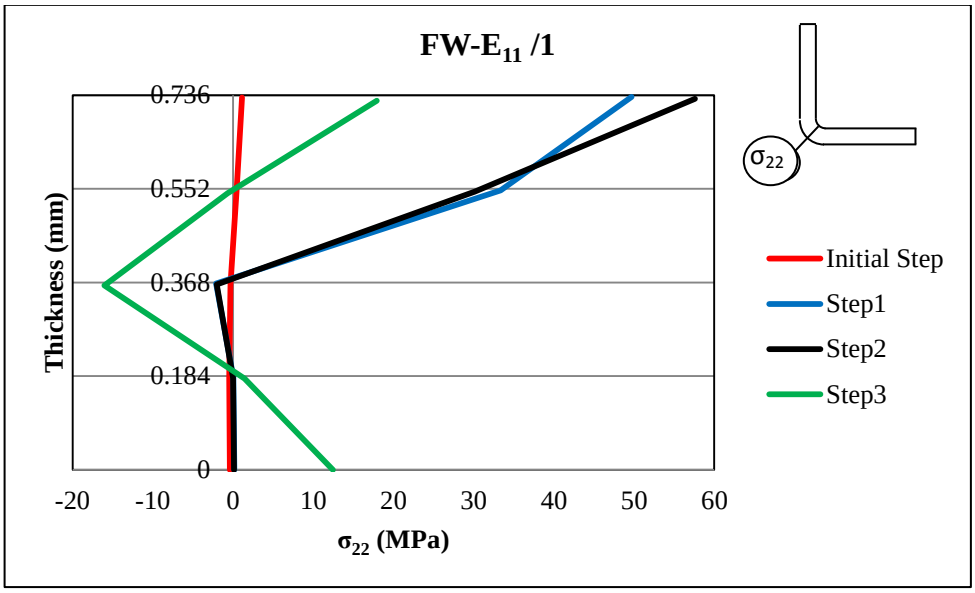


Figure 5.42. Stress distribution through the thickness at the curve side of the part at the end of each steps of analysis in which reduction ratio is 1.

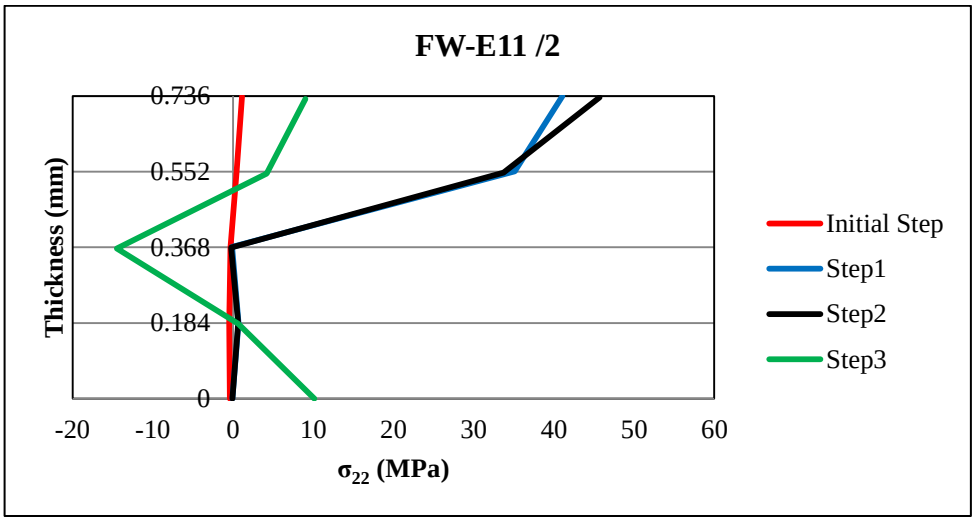


Figure 5.43. Stress distribution through the thickness at the curve side of the part at the end of each steps of analysis in which reduction ratio is 2.

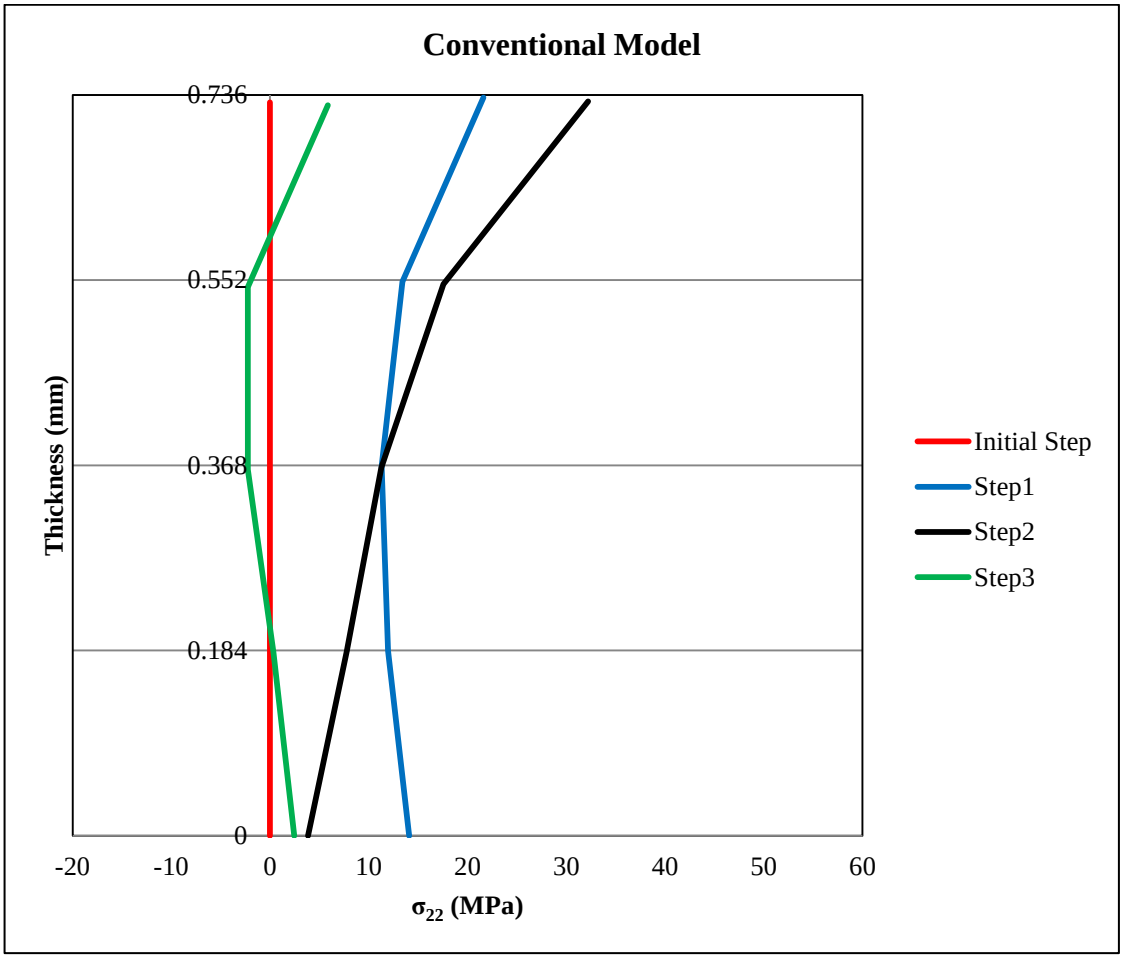


Figure 5.44. Stress distribution through the thickness at the curve side of the part at the end of each steps of analysis for the conventional model.

Both numerically determined and measured values of spring-in at parts produced by the conventional lay-up method are higher than the alternative lay-up method, as is shown in Figures 5.45 and 5.46. In this figure, the designation “C-S1” represents sample 1 (S1) which was manufactured by the conventional lay-up method, and “A-S1” represents sample 1 which was manufactured by the alternative lay-up method. The continuous lines in these figures represent the results of the FEA. The reduction of the elastic modulus resulted in a decrease in the spring-in values.

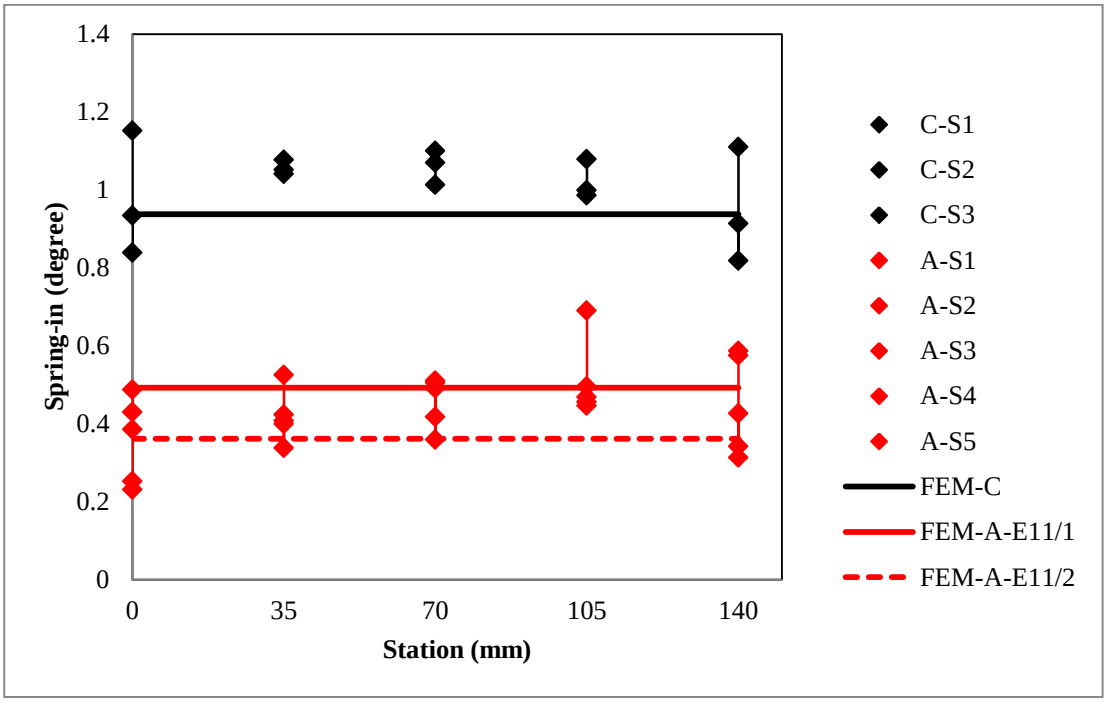


Figure 5.45. Measured and predicted spring-in for $[0]_4$ L-section parts with R15 mm corner radius.

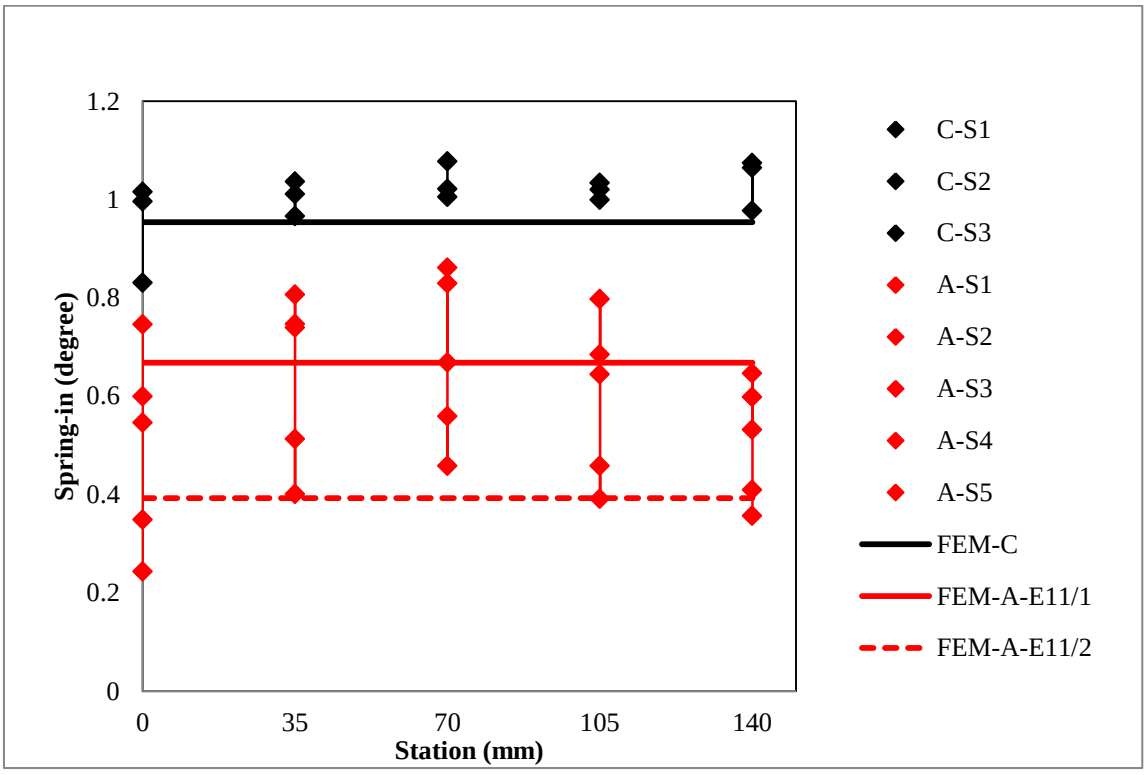


Figure 5.46. Measured and predicted spring-in for $[0]_4$ L-section parts with R25 mm corner radius.

5.3. Comparison of Predicted and Measured 3D Distortion Patterns

A three-step 3-D finite element model including anisotropy in the thermal expansion coefficient, cure shrinkage, consolidation, and tool-part interaction was developed to predict the process induced stresses and deformations. This three-step Finite Element model has been implemented to predict the shape distortion of L-shaped, U-shaped, and flat parts. The effect of viscous shear modulus on the deformation was examined in the 2D FEA so that shear modulus in the viscous state was reduced in this 3D FEA. The reduction ratio was assumed to be one fifth of the rubbery shear modulus. In the following subsections the distortion predictions obtained by the 3D Finite Element Method are compared to experimental measurements for unidirectional and cross-ply parts of various thicknesses, and geometries.

5.3.1. Comparison of Predicted and Measured 3D Distortion Patterns for L-section Samples

In Figure 5.47 full field deformation patterns for UD R15-4 and XP R15-4 plies parts are represented. The spring-in values are plotted against to the number of plies in Figures 5.48- 5.51. The continues and dashed lines in the figures represent the spring in values obtained from FEA and markers represents the measured spring in data at the five equally spaced sections.

The shear modulus reduction in the viscous state decreased the spring-in values and hence the predictions captured the measured spring-in values quite well. 3D FEM model also capture the deformation along the 3rd direction, along which 2D model is incapable to predict. Also, it can be concluded that spring-in values go to asymptotic values as thickness of the laminate increase, as seen Figures 5.48- 5.51.

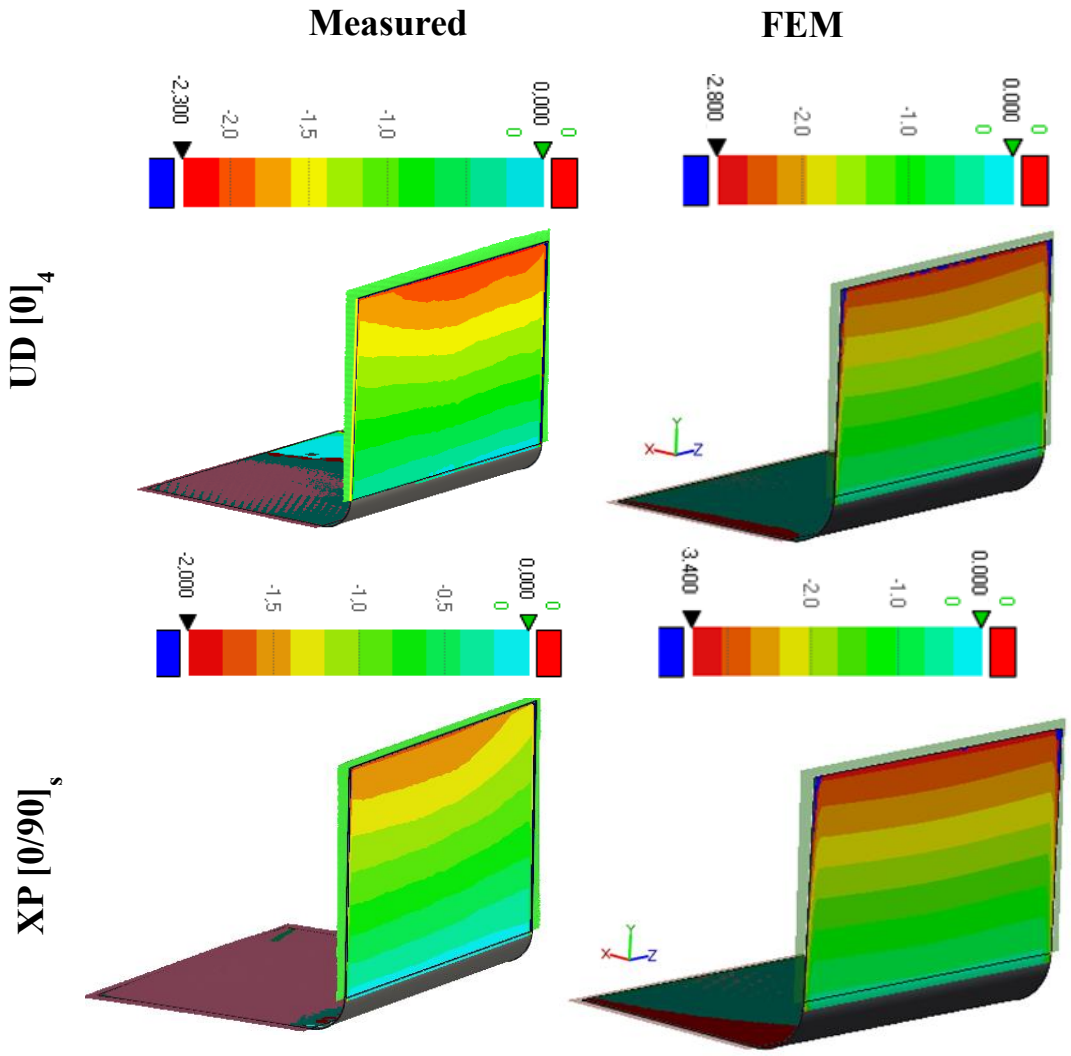


Figure 5.47. Measured and predicted deformation patterns for $[0]_4$ and $[0/90]_s$ L-section parts with R15 mm corner radius.

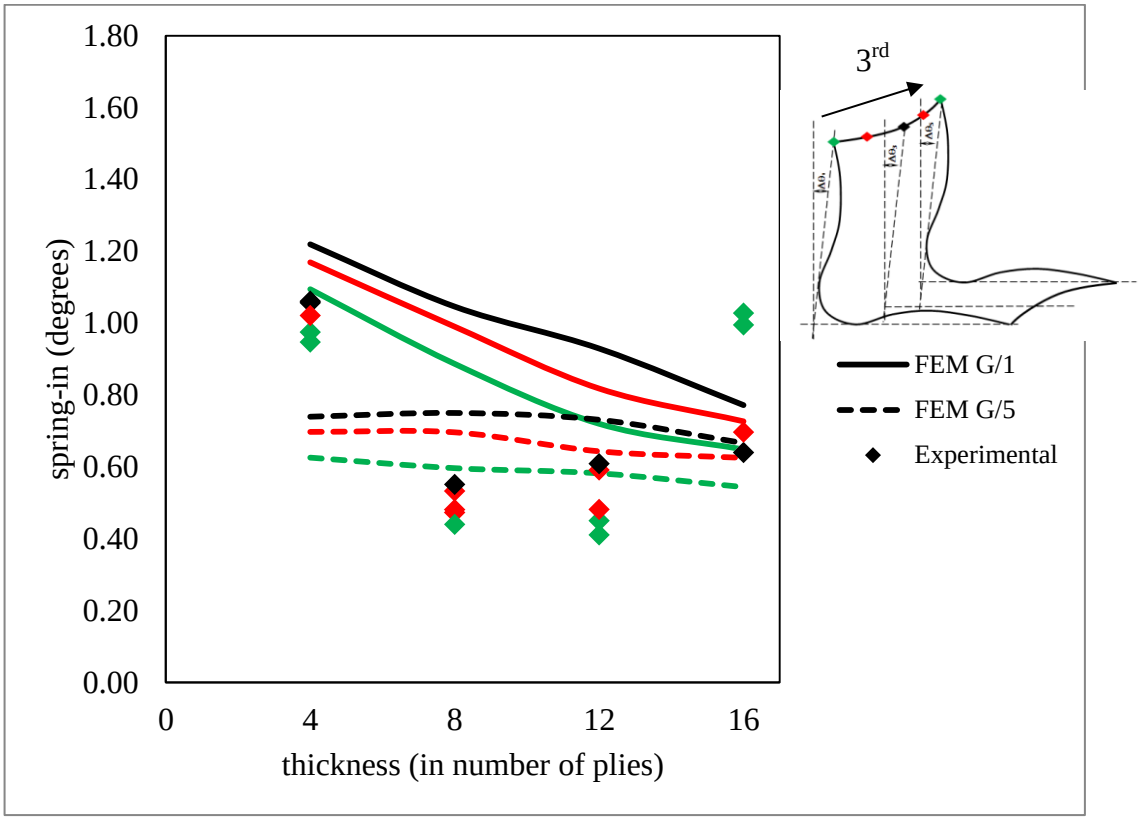


Figure 5.48. Spring-in predictions for UD-R15 parts.

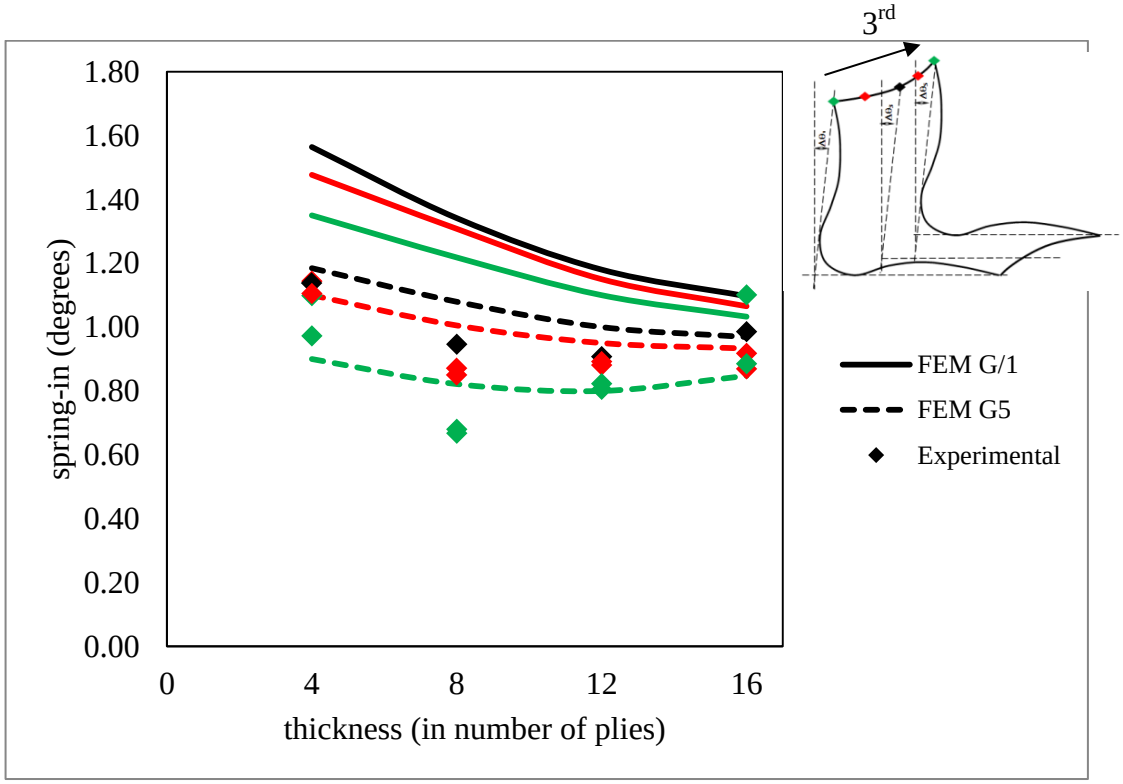


Figure 5.49. Spring-in predictions for XP-R15 parts.

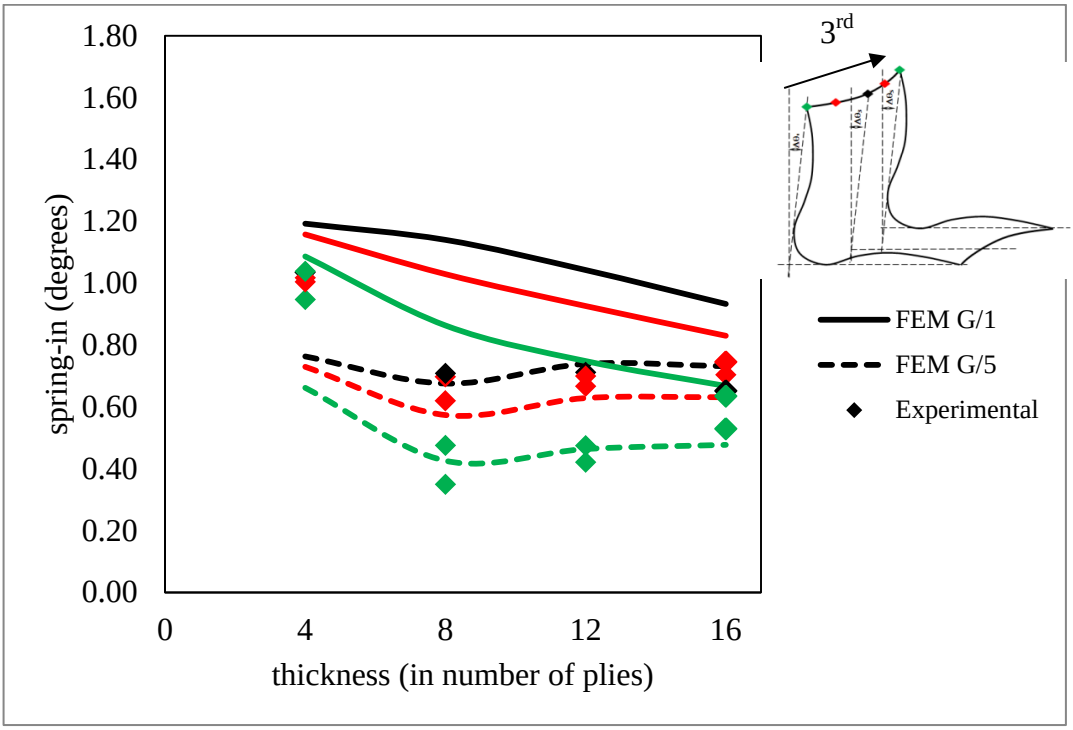


Figure 5.50. Spring-in predictions for UD-R25 parts.

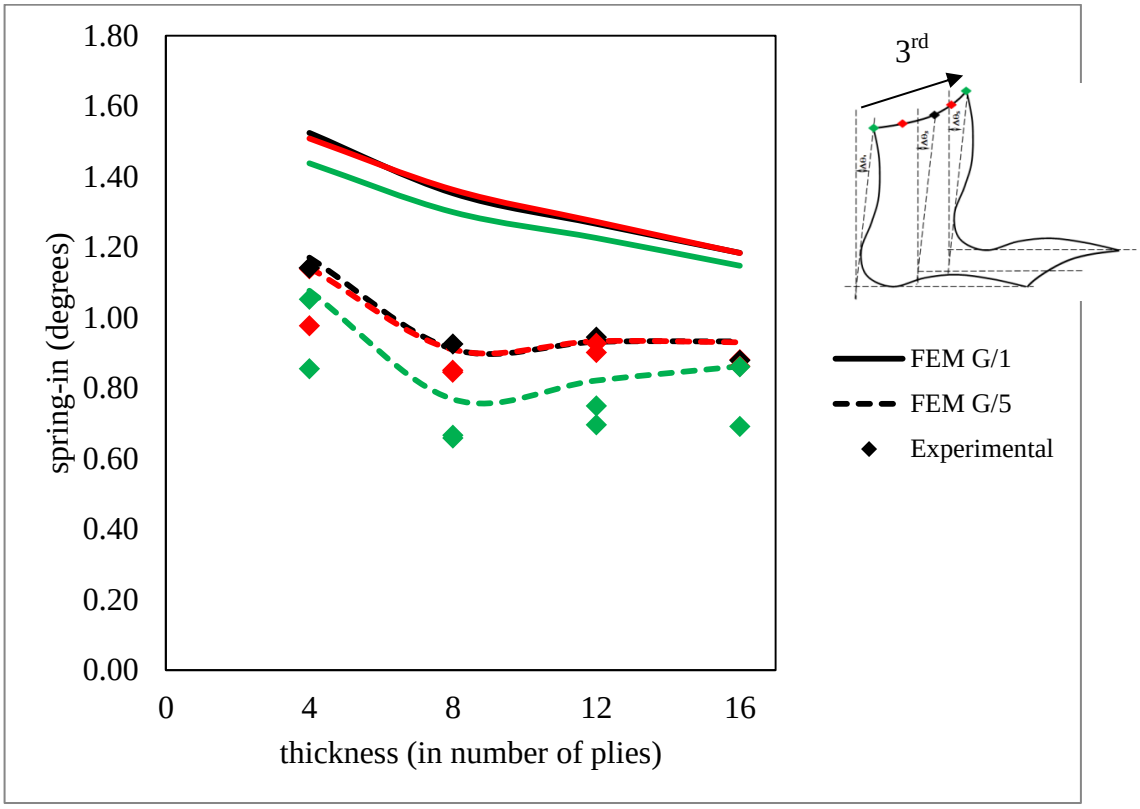


Figure 5.51. Spring-in predictions for XP-R25 parts.

5.3.2. Comparison of Predicted and Measured 3D Distortion Patterns for U-section Samples

Deformation patterns obtained experimentally and numerically for 4-ply UD and XP U-Shaped parts are represented in Figure 5.52. The spring-in values are plotted against the number of plies in Figures 5.53- 5.56 for both corners (R15 and R25 sides) of the U-Shaped parts. The continues and dashed lines in the figures represent the spring in values obtained from FEA and markers represents the measured spring in data at the five equally spaced sections.

The shear modulus reduction in the viscous state decreased the spring-in values and hence the predictions captured the measured spring-in values quite well. The deformation along the 3rd direction is lower in FEM as compared to the measured data. Again, it can be concluded that spring-in values go to asymptotic values as thickness of the laminate increase, as seen Figures 5.53- 5.56.

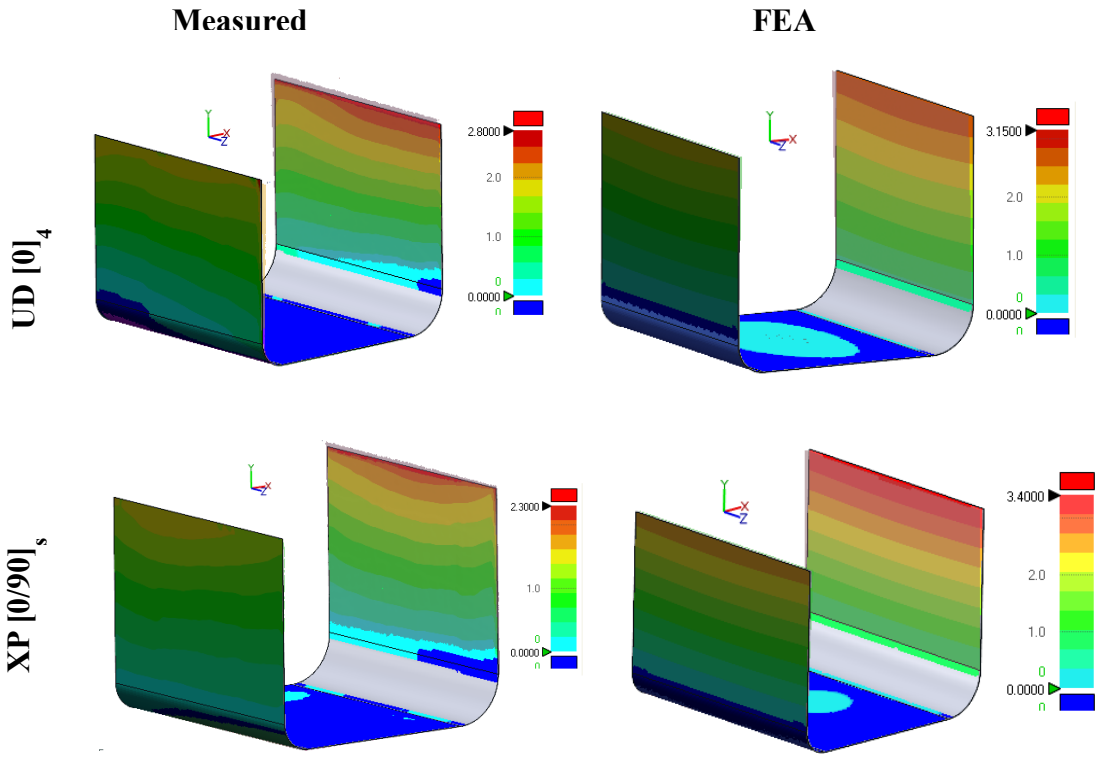


Figure 5.52. Measured and predicted deformation patterns for $[0]_4$ and $[0/90]_s$ U-section parts.

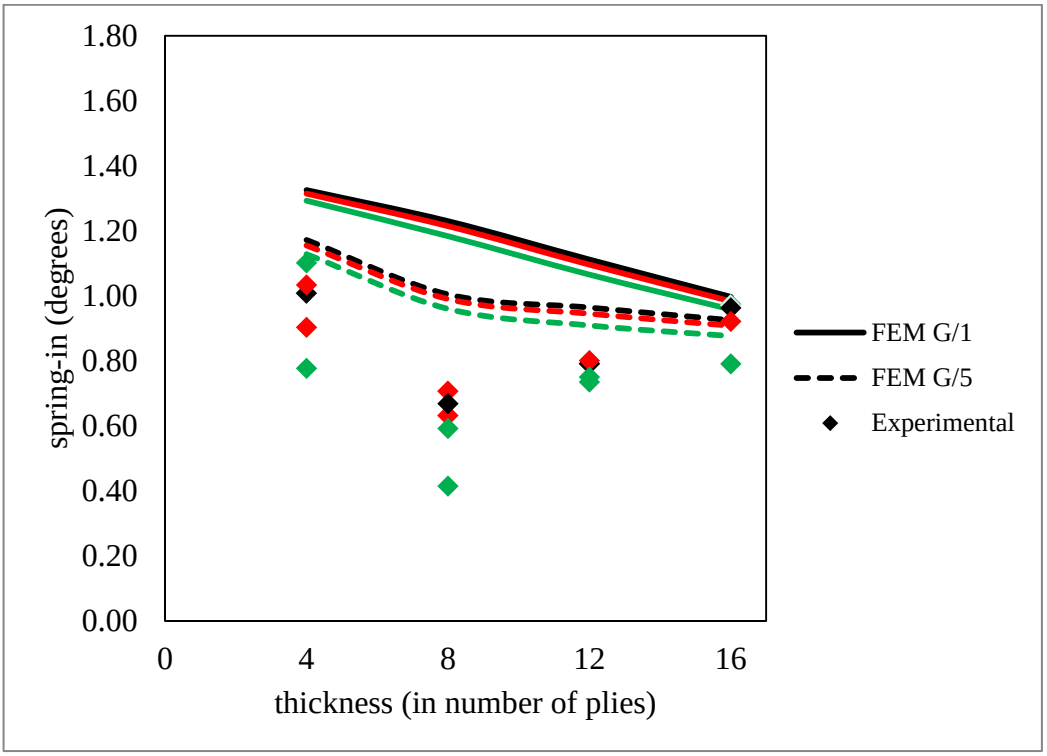


Figure 5.53. Spring-in predictions for R15 side of U shaped UD parts.

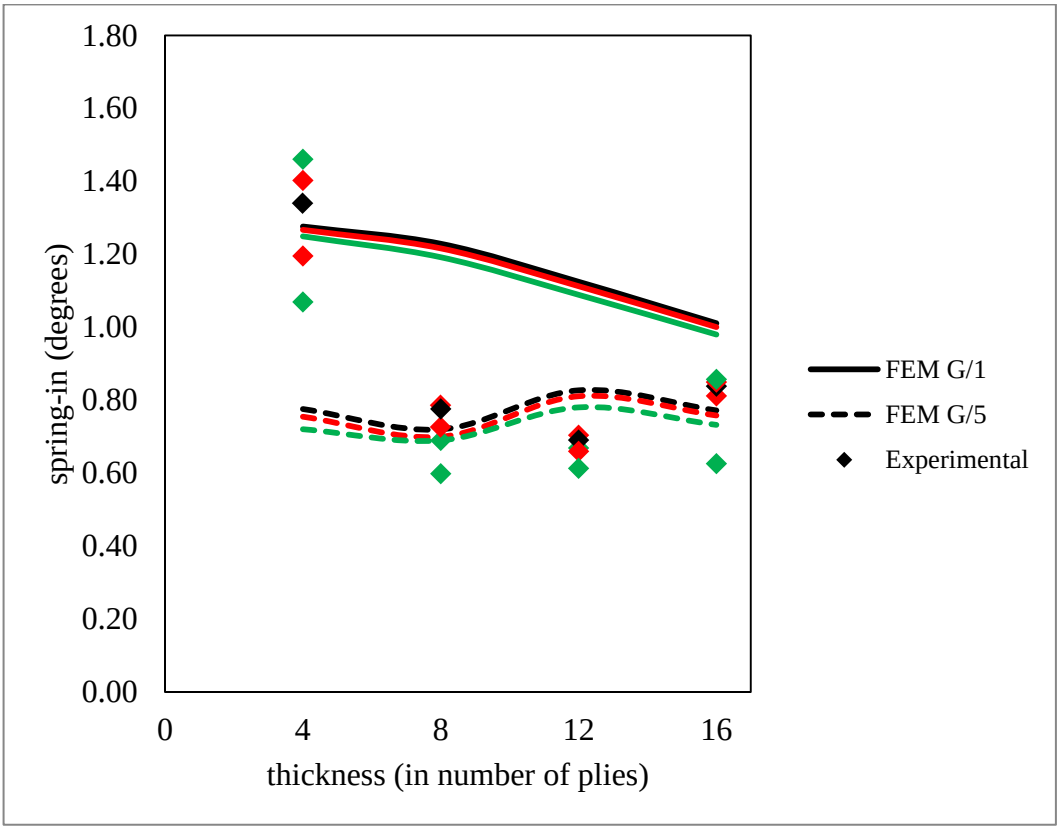


Figure 5.54. Spring-in predictions for R25 side of U shaped UD parts.

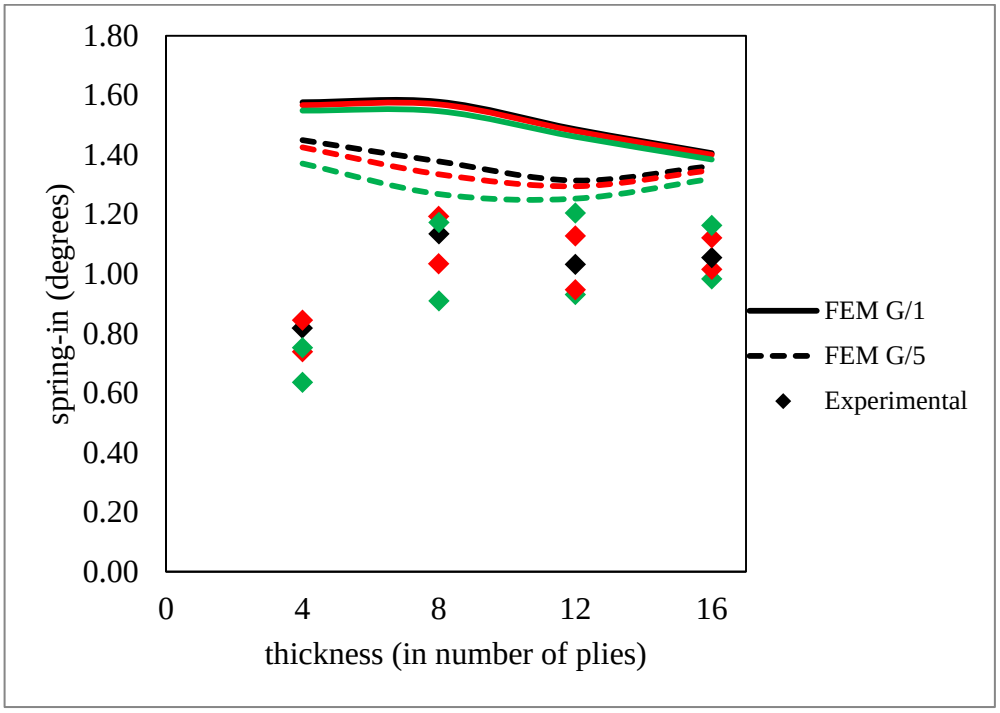


Figure 5.55. Spring-in predictions for R15 side of U shaped XP parts.

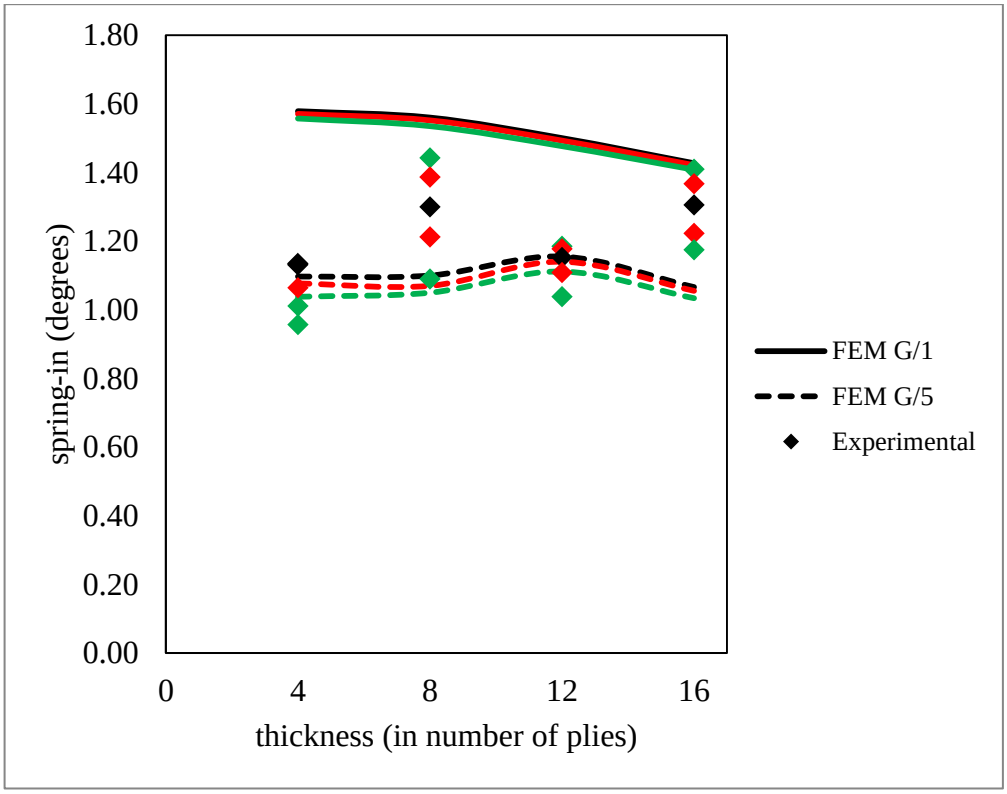


Figure 5.56. Spring-in predictions for R25 side of U shaped XP parts.

Longer (500 mm) U shaped UD and XP parts were also modelled. For the UD sample predictions are quite well when the spring in values and the deformations along the 3rd direction are compared. Full field deformation patterns for the UD4 $[0]_4$ sample, obtained from FEM as well as measured by laser scanner were represented in Figure 5.57. The spring in values and the deformation along the 3rd can be seen in Figure 5.58.

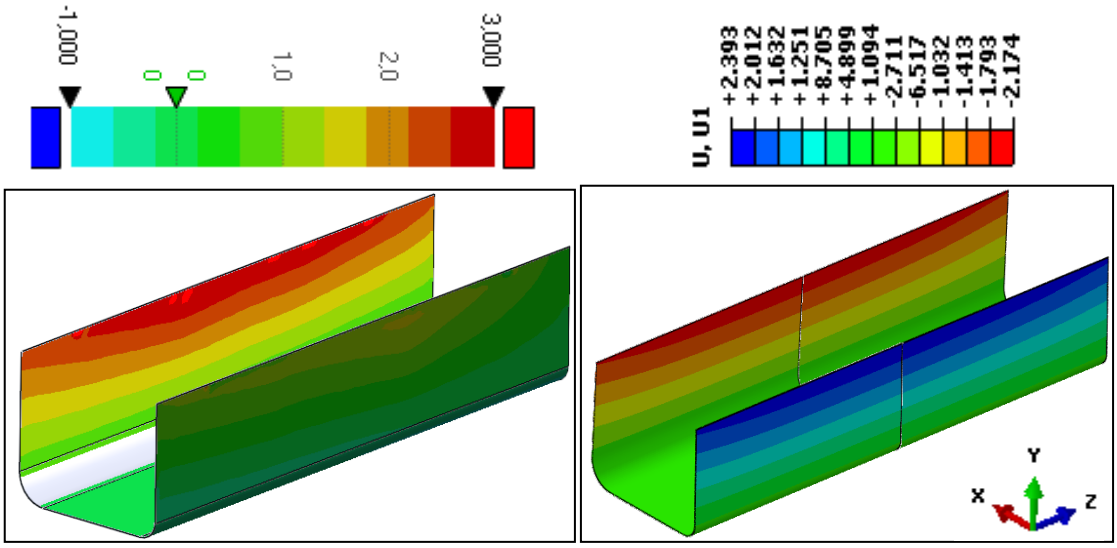


Figure 5.57. Measured and predicted full field deformation patterns for long U-Shaped $[0]_4$ parts.

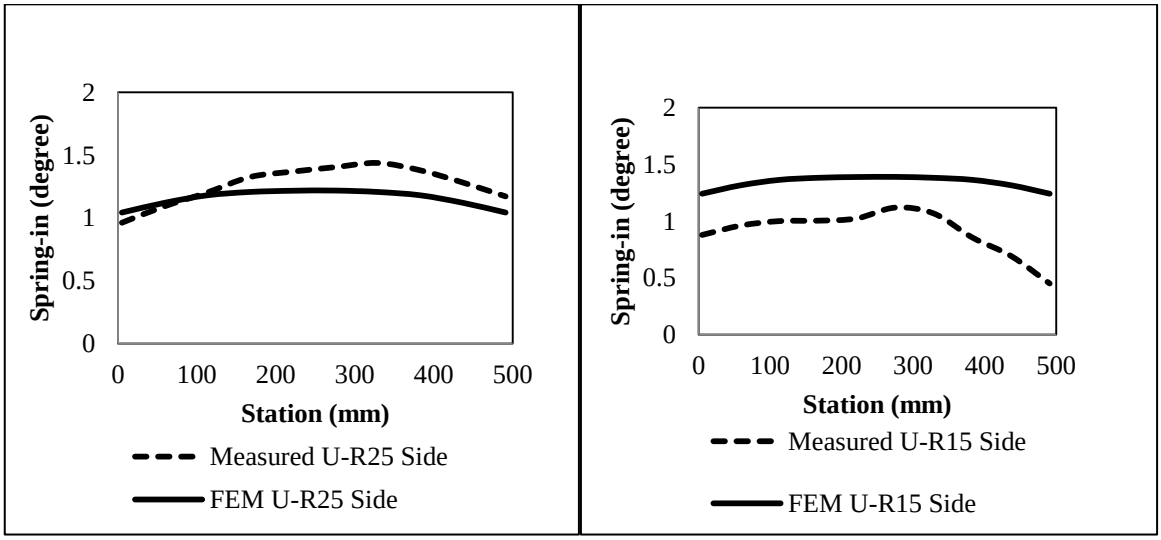


Figure 5.58. Spring-in predictions for long U- Shaped UD4 parts.

Full field deformation patterns for the XP4 $[0/90]_s$ sample, obtained from FEM as well as measured by laser scanner were represented in Figure 5.59. The spring in values

and the deformations along the 3rd can be seen in Figure 5.60. For the XP sample spring predictions are quite well at the mid-section of the part but the deformation along the 3rd direction is rather unexpected. The spring in was higher at the edges of the part as compared to the mid-section of the part.

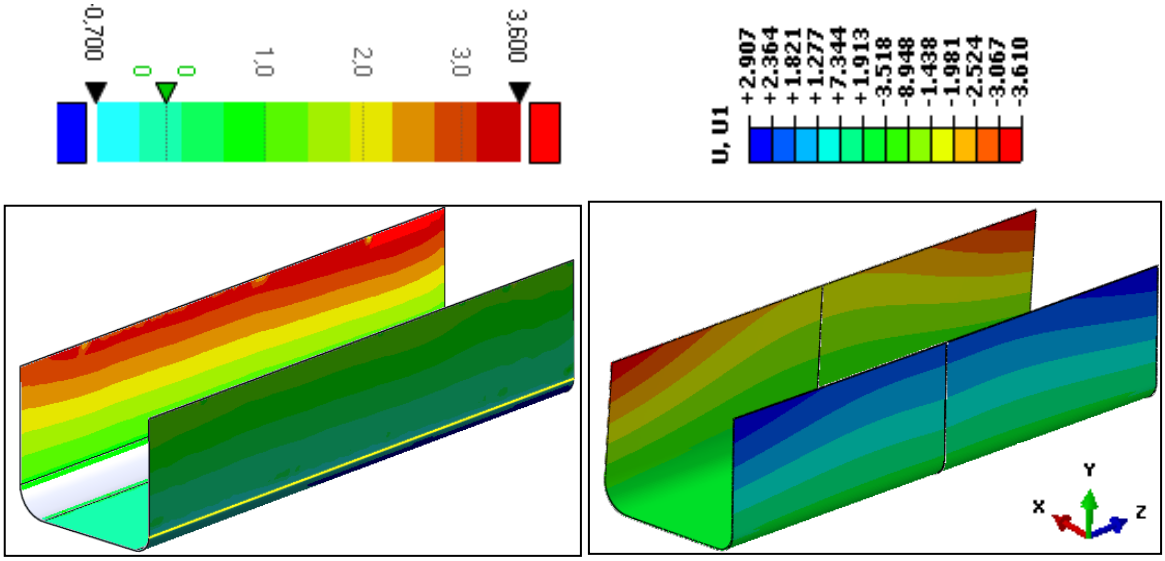


Figure 5.59. Measured and predicted full field deformation patterns for long U-Shaped $[0/90]_s$ part.

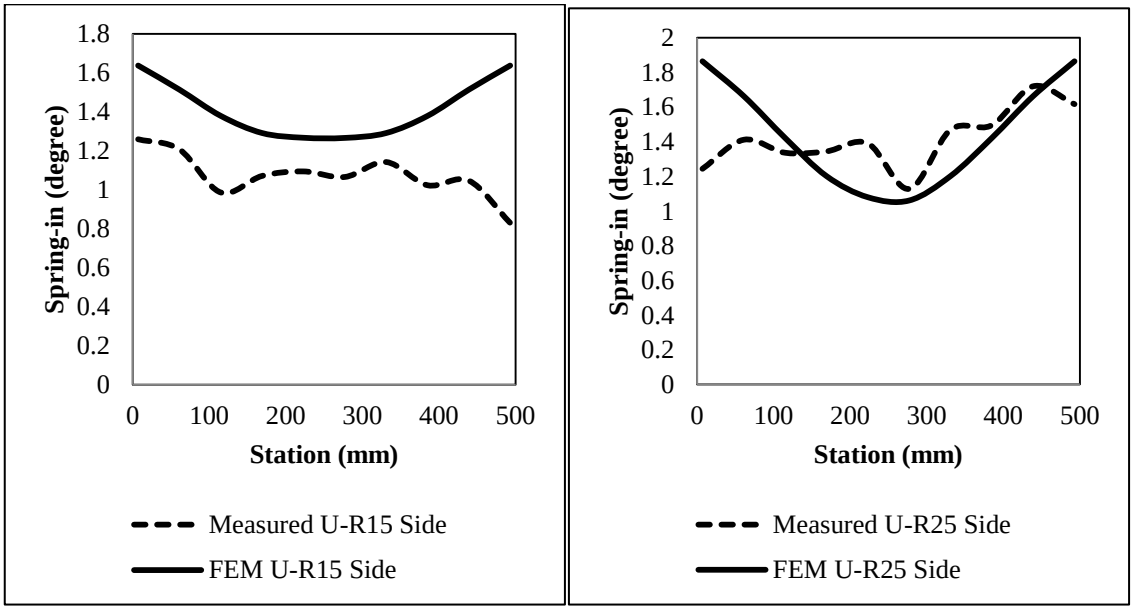


Figure 5.60. Spring-in predictions for long U-section Shaped [0/90]s part.

5.3.3. Comparison of Predicted and Measured Warpage for Flat Strip Samples

The warpage values were represented in Figure 5.61. The solid continuous lines represented results of FEM and the dashed continuous lines represent the measured data. Three stacking sequences were modelled and manufactured: $[90]_4$,$[0/90]_s$, and $[90/0]_s$. Strips of $[0]_4$ were manufactured but warpage measurement could not be done due to lower bending stiffness so that FEM results were not added to the Figure 5.61. Predictions for the configuration of $[90]_4$ and $[90/0]_s$ strips are agree well with the measured data. On the other hand the model over predicted the warpage of $[0/90]_s$ strips.

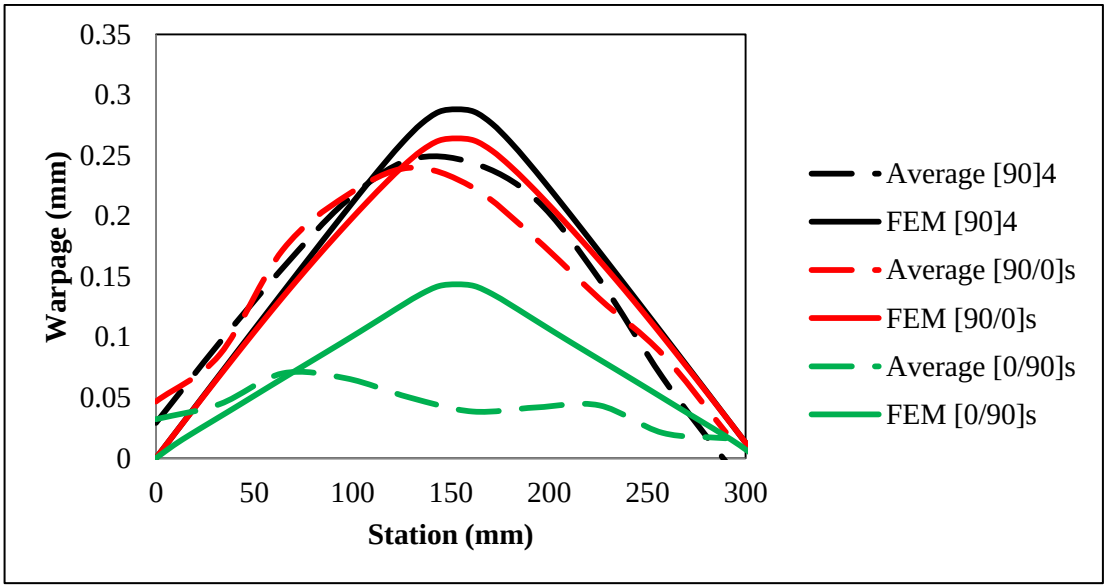


Figure 5.61. Spring-in predictions for flat strip parts of 300 mm length.

6. CONCLUSIONS AND FUTURE WORK

Composite parts of various geometries, stacking sequences, thickness, bagging, and lay-up conditions were manufactured to understand the mechanism that are responsible for distortions. Also a 2D and 3D Finite Element Model has been developed to predict shape distortions during curing of fibre reinforced composite parts.

The obtained results are summarized:

- Regarding the L-Shaped parts, parts with 15 mm radius have greater corner thickening as compared to the parts with 25 mm radius and unidirectional parts have greater corner thickening as compared to cross-ply parts. Corner thickening is basically due to internal percolation of the resin from the arms to the corner region where the pressure is lower due to fibre bridging. The resin flow is lower in cross-ply parts compared to unidirectional parts due to the fact that the cross fibres block the resin tunnelling along the length direction. Corner thickening results in low Fibre Volume Fraction, hence higher Coefficient of Thermal Expansion (CTE) in corner regions as compared to the arms of L-Shaped parts. However, the effect of higher CTE in corner regions to the spring in values are minimal, around 6-14%.

- The effect of fibre waviness on spring-in of L-Shaped was examined, and it was demonstrated that fibre wrinkling at the curved regions significantly reduce spring-in, around 50-60%. Fibre waviness in corner regions is resulting from bending the prepreg to a radius in order to conform to the tool shape. Two different lay-up methods were used to manufacture L-shaped composite parts: in conventional method, the prepreg layers are laid sequentially and in the alternative method, they are laid on flat plate and then bent to conform the radius. Due to in-plane fibre waviness, buckled fibres were observed in micrographs having an elliptical shape at the corner regions of the L-shaped parts manufactured by both conventional and alternative lay-up methods but parts manufactured using the alternative lay-up method includes more buckled fibres distributed through the thickness. Increasing

the amount of fibre wrinkling results in lower spring-in values. Reduction in fibre direction elastic modulus E_{11} due to fibre buckling, as well as the relief of fibre tensile stresses due to consolidation and cure shrinkage resulted in a decrease in spring-in values. The effect of fibre wrinkling on spring-in is demonstrated by developing a heuristic Finite Element Method, which simulates the conformation of the prepregs to the tool surface, development of compressive strains in the inner surface of the bent region which effectively reduces the fibre direction modulus and the effect of these compressive strains to further residual stress development.

- Flat laminates that were manufactured under resin bleeding condition gave more warpage for all configurations as compared to the no-bleeding condition. L-shaped and flat laminates were also manufactured under bleeding and non-bleeding conditions. It was observed that spring-in values are around 25-75% higher for UD laminates and around 100-150% higher for XP laminates higher in the bleeding condition as compared to the non-bleeding condition. Cross-ply laminates under bleeding condition warped more along the 3^{rd} direction as compared to non-bleeding condition. Thicknesses of the laminates that were manufactured under bleeding and non-bleeding conditions were measured. Thickness was less in the arm close to the vacuum port in bleed condition. There is internal percolation to the corner in non-bleed condition, which reduces tension on the fibres close to the bag-side surface in the corner region and through-thickness bleeding increases compaction in corner region and increases fibre tension on the fibres close to the bag-side surface in the corner region, resulting in more spring-in.

- It was observed that unidirectional $[90]_4$ flat strip gives more warpage than cross-ply flat strips of $[0/90]_s$ and $[90/0]_s$ lay-up although both samples were subjected to the same tooling constraints. The reason behind this observation is as follows: tool-part interaction effect is more pronounced for the $[90]_4$ samples due to stretching of fibres in 90 degree ply close to the tool. This generates more residual stress inside the laminate as compared to the other configurations. Effect of stacking sequence on angular distortion such as spring in was also measured for different cross-ply L-Shaped parts. The part that has [90/0]s stacking sequence spring out and gave negative spring-in values.

- The effect of tool-part interaction on the prediction of spring-in angles of unidirectional and cross-ply L-shaped parts of various thicknesses was investigated by using 2D FEM. The tool-part interaction is modelled as a sticking-sliding interface using contact elements. The model worked properly and the observations cast more light on the nature of tool-part interaction during composites manufacturing. It is observed that stresses developed due to tool-part interaction may cause separation of the part from the tool during manufacturing. It has been found that the effective shear modulus of the composite early in the cure has a more pronounced effect on predicted spring-in compared to the interface sliding stress. It has been observed that the three step 2-D model captures most features of the geometry development at the corner sections, except the deformation in the direction perpendicular to the model plane due to tool-part interaction in this direction.

- The 3D Finite Element model captured the distortion in the 3rd direction for L and U shaped laminates. The shear modulus reduction in the viscous state decreased the spring-in values and hence the predictions captured the measured spring-in values quite well. The full field distortion patterns, predicted and measured, were also compared. Three stacking sequences were modelled and manufactured: $[90]_4$,$[0/90]_s$, and $[90/0]_s$. Predictions for the configuration of $[90]_4$ and $[90/0]_s$ strips agree well with the measured data. On the other hand the model over-predicted the warpage of $[0/90]_s$ strips.

- Various stages of Manufacturer Recommended Cure Cycle (MRCC) were shown in Figure 6.1. The mechanisms that are active during manufacturing (MRCC), and their relative importance as a function of thickness were listed in Table 6.1. The parameters used in the models and their relative importance were represented in Table 6.2.

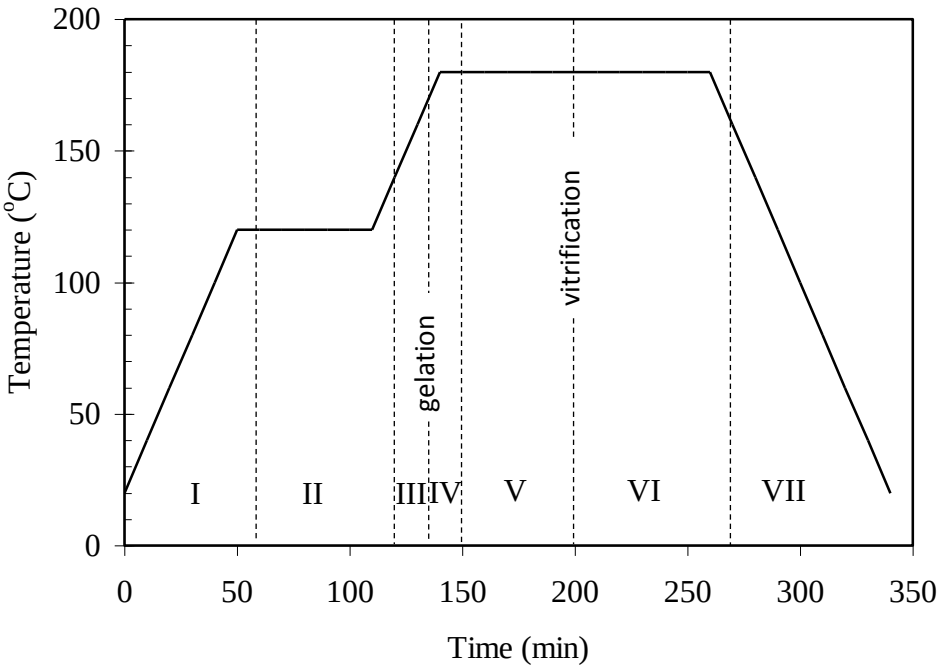


Figure 6.1. Various stages of the MRCC.

Table 6.1. List of various mechanisms that are active during manufacturing (MRCC), and their relative importance (H:High, M:Medium, L:Low) as a function of thickness.

Mechanism	**Before Curing**	**I**	**II**	**III**	**IV**	**V**	**VI**	**VII**	**Importance**
Consolidation		#	#	#					H
Tool Interaction		#		#	#				M
Relaxation			#			#			L
Cure Shrinkage			#	#	#	#			H
Modulus Development			#	#	#	#			H
Thermal Contraction								#	H
Fibre Wrinkling	#								M
Resin Bleeeding		#	#	#					H

Table 6.2. List of parameters used in model and their relative importance (H:High, M:Medium, L:Low).

Mechanism	**Importance**
stacking sequence	H
number of plies	H
τ_{max}^{vis}	M
E_{22}^{vis}	M
G_{12}^{vis}	M
radius	M
G_{12}^{rub}	L
τ_{max}^{rub}	L
μ^{rub}	L
E_{22}^{rub}	L
μ^{vis}	L

As a future work:

- One of the most important parameters affecting the shape distortions is demonstrated to be the shear modulus of the prepreg in viscous and rubbery states of the resin. Shear modulus determines how of the tool-part interface stresses are transferred through the thickness. Shear modulus and tool-part interaction properties during cure may be measured by using strain gauges placed at different locations along the thickness to assess how stress decays. Release film is used in all samples manufactured during this study, and mirror-polished and rough mould surfaces, threated by mould release agent may be used to see the property-variation for the extreme cases.

- More complex shapes of composite laminates like double curved parts may be manufactured in order to understand complex tool-part interaction patterns in more complex 3D shapes. The effect of fibre wrinkling on distortion is significant, so fibre wrinkling may be included in the 3D models.

- As part thickness decreases the effect of tool-part interaction increases. 3D FE model may be calibrated for tool-part interaction parameters using a single ply part that exhibits spring-out.

- Inter-ply slip may be added to model to approach the actual mechanism of shape conformation in the corner. Inter-ply slip decreases the residual stresses due to fibre bridging occurring at the corner regions of a laminate.

- Tool shape may be optimized in order to obtain the desired distortions during manufacturing so that the final part shape shows minimal difference with the intended geometry, so that assembly problems are eliminated.

- Variation is an inevitable phenomenon during manufacturing of composite laminates due to the hand cutting and hand lay-up process, as well as the intrinsic variability even in the same batch of prepreg material, so the number of samples may be increased for variability analysis.

REFERENCES

1. Mazumdar, S.K., *Composites Manufacturing*, CRC Press, Florida, 2002.

2. Wisnom, M.R., M., Gigliotti, N., Ersoy, M., Campbell, and K.D., Potter, "Mechanisms Generating Residual Stresses and Distortion during Manufacture of Polymer-Matrix Composite Structures", *Composites Part A,* Vol. 37, No. 4, pp. 522-529, 2006.

3. Nelson, R.H., and D.S., Cairns, "Prediction of Dimensional Changes in Composite Laminates during Cure", 34th International SAMPE Symposium and Exhibition, Vol. 34, No. 1, pp. 2397-2410, 1989.

4. Sarrazin, H., B., Kim, S.H., Ahn, and G.S., Springer, "Effects of Processing Temperature and Lay-up on Springback", *Journal of Composite Materials,* Vol. 29, No. 10, pp. 1278-1294, 1995.

5. Gigliotti, M., M.R., Wisnom, and K.D., Potter, "Development of Curvature during the Cure of AS4/8552 [0/90] Unsymmetric Composite Plates", *Composite Science and Technology*, Vol. 63, No. 2, pp. 187-197, 2003.

6. Svanberg, J.M., and J.A., Holmberg, "An Experimental Investigation on Mechanisms for Manufacturing Induced Shape Distortions in Homogeneous and Balanced Laminates", *Composites Part A,* Vol. 32, No. 6, pp. 827–838, 2001.

7. Ersoy, N., K., Potter, M.R., Wisnom, and M.J., Clegg, "Development of Spring-in Angle during Cure of a Thermosetting Composite", *Composites Part A,* Vol. 36, No. 12, pp. 1700-1706, 2005.

8. Radford, D.W., and T.S., Rennick, "Separating Sources of Manufacturing Distortion in Laminated Composites", *Journal of Reinforced Plastics and Composites,* Vol. 19, No. 8, pp. 621-640, 2000.

9. Garstka, T., *Separation of Process Induced Distortions in Curved Composite Laminates*, Ph.D. Thesis, University of Bristol, 2005.

10. Hahn, H.T., and N.J., Pagano, "Curing Stresses in Composite Laminates", *Journal of Composite Materials,* Vol. 9, No. 1, pp. 9-91, 1975.

11. Weitsman, Y., "Residual Thermal Stresses due to Cool-down of Epoxy-resin Composites", *Journal of Applied Mechanics*, Vol. 46, No. 3, pp. 563-567, 1979.

12. Adolf, D., and J.E., Martin, "Calculation of Stresses in Crosslinking Polymers", *Journal of Composite Materials,* Vol. 30, No. 1, pp. 13-34, 1996.

13. Sunderland, P., W., Yu, and J.A., Manson, "A Thermoviscoelstic Analysis of Process-Induced Internal Stresses in Thermoplastic Matrix Composites", *Polymer Composites*, Vol. 22, No. 5, pp. 579-592, 2001.

14. Kevin, D., and P.W.R., Beaumont, "The Measurement and Prediction of Residual Stresses in Carbon-fibre/polymer Composites", *Composite Science and Technology*, Vol. 57, No. 11, pp. 1445-1455, 1997.

15. Derek Hull, *An Introduction to Composite Materials*, Cambridge University Press, New York, 1981.

16. Radford, D.W., and R.J., Diendorf, "Shape Instabilities in Composites Resulting from Laminate Anisotropy", *Journal of Reinforced Plastics and Composites*, Vol. 12, No. 1, pp. 58-75, 1993.

17. White, S.R., and H.T., Hahn, "Process Modelling of Composite Materials: Residual Stress Development during Cure. Part II. Experimental Validation", *Journal of Composite Materials,* Vol. 26, No. 16, pp. 2423-2453, 1992.

18. Russell, J.D., M.S., Madhukar, MS., Genidy, and A.Y., Lee, "A New Method to Reduce Cure-Induced Stresses in Thermoset Polymer Composites, Part III: Correlating

Stress History to Viscosity, Degree of Cure, and Cure Shrinkage", *Journal of Composite Materials,* Vol. 34, No. 22, pp. 1926-1947, 2000.

19. Msallem, Y.A., F., Jacquemin, N., Boyard, A., Poitou, D., Delaunay, and S., Chatel, "Material Characterization and Residual Stresses Simulation during the Manufacturing Process of Epoxy Matrix Composites", *Composites Part A,* Vol. 41, No. 1, pp. 108-115, 2010.

20. Prasatya, P., G.B., McKenna, and S.L., Simon, "A Viscoelastic Model for Predicting Isotropic Residual Stresses in Thermosetting Materials: Effects of Processing Parameters", *Journal of Composite Materials,* Vol. 35, No. 10, pp. 826-847, 2001.

21. Madhukar, M.S., MS., Genidy, and J.D., Russell, "A New Method to Reduce Cure-Induced Stresses in Thermoset Polymer Composites, Part I:Test Method", *Journal of Composite Materials,* Vol. 34, No. 22, pp. 1882-1904, 2000.

22. Johnston, A., *An Integrated Model of the Development of Process-induced Deformation in Autoclave Processing of Composite Structures,* Ph.D. Thesis, The University of British Columbia, 1997.

23. Ersoy, N., and M., Tugutlu, "Cure Kinetics Modelling and Cure Shrinkage Behaviour of a Thermosetting Composite", *Polymer Engineering and Science,* Vol. 50, No. 1, pp. 84-92, 2010.

24. Darrow JR, D.A., and L.V., Smith, "Isolating Components of Processing Induced Warpage in Laminated Composites", *Journal of Composite Materials,* Vol. 36, No. 21, pp. 2407-2418, 2002.

25. Dong, C., C., Zhang, Z., Liang, and B., Wang, "Dimension Variation Prediction for Composite with Finite Element Analysis and Regression Modelling", *Composites: Part A,* Vol. 35, No. 6, pp. 735-746, 2004.

26. Hsiao, K.T., and S., Gangireddy, "Investigation on the Spring-in Phenomenon of Carbon Nanofibre-glass Fibre/polyester Composites Manufactured with Vacuum Assisted Resin Transfer Moulding", *Composites Part A*, Vol. 39, No. 5, pp. 834-842, 2008.

27. Bogetti, T.A., and JR. J.W., Gillespie "Process-induced Stress and Deformation in Thick-section Thermoset Composite Laminates", *Journal of Composite Materials,* Vol. 26, No. 5, pp. 626-660, 1992.

28. Wisnom M.R., N., Ersoy, and K.D., "Potter Shear-lag analysis of the effect of thickness on spring-in of curved composites", *Journal of Composite Materials,* Vol. 41, No. 11, pp. 1311–24, 2007.

29. Ersoy, N., T., Garstka, K., Potter, and M.R., Wisnom, D., Porter, and G., Stringer, "Modelling of the Spring-in Phenomenon in Curved Parts Made of a Thermosetting Composite", *Composite Part A*, Vol. 41, No. 3, pp. 410-418, 2010.

30. Twigg, G., A., Poursartip, and G., Ferlund, "An Experimental Method for Quantifying Tool-part Shear Interaction during Composites Processing", *Composite Science and Technology*, Vol. 63, No. 13, pp. 1985-2002, 2003.

31. Twigg, G., A., Poursartip, and G., Ferlund, "Tool-part Interaction in Composite Processing. Part I: Experimental Investigation and Analytical Model", *Composite Part A*, Vol. 35, No. 1, pp. 121-133, 2004.

32. Twigg, G., A., Poursartip, and G., Ferlund, "Tool-part Interaction in Composite Processing. Part II: Numerical Modelling", *Composite Part A*, Vol. 35, No. 1, pp. 135-141, 2004.

33. Potter, K.D., M., Campbell, C., Langer, and M.R., Wisnom "The Generation of Geometrical Deformations due to Tool/Part interaction in the Manufacture of Composite Components", *Composite Part A*, Vol. 36, No. 2, pp. 301-308, 2005.

34. Kappel, E., Stefaniak, D., Sprowitz, T., and Hühne, C., "A Semi-analytical Simulation Strategy and its Application to Warpage of Autoclave-processed CFRP Parts", *Composite Part A*, Vol.42, No. 12, pp. 1985-1994, 2011.

35. Stefaniak, D., E., Kappel, T., Sprowitz, and C., Hühne, "Experimental Identification of Process Parameters Inducing Warpage of Autoclave-processed CFRP Parts", *Composite Part A*, Vol. 43, No. 7, pp. 1081-1091, 2012.

36. Özsoy, Ö.Ö., N., Ersoy, and M.R., Wisnom, "Numerical Investigation of Tool-part Interactions in Composite Manufacturing", *Proceedings of ICCM-16, 16th International Conference on Composite Materials*, 2007.

37. Zeng, X., and J., Raghavan, "Role of Tool-part Interaction in Process-induced Warpage of Autoclave-manufactured Composite Structures", *Composite Part A*, Vol. 41, No. 9, pp. 1174-1183, 2010.

38. Kaushik, V., and J., Raghavan, "Experimental Study of Tool-part Interaction during Autoclave Processing of Thermoset Polymer Composite Structures", *Composite Part A*, Vol. 41, No. 9, pp. 1210-1218, 2010.

39. Arafath, A.R.A., R., Vaziri, and A., Poursartip, "Closed-from Solution for Process-induced Stresses and Deformation of a Composite Part Cured on a Solid Tool: Part I-Flat Geometries", *Composite Part A*, Vol. 39, No. 7, pp. 1106-1117, 2008.

40. Arafath, A.R.A., R., Vaziri, and A., Poursartip, "Closed-from Solution for Process-induced Stresses and Deformation of a Composite Part Cured on a Solid Tool: Part I-Curved Geometries", *Composite Part A*, Vol. 40, No. 10, pp. 1545-1557, 2009.

41. de Oliveria, R., S., Lavanchy, R., Chatton, D., Costantini, V., Michaud, R., Salathe, and J.A.E., Manson, "Experimental Investigation of the Mould Thermal Expansion on the Development of Internal Stresses during Carbon Fibre Composite Processing", *Composite Part A*, Vol.39, No. 7, pp. 1083-1090, 2008.

42. Ferlund, G., N., Rahman, R., Courdji, M., Bresslauer, A., Poursartip, K., Willden and K., Nelson, "Experimental and Numerical Study of the Effect of Cure Cycle, Tool Surface, Geometry, and Lay-up on the Dimensional Fidelity of Autoclave-processed Composite Parts", *Composite Part A*, Vol. 33, No. 3, pp. 341-351, 2002.

43. Zhu, Q., P.H., Geubelle, M., Li, C.L.III, Tucker, "Dimensional Accuracy of Thermoset Composites: Simulation of Process-induced Residual Stresses", *Journal of Composite Materials*, Vol. 35, No. 24, pp. 2171-2205, 2001.

44. Johnston, A., R., Vaziri, and A., Poursartip, "A Plane Strain Model for Process-induced Deformation of Laminated Composite Structures", *Journal of Composite Materials*, Vol. 35, No. 16, pp. 1435-1469, 2001.

45. Potter, K., M., Campbell, and M.R., Wisnom, "Investigation of Tool/part Interaction Effects in the Manufacture of Composite Components", *Proceedings of ICCM-14, 14th International Conference on Composite Materials*, 2003.

46. Kim, Y.K., and I.M., Daniel, "Cure Cycle Effect on Composite Structures Manufactured by Resin Transfer Moulding", *Journal of Composite Materials*, Vol. 36, No. 14, pp. 1725-1742, 2002.

47. Antonucci, V., A., Cusano, M., Giordano, J., Nasser, and L., Nicolais, "Cure- induced Residual Strain Build-up in a Thermoset Resin", *Composites Part A*, Vol. 37, No. 4, pp. 592-601, 2006.

48. Flanagan, R., *The Dimensional Stability of Composite Laminates and Structures*, Ph.D. Thesis, Queen's University of Belfast, 1997.

49. Martin, C.J., J.C., Seferis, and M.A., Wilhelm, "Frictional Resistance of Thermoset Prepregs and its Influence on Honeycomb Composite Processing", *Composites Part A*, Vol. 27, No. 10, pp. 943–951, 1996.

50. Ersoy, N., K., Potter M.R., Wisnom and M.J., Clegg "An Experimental Method to Study Frictional Processes During Composite Manufacturing", *Composites Part A*, Vol. 36, No. 11, pp. 1536–1544, 2005.

51. Sun, J., Y., Gu, Y., Li, M., Li, and Z., Zhang, "Role of Tool-Part Interaction in Consolidation of L-Shaped Laminates during Autoclave Process", *Applied Composite Materials*, Vol. 19, No. 3, pp. 583-597, 2012

52. Khoun, L., and P., Hubert, "Investigation of the Dimensional Stability of Carbon Epoxy Cylinders Manufactured by Resin Transfer Moulding", *Composites: Part A*, Vol. 41, No. 1, pp. 116-124, 2010.

53. Hubert, P., and A., Poursartip, "A Review of Flow and Compaction Modelling Relevant to Thermoset Matrix Laminate Processing", *Journal of Composite Materials*, Vol. 17, No. 4, pp. 286-318, 1998.

54. Dave, R., JL., Kardos, and M P., Dudukovic, "A Model for resin flow during Composite Processing: Part 1-General Mathematical Development", *Polymer Composites*, Vol. 8, No. 1, pp. 29-38, 1987.

55. Gutowski, T G., Z., Cai, S., Bauer, and D., Boucher, "Consolidation Experiments for Laminate Composites", *Journal of Composite Materials*, Vol. 21, No. 7, pp. 650-669, 1987.

56. Hubert, P., R., Vaziri, and A., Poursartip "A Two-Dimensional Flow Model for the Process Simulation of Complex Shape Composite Laminates", *International Journal for Numerical Methods in Engineering*, Vol. 44, No. 1, pp. 1-26, 1999.

57. Li, M., Y., Li, Z., Zhang, and Y., Gu, "Numerical Simulation Flow and Compaction during the Consolidation of Laminated Composites", *Polymer Composites*, Vol. 29, No. 5, pp. 560-568, 2008.

58. Li, M., L., Charles, and III., Tucker, “Modelling and Simulation of Two-dimensional Consolidation for Thermoset Matrix Composites”, *Composites Part A*, Vol. 33, No. 6, pp. 877-892, 2002.

59. Dong, Chensong, “Model Development for the Formation of Resin-rich Zones in Composites Processing”, *Composites Part A*, Vol. 42, No. 4, pp. 419-424, 2011.

60. Radford, D.W., “Cure Shrinkage-induced Warpage in Flat Uniaxial Composites”, *Journal of Composites Technology and Research*, Vol. 15, No. 4, pp. 290-296, 1993.

61. Hubert, P., and A., Poursartip, “Aspects of the Compaction of Composite Angle Laminates: An Experimental Investigation”, *Journal of Composite Materials*, Vol. 35, No. 1, pp. 2-26, 2001.

62. Lightfoot, S.C., M.R., Wisnom, and K., Potter, “A New Mechanism for the Formation of Ply Wrinkles due to sheer between Plies”, *Composites Part A*, Vol. 49, pp. 139-147, 2013.

63. Potter, K., B., Khan, M.R., Wisnom, T., Bell, and J., Stevens, “Variability, Fibre Waviness and Misalignment in the Determination of the Properties of Composite Materials and Structures”, *Composites Part A*, Vol. 39, No. 9, pp. 1343-1354, 2008.

64. Bloom, L.D., J., Wang, and K.D., Potter, “Damage Progression and Defect Sensitivity: an Experimental Study of Representative Wrinkles in Tension”, *Composites Part B*, Vol. 45, No. 1, pp. 449-458, 2013.

65. Gutowski, G.T., and A.S., Tam, “The kinematics for Forming Ideal Aligned fibre Composites into Complex Shapes”, *Composite Manufacturing*; Vol. 1, No. 4, pp. 219-228, 1990.

66. Prodromou, A.G., and J., Chen, “On the Relationship between Shear Angle and Wrinkling of Textile Composite Preforms”. *Composites Part A*, Vol. 28, No. 5, pp. 491-503, 1997.

67. Hancock, S., and K.D., Potter, "The Use of Kinematic drape Modelling to Inform the Hand Lay-up of Complex Composite Components using Woven Reinforcement", *Composites Part A,* Vol. 37, No. 3, pp. 413-422, 2006.

68. Potter, K., C., Langer, B., Hodgkiss, and S., Lamb, "Sources of Variability in Uncured Aerospace Grade Unidirectional Carbon Fibre Epoxy Preimpregnate", *Composites: Part A*, Vol. 38, No. 3, pp. 905-916, 2007.

69. Tarnopol'skii, Y.M., G.G., Portnov, and I.G., Zhing, "Effect of fibre curvature on the modulus of elasticity for unidirectional glass-reinforced plastics in tension", *Polymer Mechanics*, Vol. 3, No. 2, pp. 161-166, 1967.

70. Hsiao, H.M., and I.M., Daniel, "Effect of fibre waviness on stiffness and strength reduction of unidirectional composites under compressive loading", *Composite Science and Technology*, Vol. 56, No. 5, pp. 581-593, 1996

71. Hsiao, H.M., and I.M., Daniel, "Elastic properties of composites with fibre waviness", *Composites: Part A*, Vol. 27, No. 10, pp. 931–941, 1996.

72. Garnich M.R., and G., Karami, "Finite element for stiffness and strength of wavy fibre composites", *Journal of Composite Materials*, Vol. 38, No. 4, pp. 273-292, 2004.

73. Karami, G., and M.R., Garnich, "Effective moduli and failure consideration for composites with periodic fibre waviness", *Composite Structures*, Vol. 67, No. 4, pp. 461-475, 2005.

74. Karami, G., and M., Garnich "Micromechanical study of thermoelastic behaviour of composites with periodic fibre waviness", *Composites: Part B*, Vol. 36, No. 3, pp. 241-248, 2005.

75. Ersoy N., T, Garstka, K, Potter, M.R, Wisnom, D., Porter. M, Clegg, and *et al*. "Development of the properties of a carbon fibre reinforced thermosetting composite through cure", *Composites: Part A*, Vol. 41, No. 3, pp. 401–9, 2010.

76. Loos, A.C., and G.S., Springer, "Curing of Epoxy Matrix Composites", *Journal of Composite Materials,* Vol. 17, No. 2, pp. 135-169, 1983.

77. Huang, C.K., and S.Y., Yang, "Warping in Advanced Composite Tools with Varying Angles and Radii.", *Composites: Part A*, Vol. 28, No. 9, pp. 891-893, 1997.

78. Salomi, A., T., Garstka, K., Potter, A., Greco, and A., Maffezzoli, "Spring-in Angle as Moulding Distortion for Thermoplastic Matrix Composite", *Composite Science and Technology*, Vol. 68, No. 14, pp. 3047-3054, 2008.

79. Yoon, K.J., and J.S., Kim, "Effect of Thermal Deformation and Chemical Shrinkage on the Process Induced Distortion of Carbon/Epoxy Curved Laminates", *Journal of Composite Materials*, Vol. 35, No. 3, pp. 253-263 2001.

80. White, S.R., and H.T., Hahn, "Process Modelling of Composite Materials: Residual Stress Development during Cure. Part I. Model Formulation", *Journal of Composite Materials*, Vol. 26, No. 16, pp. 2423-2453 1992.

81. Bogetti, T., A., and J., W., Gillipse, "Processing-Induced Stress and deformation in Thick Section Thermosetting Composite Laminates", *CCM Report 89-21*, University of Delaware, August, 1989.

82. Min, L., L, Yanxia, and G., Yizhuo, "Numerical Simulation Flow and Compaction during the Consolidation of Laminated Composites", *Wiley Interscience, Society of Plastic Engineers*, Vol. 29, No. 5, pp. 560-568, 2008.

83. Svanberg, J.M., C., Altkvist, and T., Nyman, "Prediction of Shape Distortions for a Curved Composite C-spar", *Journal of Reinforced Plastics and Composites*, Vol. 24, No. 3, pp. 323-339, 2005.

84. Svanberg, J.M., and J.A., Holmberg, "Prediction of Shape Distortions. Part II. Experimental Validation and Analysis of Boundary Conditions", *Composites: Part A*, Vol. 35, No. 6, pp. 723-734, 2004.

85. Arafat, A.R., R., Vaziri, and A., Poursartip, "Closed-Form Solution for Process-induced Stresses and Deformation of a Composite Part Cured on Solid Tool: Part I-Flat Geometries", *Composites: Part A*, Vol. 39, No. 7, pp. 1106-1117, 2008.

86. Arafat, A.R., R., Vaziri, and A., Poursartip, "Closed-Form Solution for Process-induced Stresses and Deformation of a Composite Part Cured on Solid Tool: Part II-Curved Geometries", *Composites: Part A*, Vol. 40, No. 10, pp. 1545-1557, 2009.

87. HexPly 8552 Epoxy matrix, Product Data, Hexcel Composites.

88. Garstka T, N, Ersoy Potter K, and M.R., Wisnom, "In situ measurements of through-the-thickness strains during processing of AS4/8552 composite", *Composites: Part A*, Vol. 38, No. 12, pp. 2517–2526, 2007.

89. Hibbit, Karlson, and Sorensen Inc. *ABAQUS Online Documentation* 2004, Version. 6.5-1.